

SOIL-STRUCTURE INTERACTION OF TDA-GFRP-REINFORCED
CONCRETE SLAB-ON-GRADE WITH GEOCELL-REINFORCED
SANDY SOIL SUBGRADE

By

Hemanth Sai Muralidaran

Submitted in partial fulfillment of the requirements
for the degree of Master of Applied Science

At

Dalhousie University
Halifax, Nova Scotia, Canada
July 2024

Dalhousie University is located in Mi'kma'ki, the
ancestral and unceded territory of the Mi'kmaq.
We are all Treaty people.

© Copyright by Hemanth Sai Muralidaran, 2024

TABLE OF CONTENTS

LIST OF TABLES	v
LIST OF FIGURES.....	vi
ABSTRACT.....	x
LIST OF ABBREVIATIONS AND SYMBOLS USED	xi
ACKNOWLEDGEMENTS	xv
CHAPTER-1 INTRODUCTION.....	1
1.1 Research Background.....	1
1.2 Research Objective.....	6
1.3 Scope of Research	7
1.4 Layout of Thesis Report.....	8
CHAPTER-2 LITERATURE REVIEW	9
2.1 Initial Research and Investigation.....	9
2.1.1 Slab-On-Grade	9
2.1.2 Design Theory of Slab-On-Grade	10
2.1.3 Design of Structural Reinforcement for Slab-On-Grade	14
2.2 Preparation of Subgrade.....	16
2.3 Previous Studies on Geocell-Reinforcement	17
2.4 Exploration of TDA Reinforced Concrete	31
2.5 Investigation of GFRP Reinforced Concrete Slab	49
2.6 Validation of Field Data with Plaxis FEM Analysis.....	67
CHAPTER-3 SPECIMEN PREPARATION AND EXPERIMENTAL TEST SETUP METHODOLOGY	72
3.1 Introduction.....	72
3.2 Test Matrix.....	72
3.3 Material Properties of Components Used in This Research	75
3.3.1 Tire Derivative Aggregates (TDA)	75

3.3.2	Glass Fiber Reinforced Polymer (GFRP)	76
3.3.3	Geocell	78
3.4	Design of Slab-on-Grade.....	79
3.5	Concrete Mix Design	84
3.5.1	Casting of Concrete Slab-On-Grade	85
3.5.2	Concrete Curing Method.....	87
3.6	Soil Subgrade Preparation Method	88
3.7	Subgrade Test Methodology	92
3.7.1	Sand Cone Test	92
3.7.2	Laboratory Compaction Test of Sandy Soil.....	94
3.8	Slab Test Setup Procedure	95
3.9	Testing Procedure.....	98
3.9.1	Compression Test on Concrete Cylinder	98
3.9.2	Plate Load Test.....	99
3.9.3	Monotonic Load Test on Concrete Slab-On-Grade	100
 CHAPTER-4 PLATE LOAD TEST AND MONOTONIC LOAD TEST RESULT		
	COMPARISON.....	102
4.1	Introduction	102
4.2	Plate Load Test Results Comparison	102
4.3	Monotonic Load Test of Slab-On-Grade Specimens on Normal Soil	106
4.3.1	Subgrade Response of GFRP-1 Slab	107
4.3.2	Subgrade Response of 10%-TDA-GFRP-2 Slab	112
4.3.3	Subgrade Response of 20%-TDA-GFRP-1 Slab	117
4.3.4	Non-geocell Subgrade Response Comparison between Slab Specimens	124
4.4	Conclusion	129

CHAPTER-5	FIELD DATA VALIDATION USING PLAXIS 3D FEA SOFTWARE	132
5.1	Introduction	132
5.1.1	Finite Element Soil Model Development.....	132
5.1.2	Soil and Slab Parameters.....	135
5.1.3	Borehole and Subgrade Modeling.....	138
5.1.4	Modeling of Concrete Slab	139
5.1.5	Generating Geometric Mesh	140
5.1.6	Stage Construction	142
5.2	Validation of Field Data with Plaxis 3D Results	144
5.3	Conclusion	146
CHAPTER-6	GEOCELL REINFORCED SOIL RESULTS DISCUSSION	147
6.1	Introduction	147
6.2	Geocell Soil Preparation Method.....	147
6.3	Monotonic Load test of Slab-on-grade on Geocell-Reinforced Subgrade.....	150
6.3.1	Geocell-Reinforced Subgrade Response With GFRP-2 Slab	150
6.3.2	Geocell-Reinforced Subgrade Response With 20%-TDA-GFRP-2 Slab.....	158
6.3.3	Comparison Between Normal Soil and Geocell-Reinforced Subgrade Response	166
6.4	Conclusion	171
CHAPTER-7	CONCLUSION	173
7.1	Future Research Works	176
APPENDIX A	SOIL SUBGRADE IN-SITU FIELD TEST	177
APPENDIX B	SIEVE ANALYSIS OF TDA.....	183
APPENDIX C	COMPRESSIVE STRENGTH OF CONCRETE CYLINDER	185
APPENDIX D	SETTLEMENT INSPECTION CURVE AT LOAD-INTERVAL.....	188
REFERENCES	192

LIST OF TABLES

Table 2.1: Factors of Safety Used for Slab-On-Grade (ACI 360R-10, 2010)	16
Table 2.2: Details of Laboratory Tests Dash et al. (2003)	21
Table 2.3: Properties of Geocell Structure J. N. Mandal; P. Gupta, (1993).....	23
Table 2.4: Properties of Geogrids (Dash et al., 2001).....	29
Table 2.5: Details of Model Test Series (Dash et al., 2001).....	30
Table 2.6: Concrete Mix Proportions (Reda Taha et al., 2008).....	34
Table 2.7: Test Matrix (Naggar et al., 2019).....	39
Table 2.8: Test Specimen Types and Test Method (Maryam Nazari et al, 2022)	46
Table 2.9: Beam Specimen Experimental Results (Maryam Nazari et al, 2022)	47
Table 2.10: Specimen Type Reinforcement Condition(Li-Xiang et al., 2021)	55
Table 2.11: Empirical equation to correlate HSsmall model parameter to RD (Brinkgreve et al., 2010)	68
Table 2.12: HSsmall strain Model Parameters for Sand (Brinkgreve et al., 2010).....	69
Table 3.1: Experimental Testing Schedule.....	74
Table 3.2: Slab-On-Grade and Subgrade Composition (Monotonic Load)	74
Table 3.3: Properties of 10 mm V-Rod 46 GFRP rebar	78
Table 3.4: Forklift Details	80
Table 3.5: M30 Grade Concrete Mix Design.....	84
Table 3.6: Mix Design for One Slab and 4 Cylinders (NCM, 10%-TDA-CM, and 20%-TDA-CM)	85
Table 3.7: Casting Details of All Specimens	86
Table 3.8: Minimum Test Hole Volume (ASTM D1556/D1556M).....	93
Table 4.1: Response of Plate Load Test	105
Table 4.2: Non-Geocell Sandy Soil Result Comparison.....	129
Table 5.1: Plaxis-3D Soil Material Properties	136
Table 5.2: Material Properties of Concrete Slab And Steel Plate	137
Table A.1: Moisture Content Calculation Method.....	179
Table A.2: Sand Cone Test and RD Results of Soil Subgrade	182
Table C.1: Compression Strength of Concrete Cylinders with Different Mix Designs..	186
Table D.1: Settlement Rate Analysis for Each Slab-On-Grade Specimen.....	189

LIST OF FIGURES

Figure 1.1: Scrap Tire Stockpile/Landfill (EWA)	3
Figure 2.1: Slab-on-grade Support System (ACI 360R-10, 2010)	10
Figure 2.2: Flow Chart Indicating the Modulus of Subgrade Methodology based on the Soil Types. (Ringo & Anderson, 1996).....	12
Figure 2.3: Free Body Diagram of Forces Existing to Produce Subgrade Drag Action (Ringo & Anderson, 1996).....	15
Figure 2.4: Photographic view of a Typical Geocell Layer in the Sand Bed and Geogrid Properties Dash et al. (2003).....	21
Figure 2.5: Variation of Bearing Pressure on Footing Settlement for Different Heights of the Geocell Mattress with and without Geogrid Layer - Test Series C and D. Dash et al, (2003).....	22
Figure 2.6: Load-Settlement Curves of Strip Footing on an Unreinforced and Geocell-Reinforced Layer Over Soft Marine Clay J. N. Mandal; P. Gupta, (1993).....	24
Figure 2.7: (A) Bearing Pressure Versus Footing Settlement And (B) Subgrade Modulus Versus Relative Density for Geocell Reinforced Foundation Bed (Dash, 2010).....	26
Figure 2.8 Strain in the Geocell Wall for Soil At 70 and 30% Relative Density (Dash, 2010).....	27
Figure 2.9: Geocell Distribution Pattern and Geocell-Reinforced Foundation Bed (Dash et al., 2001)	29
Figure 2.10: CATRA Annual Report 2022.....	32
Figure 2.11: Schematic Representation of A. Impact Test Setup B. Fracture Toughness Test Setup (Reda Taha et al., 2008).....	35
Figure 2.12: Compression Strength of Rubber Concrete (Reda Taha et al., 2008)	36
Figure 2.13: Experimental Vs Analytical Model (Reda Taha et al., 2008).....	37
Figure 2.14: Test Setup, Compressive Strength, Elastic Modulus, Strain at Peak of TDA Concrete Cylinder (Naggar et al., 2019).....	40
Figure 2.15: Variation of Compression Strength, Elastic Modulus, and Modulus of Rupture of TDA-Reinforced Concrete (Abu Abdo & El Naggar, 2022)	43
Figure 2.16: CA And FA Used in Mix Design (Maryam Nazari et al, 2022)	46
Figure 2.17: Impact-Fatigue Test Setup (Maryam Nazari et al, 2022)	48

Figure 2.18: Test Results of Indoor and Outdoor Slab (A) Compressive Strength (B) Shrinkage (Barragan et al., 2023)	51
Figure 2.19: Indoor Slab Crack Pattern (A) No.4 Steel Rebar (B) No.4 GFRP Rebar (C) No.3 GFRP Rebar Slab (Barragan et al., 2023)	52
Figure 2.20: Outdoor Slab Crack Pattern (A) No.4 Steel Rebar (B) No.4 GFRP Rebar (C) No.3 GFRP Rebar Slab (Barragan et al., 2023)	53
Figure 2.21: Test Setup and Sensor Distribution (Li-Xiang et al., 2021)	56
Figure 2.22: Load VS Deflection Curve (Li-Xiang et al., 2021)	56
Figure 2.23: Midspan Strain Curve Of GFI-3 and GFII-3 Slab (Li-Xiang et al., 2021) ..	57
Figure 2.24: Schematics of GFRP Slab Specimen (Al-Zahrani et al., 2023)	60
Figure 2.25: GFRP Slab-On-Grade Test Results (Al-Zahrani et al., 2023)	62
Figure 2.26: GFRP Slab Geometry and Test Setup (Hassan et al., 2013).....	65
Figure 2.27: Load Vs Deflection Curve (Hassan et al., 2013).....	66
Figure 2.28: Comparison of Horizontal Displacement Profile and Bending Movement of the Wall with Triple Anchors (Brinkgreve et al., 2010).....	71
Figure 3.1: TDA Cutting and Size Segregation	76
Figure 3.2: V-Rod 46 GFRP Rebar	77
Figure 3.3: GF 30 Geocell Panel (Gridforce)	79
Figure 3.4: PCA Thickness Selection Chart for Single Axle Load (Ringo & Anderson, 1996).	81
Figure 3.5: Reinforcement Distribution Diagram and Slab Formwork	83
Figure 3.6: Concrete Slab and Cylinder Casting	87
Figure 3.7: Slab Specimen Moist-Curing.	88
Figure 3.8: Soil Layer Compaction Model	90
Figure 3.9: Soil Tank Preparation Method.....	91
Figure 3.10: (A) Strain Gauge Position (B) Slab Testing Cross-Section Diagram.....	96
Figure 3.11: LVDT Layout and Positioning.....	97
Figure 3.12: Plate Load Test Setup	100
Figure 4.1: Plate Load Test Comparison.....	104
Figure 4.2: Plate Load Test Response of (a) Normal soil (b) Geocell-Reinforced soil ..	106
Figure 4.3: Load Vs Settlement Curve Results for GFRP - 1 Slab Specimen	109

Figure 4.4: Stress-Strain Curve of GFRP-1 Slab	110
Figure 4.5: (A) Soil Crack at Sections A-A1, B-B1, and Lateral Cracks (B) Flexural and Tension Cracks Of GFRP-1 Slab	111
Figure 4.6: Load Vs Settlement Curve of 10%-TDA-GFRP-2 Slab Specimen.....	114
Figure 4.7: Stress-Strain Curve of 10%-TDA-GFRP-2 Slab.....	115
Figure 4.8: (A) Soil Crack at Sections A-A1, B-B1, and Lateral Cracks (B) Flexural Cracks Of 10%-TDA-GFRP-2 Slab.....	117
Figure4.9: Load Vs Settlement Curve of 20%-TDA-GFRP-1 Slab Specimen.....	119
Figure 4.10: Stress-Strain Curve of 20%-TDA-GFRP-1 Slab.....	120
Figure 4.11: (A) Soil Crack At Sections A-A1, B-B1, and Lateral Cracks (B) Flexural Cracks Of 20%-TDA-GFRP-1 Slab.....	123
Figure 4.12: Monotonic Load Test Comparison on Non-Geocell Sandy Soil	126
Figure 5.1: Characteristic Stiffness-Strain Behavior of Soil with Typical Strain Ranges.....	134
Figure 5.2: Secant and Tangent Shear Modulus Reduction Curve	135
Figure 5.3: Soil Subgrade Model in Plaxis 3D	138
Figure 5.4: Structure Stage in Plaxis 3D.....	140
Figure 5.5: Meshing Stage	141
Figure 5.6: Stage Construction and Node Points	143
Figure 5.7: Validation of Lab Testing Data	144
Figure 6.1: (A)Geocell Alignment on Top of The Second Soil Layer (B) Geocell Installation.....	149
Figure 6.2: Load VS Settlement Curve Of GFRP-2 Slab on Geocell-Reinforced Soil ..	152
Figure 6. 3: Stress-Strain Curve Of GFRP-2 Slab on Geocell Reinforced Soil	154
Figure 6.4: (A) Soil Crack at Sections A-A1, B-B1, and Lateral Cracks (B) Flexural Cracks of GFRP-2 Slab.....	158
Figure 6.5: Load Vs Settlement Curve of 20%-TDA-GFRP-2 slab on Geocell-Reinforced Soil	160
Figure 6.6: Stress-Strain curve of 20%-TDA-GFRP-2 Slab on Geocell-Reinforced Soil	162

Figure 6.7: (A) Soil Crack At Sections A-A1, B-B1, And Lateral Cracks (B) Flexural Cracks of 20%- GFRP-2 Slab on Geocell-Reinforced Soil	165
Figure 6.8: Comparison Between Normal and Geocell-Reinforced Soil Monotonic Load Test	168
Figure A.1: Compaction Test Result Curve	180
Figure B.1: TDA Sieve Analysis.....	184
Figure B.2: Particle Size Distribution of TDA	184
Figure C.1: Compression Test Results	185
Figure C.2: Cracked Cylinder Specimens.....	187
Figure D.1: Settlement Curve Graph (A) GFRP-2 (B) 20%-TDA-GFRP-2	191

ABSTRACT

Slab-on-grade has been established as a successful foundation method over the past decades. It is predominantly utilized in manufacturing plants, warehouses, and heavy facility hangars. The consolidative settlement of the slab-on-grade and soil structure occurs mainly due to the monotonic and cyclic incursion of various load types. Geocells are inserted underneath the slab-on-grade at a certain depth to enhance the subsoil structure properties to diminish the soil's pressure and unify the stress distribution pattern. Several studies were conducted on various slab-on-grade compositions placed on geocell-reinforced soil types, which have proven effective. However, the behavior of TDA-reinforced slabs-on-grade under monotonic loads has not been investigated thoroughly. In this study, slab-on-grades are infused with tire-derivative aggregates to replace coarse aggregate at 10 and 20 percent of their volume. The steel rebars have been replenished with glass-fiber-reinforced polymer (GFRP) to improve the moment resistance and flexibility of the slab-on-grade. Plate load tests were conducted on unreinforced and geocell-reinforced sandy soil to manifest the change in the density and bearing capacity of the soil. The control specimen was examined by imposing a monotonic load on the slab superimposed on top of the loose soil. The GFRP slab, 10%-TDA-GFRP, and 20%-TDA-GFRP slab specimens are superimposed on top of unreinforced and geocell-reinforced sandy silt soil to examine under monotonic load. A 3D finite element model was developed using Plaxis 3D analysis software to analyze further and validate experimental laboratory tests, considering various relative densities of the soil subgrade. To summarize, a comparison between these control and special slab specimens is executed in terms of settlement of slab-on-grade versus applied load, concrete Cracking point load, and stress-strain curve to obtain the optimum TDA content and exalt the utilization of geocell-reinforced soil.

LIST OF ABBREVIATIONS AND SYMBOLS USED

Abbreviations

LDPE	Low-Density Polyethylene
ASTM	American Society of Testing and Materials
AASTHO	American Association of State Highway and Transportation Officials
CSA	Canadian Standards Association
ACI	American Concrete Institute
FOS	Factor of Safety
PCA	Portland Cement Association Method
CATRA	Canadian Association of Tire Recycling Agencies
LVDT	Linear Variable Differential Transformer
LP	Linear Potentiometer
W/C	Water Cement Ratio
CA	Coarse Aggregate
FA	Fine Aggregate
SP	Superplasticizer
PCC	Portland Cement Concrete
P _{cr}	Point of Cracking Load
EPS	Expanded Polystyrene
XPS	Extruded Polystyrene
CS	Control Specimen
GFRP	Glass Fiber Reinforced Polymer
TDA	Tire Derivative Aggregate
FEA	Finite Element Analysis
RD	Relative Density
10%-TDA-GFRP	10% Tire Derivative Aggregate Glass Fiber Reinforced Polymer Concrete
20%-TDA-GFRP	20% Tire Derivative Aggregate Glass Fiber Reinforced Polymer Concrete
Cyl	Cylinder Specimen

NS	Normal Soil
GRS	Geocell-Reinforced Soil
HS	Hardening soil model
HSs	Hardening Small Strain Model
SG	Strain Gauge
UTM	Ultimate Testing Machine
NCM	Normal Concrete Mix
10%-TDA-CM	10% Tire Derivative Aggregate Concrete Mix
20%-TDA-CM	20% Tire Derivative Aggregate Concrete Mix

Symbols

A_s	Cross-Sectional Area of Reinforcing Steel
F	Coefficient of friction between base and slab
L	Slab length between free ends
w	Weight of the concrete slab
F_s	Allowable steel stress
MOR	Modulus of rupture
M_{app}	Applied moment of the Slab
M_u	Ultimate Moment
SM	Section Modulus
fb	Allowable stress
b	Base width of the slab section
t	Thickness of the slab section
Φ	Capacity reduction factor
F_y	Yield strength of steel
j_{ud}	Moment arm
q_s	Bearing Capacity
γ	Unit weight of sand
B	Footing width
$N\gamma$	Bearing Capacity Factor
w_i	Drop hammer weight equal
h_i	Height of the drop hammer

N_f	The total number of drops up to failure
IE	Impact energy
f_{RC}	Compressive Strength of rubber concrete
f_C	28 days compressive strength of normal concrete
R	Replacement percentage of the aggregate with tire rubber particles
ρ_f	Reinforcement Ratio
ρ_{fb}	Allowable Reinforcement Ratio
V_{Hole}	Volume of Hole
ω	Optimum Moisture Content in the soil
γ_{wet}	Wet unit weight
γ_{dry}	Dry unit weight
W_{wet}	Weight of Wet soil removed
W_{CON}	Weight of silica sand in the cone
γ_{SILICA}	Unit weight of silica sand
γ_{dmax}	Maximum dry unit weight
γ_{dmin}	Minimum dry unit weight
γ_d	nominal dry unit weight of soil layer
c	cohesion
ϕ	friction angle
ψ	dilatancy angle
E_{50}^{ref}	Secant stiffness
E_{oed}^{ref}	Tangent stiffness for oedometer loading
E_{ur}^{ref}	Unloading/reloading stiffness
m	Power for a stress-level dependency of stiffness
G_0^{ref}	modulus at low levels of strain
G_s	secant shear modulus
G_0	shear modulus
$\gamma_{0.7}$	strain level at which the (G_s) declines to 70% of the (G_0) at small strains

γ_{unsat}	Unsaturated unit weight
γ_{sat}	Saturated unit weight
R_f	Failure Ratio
K_0^{nc}	Coefficient of Lateral Stress in Normal Consolidation
R_{inter}	Interface between soil and structure
d	Diameter of steel bearing plate
E	Youngs Modulus
ν	Poisson's ratio
G	Shear modulus
E_{oed}	primary oedometer loading
X_{Max}	X-Axis maximum value
X_{Min}	X-Axis Minimum value
Y_{Max}	Y-Axis maximum value
Y_{Min}	Y-Axis Minimum value
A, A', B, B'	Concrete slab coordinated in Plaxis 3D and Experiment

ACKNOWLEDGEMENTS

I am immensely thankful to the ALMIGHTY for his unlimited blessings and assistance, which strengthen me to follow the road of righteousness. First of all, I would like to express my heartfelt gratitude to my supervisor, Dr. Hany El Naggar. His wisdom, expertise, encouragement, and constant assistance have served as the foundation for my academic career. His persistent trust in my talents motivated me ahead even in the face of adversity. His mentorship has not only shaped my research but also fostered my personal and professional growth. I am extremely fortunate to have him as my mentor.

I thank Mr. Jordan Maerz and Mr. Jesse Keane for their guidance, unwavering support, and assistance. Their expertise ensured the smooth setup and execution of our tests, allowing for seamless experimentation. Their commitment and assistance were vital to the success of this endeavor.

I am forever grateful to my father, Mr. A. V. Muralidaran, and mother, Dr. S.Maidhili, for their unconditional love, unwavering support, and encouragement throughout this journey. Their sacrifices, understanding, and steadfast support for my aspirations have served as an endless source of strength and inspiration. I am profoundly grateful for your enduring support, which has sustained me through the challenges and triumphs of academic pursuit.

To my dear friends and colleagues, I extend my sincerest appreciation for your companionship and encouragement throughout this adventure. Your support has been priceless, and I feel fortunate to have shared this journey with such exceptional individuals. Their consistent encouragement has been pivotal in shaping my path and I am forever thankful for their presence in my life.

CHAPTER-1 INTRODUCTION

1.1 Research Background

Urbanization and infrastructure development continue to expand in this modern global era of construction. The need for resilient and sustainable construction techniques, proficient in lifespan, serviceability, and maintenance becomes increasingly evident. Engineers have historically found it challenging to construct on loss and soft terrains, significant sections of unreliable surfaces must be consolidated to a greater extent to ensure the safety of the superstructure. When dealing with such unreliable soil, it is a standard practice to use deep foundation technology like pile foundations or a surface improvement technique like Vibro stone columns. Executing a deep or shallow foundation would be extravagant in various situations involving moderate loading circumstances, with fewer levels above the ground level. Under such circumstances, it is best to construct slab-on-grade and reinforce the subsurface soil with geosynthetic material to improve the soil properties. Traditionally, concrete slabs resting on sandy soil subgrades have faced challenges related to cracking, settlement, and overall structural instability due to the uneven settlement and high compressibility of soils. Hence, the involvement of geosynthetic materials in geotechnical engineering projects has increased. There were several studies done on utilizing geocells as soil reinforcement to improve soil properties and has proven to be successful. In several studies geocell confinement system has proven to improve the subgrade density, and load-bearing capacity of the soil, and has substantially brought down the settlement rate compared to other geosynthetic materials. This is obtained by confining the soil mass into small cubical cell boundaries, and the geocells were interlocked against each other to form a large panel, reducing the failure wedges that occur in the soil due to lateral and outward

displacement of soil. Therefore, in this research, we will be utilizing GF30-type geocell as reinforcement for loose sandy soil subgrade. These geocells were manufactured from low-density polyethylene (LDPE) in the form of three-dimensional interconnected cells.

Over the last few decades, there has been a tremendous increase in waste tires that were discarded. Tires cannot decompose naturally. Tire piles at scrap yards and landfills can emit pollutants into the water, air, and ground that change environmental conditions. A rotting tire emits methane gas into the atmosphere by existing in the sun. The universal carbon footprint level is exacerbated by this greenhouse gas, which will aggravate climate change. When stockpiles were left out without any recycling and maintenance equilibrium, these stockpiles provide excellent habitats for rodents, insects, and other species that could damage the ecosystem surrounding them (Naggar et al., n.d.). Canadian government along with several waste management policies, sustainability agencies, and the End-of-life (ELT) tire management stream has managed to attain 100% recycling and reuse of waste tires for various resources and purposes. Every year more than 400,000 tons of waste tires were diverted from the waste stream and recycled into products offering distinct value to end-users. The useful derivatives obtained from scrap tires were Rubber crumbs, molded rubber, tire-derivative aggregates, rubber mulch, fiber, blasting mats, tire-derived fuel, reusable tires, rubber gym flooring mats, and other rubber products. About 15% to 20% of the mass of scrap tires is recycled into tire-derivative aggregates (CATRA_AR_2021 TDA, n.d.).

Researchers have been examining the incorporation of various forms of debris or recyclable products in concrete to enhance its characteristics and performance. Several varieties of waste materials such as recycled construction materials, plastic waste, glass, rubber tire waste, steel manufacturing byproducts, and other products can be inculcated

into the concrete mix. Molenaar has suggested that the implementation of recycled and discarded materials in the road, pavement, slab-on-grade, and other construction projects provides the potential to minimize carbon footprint while improving economic and environmental benefits.



Figure 1.1: Scrap Tire Stockpile/Landfill (EWA)

The Concrete based on normal coarse and fine aggregates is a brittle material with high stiffness and low damping characteristics. The application of concrete structure differs concerning its requirements. Structures such as slab-on grade, pavements, and concrete roads will require immense toughness and impact resistance. The American Society for Testing and Materials (ASTM) has outlined the Standard Practice for the Use of Scrap Tires in Civil Engineering Applications (ASTM D6270-08 2008). In civil engineering applications, discarded tires were first formally used in the 1970s. Since TDA is a non-biodegradable component, it will not lose its engineering properties throughout its lifespan.

TDA's unique characteristics made it possible to save a lot of money and time on several projects. The fusion of TDA in the Concrete elevates the structural integrity of the concrete structure but also contributes towards reusing and promotes sustainable waste management without causing any environmental hazards. The utilization of rubberized concrete slabs has proven to plummet the brittleness, toughness, elastic modulus, compressive strength, and deformation of the concrete structure which has gained acceptance in a decade. According to the findings, Increased rubber content has a detrimental influence on desirable PCC mechanical characteristics but improves ductility and bonding capacity. Hence, in this research, TDA will be incorporated into the concrete mix, by replacing 10% and 20% of coarse aggregate in terms of its volume.

Steel rebars have always been a prominent member used to increase the structural properties of concrete. Although steel enhances the tensile and shear strength of slab-on-grade, it also develops corrosion due to the alkaline and other chemical reactions that take place in the concrete structure leading to a reduction of lifetime, strength, and loss of structural integrity. Over the past decade through various research and experimental studies, it has been proven that Glass Fiber Reinforced Polymer (GFRP) can be used as an effective alternative to overcome those obstacles and enhance the structural properties in slab-on-grades. The predominant feature of this GFRP rebar is the corrosion resistance feature of the polymer and the elongated strain to failure behavior. There have been numerous research and experimental studies done over the past decades to improve the subgrade soil stiffness modulus, bearing capacity, and structural properties of the concrete slab-on-grade. In this research, the concrete slab-on-grade is reinforced with tire derivative aggregates and GFRP rebars to enhance the post-cracking strength, flexural toughness,

crack-width control, fatigue endurance, flexibility, and durability. In terms of sandy soil subgrade, geocell has been inserted to improve the soil properties and reduce the settlement of the structure. Hence, in this research, one control specimen, two concrete slabs were incorporated with 10% TDA with GFRP rebars, two slabs with 20% TDA with GFRP rebars, and two slabs with GFRP rebars were cast and tested. The Slabs were then placed on top of the sandy soil subgrade inside the soil tank which was consolidated accordingly to attain 45% to 50% of relative density and tested by imposing a monotonic load under geocell-reinforced and unreinforced subgrade conditions. The CS and 10%-TDA-GFRP-1 specimens were tested on top of a normal subgrade with relative density varying between 65% to 70 %. The experimental test results gathered from specimens tested on top of normal soil subgrade were investigated with a 3D numerical finite element analysis (FEA) model developed using Plaxis-3D FEA software. Six cases of 3D FEA numerical models were generated with different relative densities (40%, 45%, 50%, 65%, 70%, and 75%) for the soil subgrade. The obtained experimental results were then validated by comparing them to the results obtained from Plaxis-3D FEA models under all 6 cases. The obtained results were examined to determine the optimum TDA content that can be used to construct slab-on-grade for various engineering purposes such as industrial and warehouse flooring, manufacturing plants, heavy facility hangars, etc. The experimental behavior of GF30-type geocell is also tested and the exponential difference in the soil behavior will be emphasized to exalt the usage of geocell as a soil reinforcing agent.

1.2 Research Objective

This research aims to investigate the behavior of concrete slab-on-grade placed on top of unreinforced subgrade and geocell-reinforced sandy soil subgrade, subjected to a central monotonic load. The primary objectives of this research and experimental study were as follows:

- To investigate and understand the difference between the subgrade bearing capacity of sandy soil with respect to unreinforced and geocell-reinforced subgrade conditions.
- Conduct laboratory monotonic load tests on the slab-on-grade specimens under normal subgrade conditions, to investigate and compare the load vs settlement curve and stress-strain curve response of GFRP-1, 10%-TDA-GFRP, and 20%-TDA-GFRP slabs on grade specimens on top of unreinforced sandy soil subgrade.
- Develop a 3D finite element model using Plaxis 3D analysis software, to analyze and validate experimental laboratory test results, considering various relative density values of the soil subgrade (RD-40, RD-45, RD-50, RD-65, RD-70, and RD-75).
- To investigate and compare the load vs settlement curve and stress-strain curve response of GFRP-2 and 20%-TDA-GFRP-2 specimens on geocell-reinforced sandy soil subgrade. To analyze and compare the experimental test data of load versus settlement curve and difference in subgrade response between all the concrete slab specimens tested on both subgrade conditions.

1.3 Scope of Research

In this study, static plate load tests on both subgrade conditions and monotonic load tests were conducted on seven slab-on-grade specimens on top of normal and geocell-reinforced subgrade conditions. The sand was poured inside the soil tank and spread evenly to obtain a 150-mm layer of soil. Each soil layer was then moist evenly with the help of a water sprinkling tool and evenly compacted to obtain a 1.5-meter height of sandy soil subgrade, for each compacted layer, a sand cone test will be conducted to determine the wet and dry unit weight, of that soil layer. Based on the field data, relative density would be calculated for each layer of soil. The soil tank is 2.75 meters long, 2.25 meters wide, and 1.85 meters high. The dimensions of the slab strips are 800 mm long, 400 mm wide, and 127 mm thick. All the slabs were cast on the form outside the sand tank, then moved inside the soil tank and positioned exactly in the middle of the soil tank. Before executing the Monotonic load test, the subgrade was subjected to a non-repetitive static plate load test on a non-reinforced and geocell-reinforced subgrade. The top layer of the soil gets disturbed up to a certain depth of 500 mm, which will be removed and compacted layer by layer using the same compaction method. This will be done after each specimen examination. The deformation response and stress-strain curve under the influence of monotonic load were investigated for all slab types under both subgrade conditions. Comparisons were made between different slab specimens under both subgrade conditions and presented. The obtained field results of soil properties and monotonic load test on normal soil subgrade were validated by developing a similar simulation model in Plaxis 3D FEA software. Based on the compared results optimum TDA percentage slab-on-grade will be proposed and the utilization of geocells as subgrade reinforcement will be exalted.

1.4 Layout of Thesis Report

This thesis report is structured into six chapters. The Descriptive layout of each chapter is mentioned below.

Chapter 1: Introduces the research background of this thesis and provides the objective and scope of this research.

Chapter 2: Literature review presents the initial investigation on the design of slab-on-grade, provides previous research and findings on every material utilized in the concrete slab, testing methodologies, and study on field data validation through finite element analysis.

Chapter 3: Discuss the specimen preparation and experimental test setup methodology, test matrix, material properties, design of slab-on-grade, concrete mix design, casting and curing of concrete slab-on-grade, subgrade preparation methodology, and testing procedures.

Chapter 4: Presents the comparison of plate load test results attained from both subgrade conditions. Explanation and comparison of Monotonic Load test response of slab-on-grade specimens on normal soil.

Chapter 5: Exposes the FEA Model development methodology and validation of field test results with Plaxis 3D FEA software.

Chapter 6: Explores the geocell soil preparation method, investigates and compares normal soil and geocell-reinforced subgrade response due to monotonic load test on slab-on-grade specimens.

Chapter 7: Summarizes the main outcomes, conclusions, and recommendations for this thesis.

CHAPTER-2 LITERATURE REVIEW

2.1 Initial Research and Investigation

2.1.1 Slab-On-Grade

A structure consisting of unreinforced or reinforced concrete slab sitting on a continuous subgrade is called a "slab-on-grade" structure. The interaction between the concrete slab and the supporting components determines the design of slabs-on-ground to resist bending moment and shear force generated by applied stresses. The properties and dimensions of the slab and the supporting materials were important in the design of a slab-on-ground. The slab thickness, mesh, or steel reinforcement were all decided based on the type of slab, the magnitude of load exerted on the slab, the type of soil underneath it, and the bearing capacity of the soil. The most common utilization of the slab-on-grade is for industrial floorings, manufacturing plants, warehouses, Heavy facility hangars, pavements, flooring for house basements, and rigid concrete roads.

Four basic design choices can be selected to construct a slab-on-grade based on the requirements.

- Unreinforced concrete slab.
- Reinforced concrete slab to limit crack widths due to shrinkage and temperature restrains, and applied load.
 1. Utilization of mild steel bars, welded wire fabric mesh, and fiber-reinforced concrete. These slabs must have closely spaced joints to prevent cracks.
 2. Continuously reinforced concrete slabs to prevent saw-cut contraction joints.
- Slab-on-grade reinforced to prevent cracking.

1. Shrinkage compensating concrete.
 2. Post-tensioned concrete slab.
- Structural slabs (structurally reinforced with rebars).

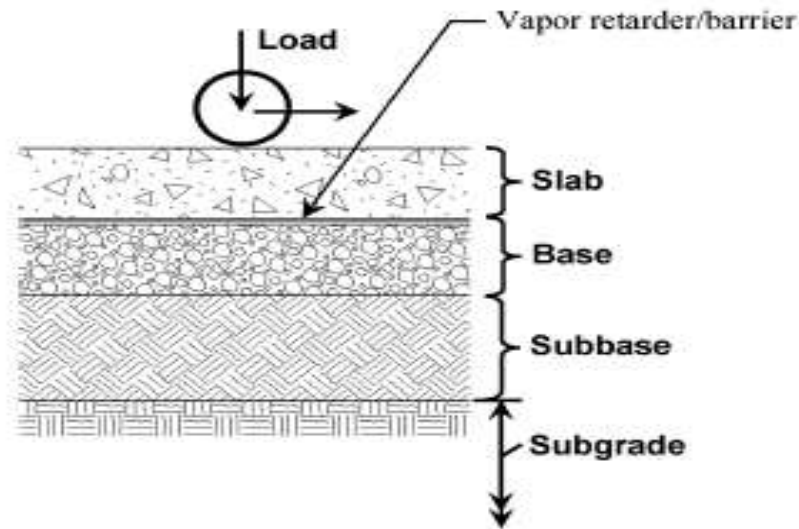


Figure 2.1: Slab-on-grade Support System (ACI 360R-10, 2010)

Stresses exerted in slabs-on-grade result from both applied loads and volume changes of the soil and concrete. The magnitude of these stresses depends on factors such as the degree of continuity, subgrade strength, uniformity, construction method, construction quality, and load position. The slab-on-grade must at least have a minimum thickness of 4 inches, and it varies in correspondence to the utilization of the slab.

2.1.2 Design Theory of Slab-On-Grade

The slab-on-grade design methodologies were based on theories developed for airport and highway pavements. Around the mid-1920s, a rational approach was developed by Westergaard to optimize a practical design methodology for slab-on-grade, Westergaard (1926) then proposed a theory called the “corner formula” to evaluate the stress acting on the slab. Most of the slabs were subjected to non-uniform loading, therefore, this theory analyses it as a homogeneous, isotropic, and elastic slab laying on a suitable subgrade that

applies a vertical retaliating pressure inversely related to the slab's deflection at all spots. This is known as a Winkler subgrade (Winkler 1867). The subgrade acts as a linear spring, with a proportionality constant k with units of pressure (lb/in.² [kPa]) per unit deformation (in. [m]). This constant is defined as the modulus of subgrade reaction and is determined from static plate load tests.

During the 1930s, the Arlington Virginia Experimental Farm and the Iowa State Engineering Experiment Station conducted extensive investigations on the structural behavior of concrete pavement slabs which remained continuously supported by the subgrade, exhibited a strong correlation between the observed stress and the computed stress obtained through Westergaard theory. (Lösberg 1978; Pichaumani 1973) later proposed a strength theory based on the yield-line concept for ground-supported slabs. All identified theories can be categorized based on the models implemented to simulate the behavior of the slab and subgrade.

Three different models were used for the slab:

- Elastic-isotropic solid.
- Thin elastic slab.
- Thin elastic-plastic slab.

The two models used for the subgrade were:

- Elastic-isotropic solid.
- Winkler.

A slab-on-grade cannot be designed without parameters that were derived from field in-situ and lab tests of the soil subgrade that supports the slab. A value for the modulus of subgrade, denoted as K , is necessary at the very least. In addition to K , it is necessary to

know the properties of the underlying soil and the fill material. The flow chart below summarizes an orderly approach to obtaining the soil properties, concerning the soil type.

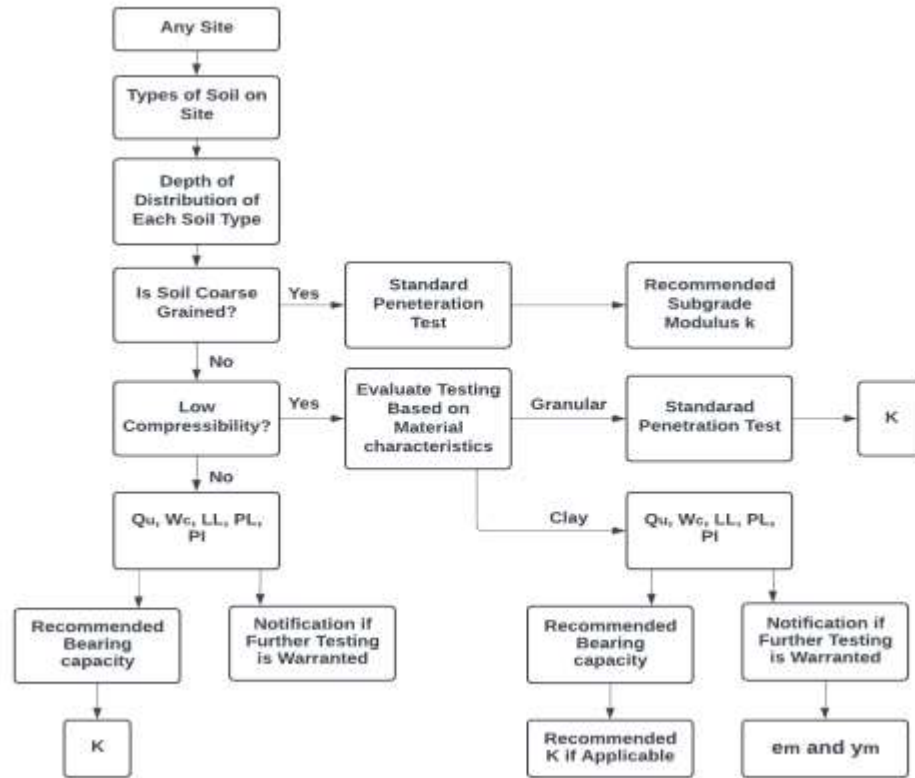


Figure 2.2: Flow Chart Indicating the Modulus of Subgrade Methodology based on the Soil Types. (Ringo & Anderson, 1996)

There were six commonly used methods or procedures by which industrial floors were planned and the thickness was determined.

- PCA, Portland cement association method.
- WRI, Wire Reinforcement Institute method.
- COE, U. S. Army Corps of Engineers method.
- PTI, Post-tensioning Institution method.
- ACI 223, ACI committee 223 method.
- MATS (PCA) Finite Element method.

All these methods have been proven effective and useful when utilized under the required circumstances and differ based on the project's needs. PCA has always been a predominant method for designing a slab-on-grade for industrial warehouses and other heavy structure floorings. PCA's charts and tables permit slab thickness selection for dual and single-wheel axle loads, rack support post-loading, column load, and uniform loads with fixed or variable positions. Slab thickness calculations were based on the assumption of an uncracked and unreinforced slab. Steel reinforcement may be used in slabs-on-grade to improve the performance of the slab under certain conditions which will be efficient to obtain these criteria:

- Limiting the width of shrinkage cracks.
- Use of longer joint spacings than unreinforced slabs.
- Providing moment capacity and stability at cracked sections.

The utilization of reinforcement in the slab-on-grade will not completely restrict cracking, whilst it will increase the shrinkage crack frequency and it will reduce the crack width. Properly proportioned and positioned, reinforcement will limit crack widths such that the cracks will not affect slab serviceability. The PCA, WRI, and COE methods can also identically be utilized to design the slab thickness of reinforced slab-on-grade by simply ignoring the presence of rebars. The inclusion of reinforcement for crack width control is done to decrease the joint spacings and thickness of the slab. To eliminate saw-cut contraction joints, a minimum steel ratio of 0.5% (PCA 2001) of the slab cross-sectional area is recommended. Reinforcements for crack width control must always be positioned at or above the mid-depth of the slab-on-grade. It should never be dropped below the mid-depth. A common practice is to specify that the steel has a 1.5 to 2 in. (38 to 51 mm) cover

below the top surface of the concrete. Reinforcements that were specifically provided for moment capacity must be positioned at the centroid of the tensile area of the uncracked concrete section.

2.1.3 Design of Structural Reinforcement for Slab-On-Grade

Generally, it is mandatory to design the steel reinforcements for the slab-on-grade if any one of the four basic requirements is satisfied. Proper positioning of steel reinforcement within the concrete slab is essential. The steel positioning also depends on why the steel reinforcement has been specified. The four basic requirements were as follows. (Ringo & Anderson, 1996)

- To act as crack control. Here, the steel is commonly selected using the subgrade drag equation. This subgrade drag equation is commonly used to determine the area of reinforcing steel which is utilized for shrinkage crack control. This equation does not provide the specific area of steel that is suitable for structurally active steel. In contrast, it is intended to select the steel rebar and place it in both directions, to accept the tensile stress that is exerted in the concrete.

$$A_s = \frac{FLW}{2F_s}$$

A_s = cross-sectional area of reinforcing steel, in square inches per lineal foot of slab width

F = coefficient of friction between base and slab

L = slab length between free ends, in the direction of the intended steel

w = weight of the concrete slab, psf
(usually, 12.5 pounds per inch of slab thickness)

F_s = allowable steel stress, psi

- To act as the required steel with shrinkage-compensating concrete slabs. The steel reinforcement used here is essential to improve the slab performance when concrete joints are placed at a much wider spacing rather than the nominal spacing. The steel is selected following the requirements of ACI Committee 223 the usual spacing.

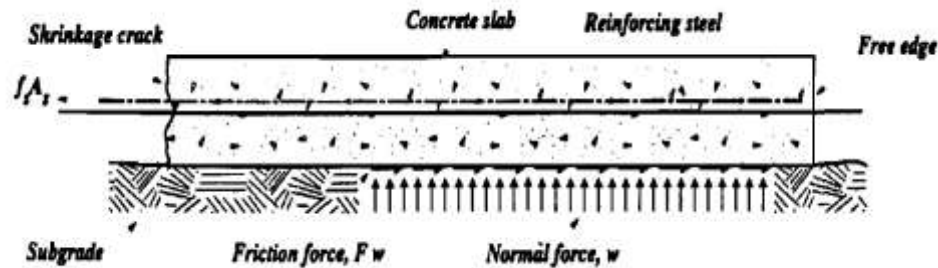


Figure 2.3: Free Body Diagram of Forces Existing to Produce Subgrade Drag Action (Ringo & Anderson, 1996)

- To provide reserve load capacity, the main objective of this is to maintain the slab thickness that was designed for an uncracked and unreinforced slab section. This criterion is obtained by inserting steel reinforcement and the steel area is increased to achieve an increment in the moment capacity for the reinforced and cracked section which is escalated greater than the allowable moment capacity of the slab section.
- To allow the use of a thinner slab. In this method, the loading capacity of the slab is multiplied with a safety factor due to the substantially imposed large area of steel than the area of steel indicated by the subgrade drag equation. The slab section is anticipated to develop small hairline cracks (generally less than 0.01 inch thick) due to various types of loading.

Slabs were often designed to remain uncracked as a result of imposed loads; thus, the design should be calculated with an appropriate factor of safety to reduce the probability of serviceability failure due to cracking. The major significance is ascertaining that the slab

joint spacing, thickness, and reinforcement requirement were the critical criteria that distinguish the number of random cracks to be exerted on the slab due to various loads. Table 2.1 shows some commonly used safety factors (FOS) for various types of slab loadings.

Table 2.1: Factors of Safety Used for Slab-On-Grade (ACI 360R-10, 2010)

Load Type	FOS
Moving Wheel Load	1.7 to 2.0
Concentrated Load	1.7 to 2.0
Uniform Load	1.7 to 2.0
Line and Strip Load	1.7
Construction Load	1.4 to 2.0

2.2 Preparation of Subgrade

The subgrade beneath the slab-on-grade plays a pivotal role in the performance of the footing slab. The soil layers on a site must be investigated, and classified according to their type, and parametric studies must be done to determine the soil parameters. To guarantee satisfactory slab performance, the subgrade supporting the slab-on-grade needs to be prepared with extreme precision. While it is usually believed that the soil is distributed uniformly, this is frequently not how soil behaves (Hernandez & Bsce, 2014). Generally, the subgrade consists of several irregularities that may change the stress distribution pattern in the soil, leading to the generation of cracks in the tension side of the slab. The main factors causing excessive uneven settlement, cracking on the slab, and the soil's inability to support the imposed loads when improperly compacted and unevenly distributed soil mass (PCA, 1983). A poor subgrade causes unanticipated settling and accumulation of water against the Slab-on-grade, which causes seepage and

slab deterioration. The uneven subgrade modulus, change in soil properties, low resistance to the applied load, and uneven settlement of the soil due to imposed load were all significant factors that affect the performance of the slab-on-grade, especially when the slab is subjected to heavy load.

To avoid this, the construction area must be marked and any kind of debris or obstacles such as grass, rock, and other rubbish must be removed. The area must be excavated up to at least 6 inches. The optimal subgrade must be without frost, organic matter, and dirt. It should have the right slope and be well-drained. The compaction method must be the same throughout the soil mass to provide a uniformly consolidated subgrade. Soil parameters such as wet unit weight, dry unit weight, moisture content, bearing capacity, and relative density of the soil must be maintained consistently throughout the soil surface. According to the soil type, the relative density of the soil must be kept within the selected limits throughout the soil area. Depending on the soil type and project requirements geosynthetic materials such as geocells can be provided as soil reinforcement agents.

2.3 Previous Studies on Geocell-Reinforcement

The application of geosynthetics in geotechnical engineering projects is rising. These reinforcing components were an affordable remedy for several construction-related issues, such as retaining structures, highways, dams, foundations, slope stability, and erosion control. There were several geosynthetic reinforcement materials such as geotextile, geomembrane, geogrid, geonet, geocell, geosynthetic clay liner, and geo-composites. Over the last few years, geocells have proven to be more successful than other approaches for soil reinforcement in a variety of geotechnical engineering applications. Geocells can be categorized into two types: non-perforated geocells and perforated geocells, in terms of

shapes they can be composed into circular, square, rectangular, hexagonal, honeycomb, and three-dimensional polyethylene interlocking geocell panels. Geocells are generally a cost-effective and sustainable component that can be utilized to improve the soil properties and its performance.

The US Army Corps of Engineers created geocell first in the early 1970s and implemented it on military applications. Based on this, many research engineers have studied and examined the geocell in many laboratory experiments to improve the application of geocells in various streams of engineering projects. These studies were focused on obtaining the efficiency of geocells in enhancing the properties and performance of various soil types in various geotechnical applications (Hegde, 2017). From the mid-1990s onward, numerical simulation software was used to investigate the functionality of the geocells. Through the use of numerical simulations, numerous researchers have improved their understanding of geocells over the decades. Based on these previous numerical simulations analysis results and laboratory study results have led to performing large-scale model testing or real field investigations to observe and understand the geocell effectiveness. Generally, geocells were cast into three-dimensional panels depending on the type of the geocell, they were manufactured from welded high-strength polymers or polymeric alloys such as polyethylene, polyolefin, etc. (Hegde & Sitharam, n.d.). Due to its intricate structure of interconnected cells and adjacent panels, the geocell reinforcement mechanism confines the soil particles inside the cell, restricting soils from spreading laterally under exerted pressure. Thus, geocells act as a more rigid mattress that dissipates applied loads over a larger surface area. (Mahgoub, 2019) Geocell reinforcement performance is influenced by several variables, including soil cover thickness, the relative

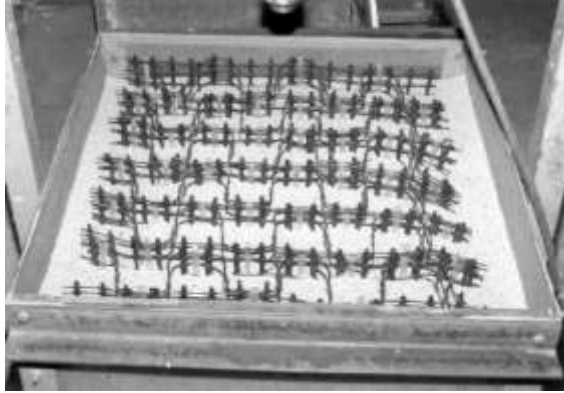
density of compacted subgrade and fill aggregate, geometric properties, and the tensile strength of the product used to create the geocell. (Kargar and Hosseini 2016; Zhang et al. 2018).

Over the past decades, Numerous studies have demonstrated how effective it is to use geocells to improve highway construction by decreasing the characteristics of rutting and deformation of the road. For instance, Imad L. Al-qadi and John J. Hughes (2000) conducted a field test on Route 30 in Delaware County, Pennsylvania, an urban route with a significant average daily traffic. Potholes and wheel rutting of more than 100 millimeters were observed within 7 days of repair of a portion. In this study, to stabilize the subgrade and alleviate this challenge, a geocell and geogrid confinement method was installed. The geocell was made of high-density polyethylene. Each geocell panel was manufactured into 3.3 m long and 100 mm thick strips. When enlarged, the panels were 2.4 m x 6.1 m and formed a honeycomb-patterned cellular confinement system. The outcomes showed that the geocell system utilized in this project succeeded quite well: There has been no evidence of pavement distress (alligator cracking, rutting, etc.) on the route.

➤ **The behavior of geocell-reinforced sand beds under circular Footing**

Dash et al. (2003) have studied the efficiency of geocell reinforcement utilized in granular fill covering soft clay beds have been investigated in laboratory environments using small-scale experimental testing. A circular footing was placed on top of the sandy soil, it was subjected to a monotonic load through a hydraulic jack. Based on this experimental investigation the load exerted by the circular footing, settlement caused due to the footing load, and the deformation attained in the soil surface were obtained and analyzed. In addition to the geocell reinforcement, the soil body was supported by providing a planar

geogrid layer at the base of the geocell mattress and the overall efficiency of the system has been thoroughly investigated using a series of monotonic load tests. The experimental testing was carried out in the laboratory using a testing tank attached to a loading frame arrangement. The soil mass was laid out in a test tank having internal dimensions of 900mm length, 900mm width, and 600mm height. The circular footing used was made out of a rigid steel plate and measured 150mm in diameter and 30mm in thickness. The base of the footing was made rough by coating a sandy layer with epoxy glue. The geocell mattress was formed on top of the compacted clay bed. The geocell layer was created by cutting entire rolls of geogrids to the desired length and height and arranging them in transverse and diagonal directions with bodkin joints (plastic strips) placed at the junctions. depending on the soil mass preparation method the geogrids were also placed underneath the geocell surface and then the geocell was inserted into the soil mass, the remaining soil mass was poured and compacted for testing. The force was applied at a rate of roughly 2 mm/min, the footing had settled into the sandy soil. The experimental test was done under the same procedure for both types of reinforced soil mass, the results were obtained and compared. Series A tests were conducted for different thicknesses (H) of the overlaying sandy soil. Series B and C were based on the influence of varying the width and height of the geocell layer. Series D was specifically for the planar geogrid layer, it was inserted in the soil without being connected to the geocell layer. Series 6 is for planar reinforcement layers based on the previous series results.



Properties of the geogrid

Parameter	Quantity
Polymer	Polypropylene
Aperture size (MD × XMD)	41 mm × 31 mm
Peak tensile strength (MD × XMD)	14.5 kN/m × 20.5 kN/m
Yield point strain (MD × XMD)	16% × 13%

MD: machine direction, XMD: cross-machine direction.

Figure 2.4: Photographic view of a Typical Geocell Layer in the Sand Bed and Geogrid Properties Dash et al. (2003)

Table 2.2: Details of Laboratory Tests Dash et al. (2003)

Test series	Type of reinforcement	Details of test parameters
A	Unreinforced	Variable parameter: $H/D = 0, 0.52, 0.94, 1.36, 1.78, 2.20, 2.62$ Constant parameter: $C_u = 3.13 \text{ kN/m}^2$, $ID = 70\%$
B	Geocell alone	Variable parameter: $b/D = 1.2, 1.7, 2.2, 3.6, 5.0, 5.6$ Constant parameter: $d/D = 0.8$, $h/D = 1.26$, $u/D = 0.1$
C	Geocell alone	Variable parameter: $h/D = 0.42, 0.84, 1.26, 1.68, 2.10, 2.52$ Constant parameter: $d/D = 0.8$, $b/D = 5.0$, $u/D = 0.1$
D	Geogrid layer below geocell mattress	Variable parameter: $h/D = 0.42, 0.84, 1.26, 1.68, 2.10$ Constant parameter: $d/D = 0.8$, $b/D = 5.0$, $u/D = 0.1$
E	Planar reinforcement layers	$N = 6$, $b/D = 6$, $\Delta u = \Delta h = 0.333D$

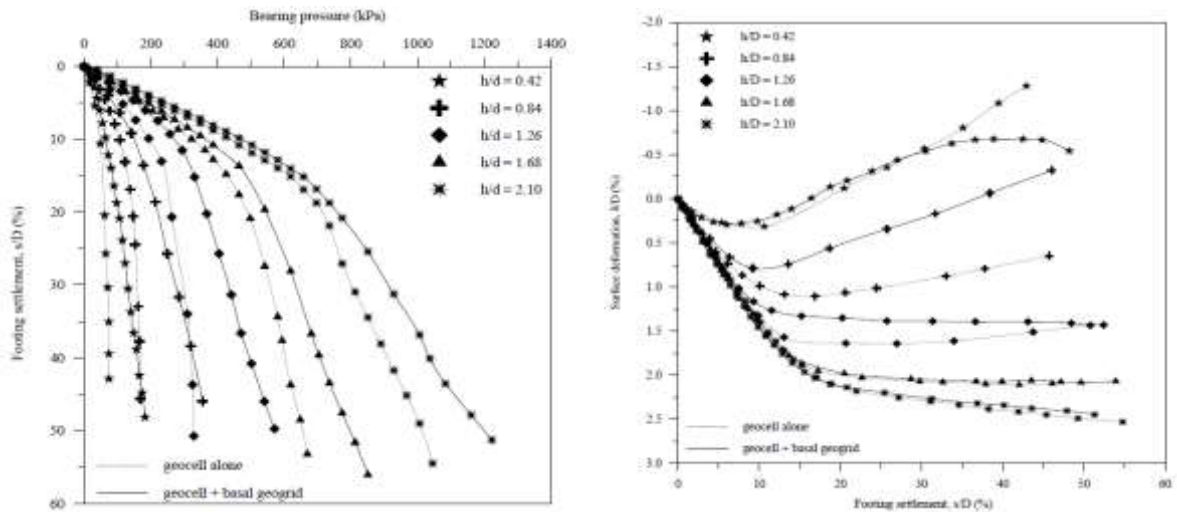


Figure 2.5: Variation of Bearing Pressure on Footing Settlement for Different Heights of the Geocell Mattress with and without Geogrid Layer - Test Series C and D. Dash et al, (2003)

The results of this investigation show that by including geocell reinforcement in the overlaying sand layer, a significant enhancement in load-carrying capacity and a decrease in the amount of surface heaving of the base layer can be attained. when another layer of geogrid is inserted at the base of the geocell mattress to improve the subgrade load-carrying capacity and stiffness, by incorporating geocell reinforcement and a basal geogrid layer into the underlying soft clay sand bed, the bearing capacity of the circular foundation can be increased substantially.

➤ **Stability of geocell-reinforced Soil**

Engineers frequently encounter challenges when beginning new construction projects on soft clay, since no firm strata were found within a depth of 15 m. The incorporation of a geocell reinforcement produces a comparably tougher stratum on top of the soft subgrade. To assess the influence of the geocell configuration—that is, the size and height of the geocell opening on the failure settlement and the bearing capacity of a two-layer system, experimental research has been conducted on the stability of a geocell-reinforced soft soil

structure. To investigate load versus settlement characteristics, enhancement in ultimate bearing capacity, and reduction in settlement, laboratory model tests were conducted on strip footing placed on top of marine clay covered by a sand layer with and without the geocell reinforcement. In the current work, experiments were carried out to investigate how bearing capacity changes because of geocell size at constant geocell height. Based on the trial results, an improvised bearing capacity factor has been proposed. Load vs settlement curves were drawn for each of the experiments. In all these experiments punching failure was observed. To identify the failure clearly, the load Versus settlement diagrams were drawn in the dimensionless form of $(p/d\gamma)$ vs (w/γ) , where p is the average bearing pressure. d is the dimensionless factor given by De Beer. The bearing capacity of the sand layer is one of the main properties of a subgrade, which was theoretically calculated using $q_s = 0.5\gamma BN\gamma$ which is obtained from Meyerhof and Hanna. The average modified bearing capacity can be found by dividing the ultimate bearing pressure by sand layer thickness. (γ = unit weight of sand and B = footing width). J. N. Mandal; P. Gupta, (1993)

Table 2.3: Properties of Geocell Structure J. N. Mandal; P. Gupta, (1993)

No.	Title	Values
1	Expanded dimension	$60 \times 30 \times 7.3 \text{ cm}^3$
2	Collapsed dimension	$7.5 \times 5 \times 7.3 \text{ cm}^3$
3	Panel thickness nominal	0.363 cm
4	Weight	
5	Cell area	26.6 cm ²
6	Cell seam node pitch	7.2 cm
7	Glue/seam	1
8	Seam tensile peel strength	1700 N m ⁻¹
9	Installation temperature	24–30°C
10	Material of geotextiles	Polypropylene
11	Colour	White
12	Chemical resistance	Medium
13	Frictional efficiency (E_f)	0.74

For each value of the geocell opening size, the modified bearing capacity factor rises

exponentially with a change in layer thickness. The stiffness of the upper elastic layer over soft marine clay increases with the thickness of the layer.

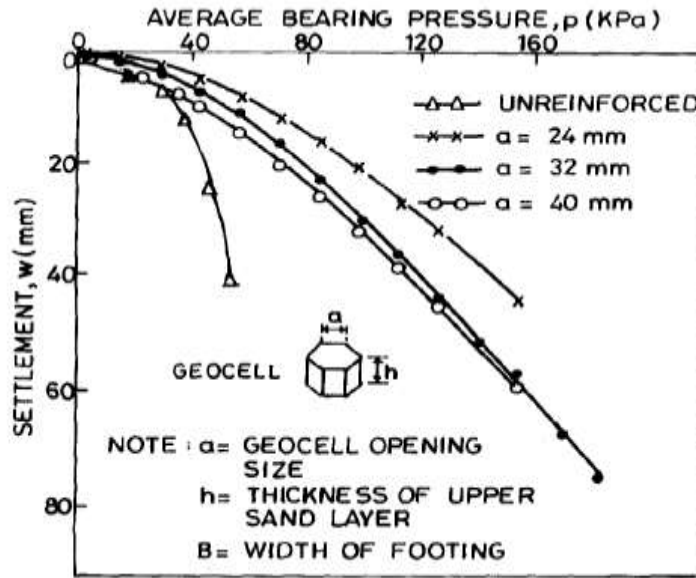


Figure 2.6: Load-Settlement Curves of Strip Footing on an Unreinforced and Geocell-Reinforced Layer Over Soft Marine Clay J. N. Mandal; P. Gupta, (1993)

The failure wedges in the unreinforced case were entirely confined in the sand layer at $h/B = 1.625$. The bearing capacity of geocell-reinforced soil exceeds that of unreinforced soil significantly as it enhances the bonding between the soil particles. The geocell layer's combination of beam and membrane action increases bearing capacity and keeps the failure wedges from coming into contact with the soft subgrade that is lying underneath it. Up to a settlement ratio of 5–10%, the geocell layer depicts beam action. Beyond 20% of the settlement ratio, the geocell layer displays membrane action. Both the thickness and the size of the geocell openings improve the bearing capacity. The addition of a geocell layer greatly increases the initial stiffness of the overlying sand layer. The initial stiffness is larger when the geocell aperture size is smaller and the geocell depth is greater. The implementation

of geocell reinforcement has proven to improve the load versus settlement characteristics of the subgrade. J. N. Mandal; P. Gupta, (1993)

➤ **Influence of Relative Density of Soil on Performance of Geocell-Reinforced Sand Foundations**

This research investigates the effect of the relative density of foundation soil on geocell reinforcement and its influence on the enhancement of performance using model load laboratory tests on the geocell-reinforced and unreinforced sand subgrade. The laboratory experiments were conducted on a steel-framed tank measuring 1,200 mm in length, 332 mm in width, and 700 mm in height. The steel model footing measuring 330 mm in length, 100 mm in width, and 25 mm in thickness was used for testing the soil subgrade. The soil utilized is poorly graded sand with an effective particle size D_{10} of 0.22 mm and an average particle size D_{50} of 0.46 mm. (Dash, 2010). The lowest void ratio E_{min} as established by an ASTM 2006b vibratory table is 0.474. The maximum void ratio E_{max} according to ASTM 2006a is 0.795.

The geocell reinforcement was constructed utilizing a polymer biaxial geogrid with an aperture opening size of 35 X 35 mm, an ultimate tensile strength of 20 kN/m, and a 5% strain secant modulus of 160 kN/m (ASTM 2001). The geogrids were cut from entire rolls to the necessary height and length, and then they were arranged with bodkin joints in both transverse and diagonal orientations to construct the geocell mattresses. Sandy subgrade was tested at five different relative densities: 30, 40, 50, 60, and 70%. In the laboratory steel test tank, these relative densities were attained through a calibrated sand raining apparatus. Electrical resistance-type strain gauges with 10-mm length, 2-mm width, 120-ohm resistance, and 2.1-gauge factor were used to determine the strain in the geocell

reinforcement. Two distinct series of model experiments were conducted by altering the relative density of soil from loose to dense, i.e., ID =30, 40, 50, 60, and 70%. Unreinforced soil subgrade was used for testing in the first series. Soils equipped with geocell reinforcement were used for testing in the second series. The stiffness of the geocell-reinforced sandy soil subgrade can be expressed by the subgrade modulus (k_r), which is usually determined by the secant modulus of the pressure-settlement responses curve, or the slope of the line connecting the point on the curve at a certain settlement to its origin as presented in Figure 2.7 (A). The relationship between the relative density of soil and the differential incrementation of subgrade modulus of the geocell-reinforced subgrade soil (k_r) at various footing settlement levels (s/B) is shown in Figure 2.7 (B). It demonstrates that as the relative density of soil improves, correspondingly increments the subgrade modulus of the geocell-reinforced foundation soil (k_r).

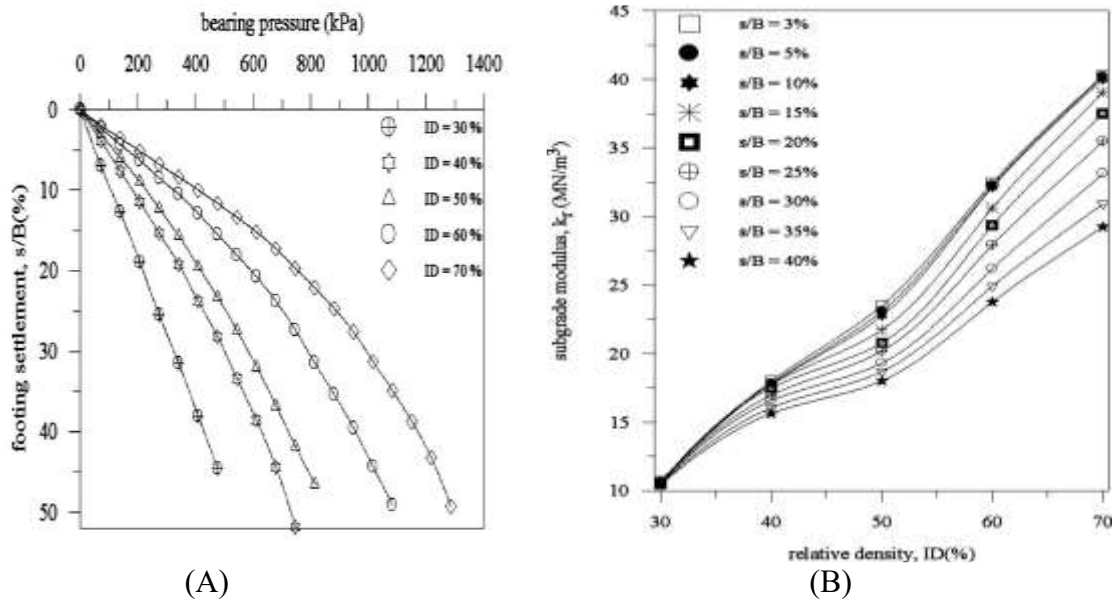


Figure 2.7: (A) Bearing Pressure Versus Footing Settlement And (B) Subgrade Modulus Versus Relative Density for Geocell Reinforced Foundation Bed (Dash, 2010)

With an increase in soil density from 30% to 70%, the subgrade modulus value increased from about 10 MN/m³ with ID = 30% to approximately 40 MN/m³ with ID = 70%. This suggests that the stiffness of the geocell-reinforced foundation soil has inflated fourfold. This indicates that the subgrade modulus and the bearing capacity of the soil increase due to the influence of geocell reinforcement. Figure 2.8 depicts the various strain distribution patterns in the geocell wall for the dense state ID = 70% and loose state ID = 30% of the soil stratum. Compressive strains can be observed to be generated quite near to one another in the vicinity of the geocell mattress's two free ends when there is a dense soil stratum. Since the soil mass gets dilated surrounding the region of loading, eventually forces the soil mass to expand and evade the pressure bypassing through the openings present in the geocell walls. The sand in the nearby stable zone restricts this confined transverse expansion. A constraint of this kind compresses the soil mass, which in turn compresses the geocell wall.

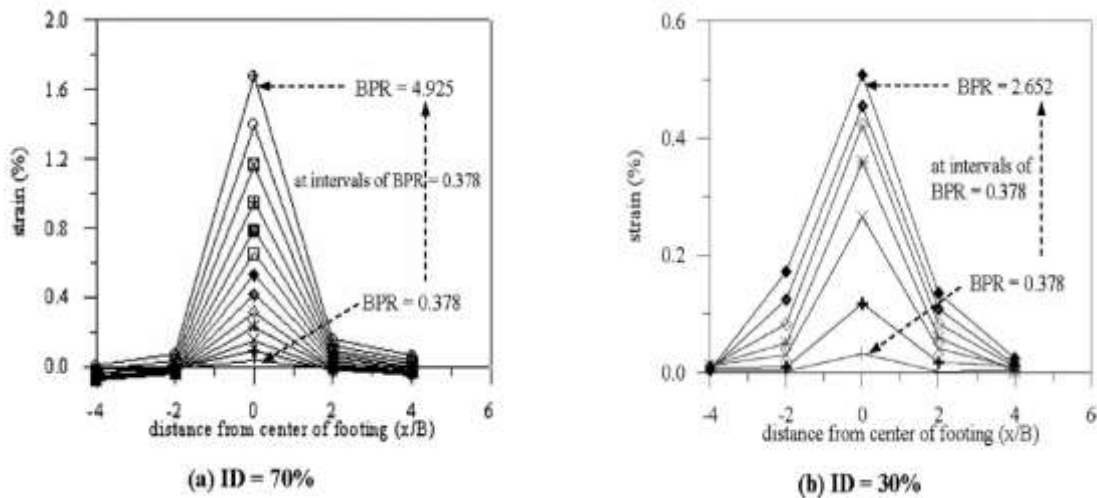


Figure 2.8 Strain in the Geocell Wall for Soil At 70 and 30% Relative Density (Dash, 2010)

Whereas, in the 30% relative density state the soil subgrade is kept in its loose state, thus the compression strains were very low in the free ends of the geocell mattress. The

advantageous effects of geocell reinforcement were apparent over a wide range of relative densities (ID=30–70%}); however, they were significant for dense conditions of foundation soil. These effects encompass an increase in stiffness, bearing capacity, and load dispersion angle of the foundation bed.

➤ **Bearing Capacity of Strip Footings Supported on Geocell-Reinforced Sand**

A more resilient geocell reinforcement mattress is placed underneath to support the foundation, which stops the in-fill soil's lateral spreading and enhances the load-carrying capacity of the soil structure. The outcomes of laboratory-model testing on a strip footing underpinned by a sandy subgrade reinforced with a geocell mattress were presented in this study. The geocell construction pattern, pocket size, height, width, depth to the top of the geocell mattress, tensile strength and stiffness of the geogrids used to construct the geocell mattress, and the relative density of the sand were among the elements that varied in the testing procedure. The steel tank used for the model experiments was 1200 mm long, 332 mm wide, and 700 mm high. To prevent collapsing during testing, the tank's two long sides, composed of a 15 mm thick Perspex sheet, were anchored laterally on the exterior using mild steel angles. The steel model's foundation had dimensions of 330 mm in length, 100 mm in breadth, and 25 mm in thickness. The footing was positioned in the middle of the tank, its length parallel to the breadth of the soil tank. The footing's length and tank width were almost equal to simulated plane strain characteristics throughout the test setup. 1 mm wide space was left on either side of the tank to avoid the footing and side walls coming into touch. The properties of the different types of geogrids used in this study to construct geocells are presented in Table 2.4.

Table 2.4: Properties of Geogrids (Dash et al., 2001)

Parameter	Descriptions		
	BX	NP-1	NP-2
Ultimate tensile strength (kN/m)	20	4.5	7.5
Failure strain (%)	25	10	55
Initial modulus (kN/m)	183	75	95
Secant modulus at 5% strain (kN/m)	160	70	70
Secant modulus at 10% strain (kN/m)	125	45	50
Aperture size (mm)	35 × 35	50 × 50	8 × 7
Aperture opening shape	Square	Square	Diamond

Three distinct geogrid types were used for constructing the geocells: the first kind, known as the biaxial grid (BX), is composed of oriented polymer, while the other two, known as the NP-1 and NP-2 grids, were composed of non-oriented polymer. The geogrids were cut into the required length, and height and then distributed into two different patterns to attain diamond-pattern geocell and chevron-pattern geocell panels. The geogrids were oriented in transverse and diagonal directions and the joints were interlocked with bodkin joints (plastic strips). Below Figure 2.12 depicts the distribution pattern of geocell.

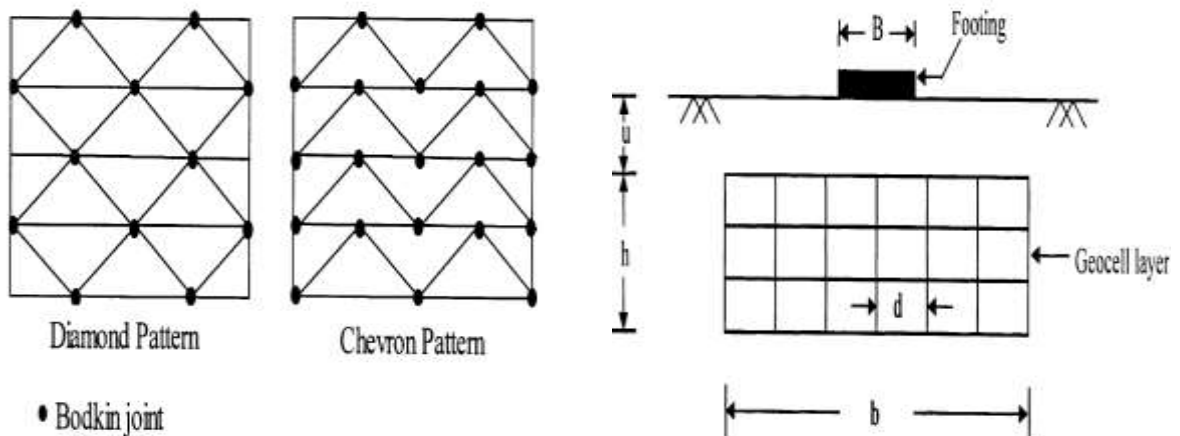


Figure 2.9: Geocell Distribution Pattern and Geocell-Reinforced Foundation Bed (Dash et al., 2001)

There were several series of tests that were executed on the footing which were supported by two different geocell orientation patterns, and variable parametric changes such as the

d/B ratio, h/B ratio, relative density, b/B , and u/B ratio which differ as per the test series. The below Table 2.5 below is a detailed view of differences in all these aspects as per the test series. The present study's findings lead to the following conclusions concerning the performance of strip footings superimposed on geocell-reinforced sand beds. When strip footing is placed on geocell-reinforced sand, its pressure-settlement response is roughly linear. It is evident even under loads that were almost eight times the unreinforced footing's maximum capacity and settlements of around 50% of the footing wide.

Table 2.5: Details of Model Test Series (Dash et al., 2001)

Test series	Details
A	Tests on unreinforced sand with relative densities (ID) of 30, 40, 50, 60, 70%
B	Variable parameter: Patterns of geocell formation: chevron, diamond Constant parameters: $d/B = 1.5$, $h/B = 0.8$, $b/B = 12$, $u/B = 0.1$, geocell made of BX grid, ID = 70%
C	Variable parameter: $d/B = 1.2, 1.5, 2.7$ Constant parameters: Chevron pattern, $h/B = 0.8$, $b/B = 12$, $u/B = 0.1$, geocell made of BX grid, ID = 70%
D	Variable parameter: $h/B = 0.8, 1.6, 2.0, 2.75, 3.14$ Constant parameters: Chevron pattern, $d/B = 1.2$, $b/B = 12$, $u/B = 0.1$, geocell made of BX grid, ID = 70%
E	Variable parameter: $b/B = 1, 2, 4, 6, 8, 10, 12$ Constant parameters: Chevron pattern, $d/B = 1.2$, $h/B = 2.75$, $u/B = 0.1$, geocell made of BX grid, ID = 70%
F	Variable parameter: $u/B = 0.0, 0.1, 0.25, 0.5, 0.75, 1.0, 1.5$ Constant parameters: Chevron pattern, $d/B = 1.2$, $h/B = 2.75$, $b/B = 8$, geocell made of BX grid, ID = 70%
G	Variable parameter: Geocell materials: BX, NP-1, NP-2 grids Constant parameters: Chevron pattern, $d/B = 1.5$, $h/B = 1.2$, $b/B = 8$, $u/B = 0.1$, ID = 70%
H	Variable parameter: ID = 30, 40, 50, 60, 70% Constant parameters: Chevron pattern, $d/B = 1.2$, $h/B = 1.6$, $b/B = 8$, $u/B = 0.1$, geocell made of BX grid.

Since the footing loads were transferred to greater depths through the geocell layer, significant enhancements in the footing behavior can be achieved even with a geocell mattress whose width is equal to the footing's breadth. A geocell adequate in size to prevent the rupture plane from emerging within the foundation soil may significantly decrease surface heave. Performance is significantly improved up to a geocell height of twice the footing's width. Its enhancement is minimal above that point. For optimal beneficial characteristics, the geocell mattress's top should be situated $0.1B$ beneath the footing's slab. Geocells formed in a chevron design were more advantageous than those in a diamond layout. To assess the effectiveness of a geocell mattress, the tensile strength of the grid utilized to construct it is inadequate, apart from that the geocell-reinforced foundation bed's load-bearing mechanism is partly influenced by the size of the aperture and the orientation of the ribs within the grid structure. Due to dilation-induced weight transfer from soil to geocell, the soil must be filled in the geocell pockets and compacted to a dense state which will increase footing performance significantly. subsequently, it was discovered that a geocell pocket's ideal aspect ratio for sustaining strip footings was approximately 1.67.

2.4 Exploration of TDA Reinforced Concrete

Scrap tire rubber material is a catastrophic worldwide issue due to the scarcity of landfills and the health risks connected to these waste dumps. Tire rubber accounts for a significant component of the solid waste that has evolved into a global environmental concern. Considering the tremendous rise of the world population, recycling abandoned scrap solid tire waste is one of the most difficult issues in the world. Aside from the ecological advantages attained from recovering huge quantities of discarded tire waste, utilizing these

tire rubber particles creates an innovative concrete mix with distinct mechanical and structural properties. A tire is a combination of rubber elastomer sheets solidified with transversely running steel fibers, nylon threads, and cables. Natural rubber, when formed into rubberized materials, exhibits excellent tensile and shear strength with exceptional fatigue resistance. Rubber has great adherence to metallic wiring and minimal hysteresis, which contributes to its long-term integrity. CATRA members contribute to Canada's sustainable economy by enabling the reuse of previously discarded resources into profitable products. Their commitment to this purpose is reflected in their continually elevated diversion rate. Overall, our Canada-wide member programs achieved nearly 100% diversion. Our programs coordinate the safe and responsible diversion of used tires from landfills and stockpiles, including PLT (passenger and light truck), MT (medium truck), and OTR (off-the-road) tires. Tire recycling programs in Canada have established the groundwork for new businesses that turn old tires into new goods. This is particularly true in the fields of molded goods, crumb rubber, aggregate made from tires, and gasoline made from tires.

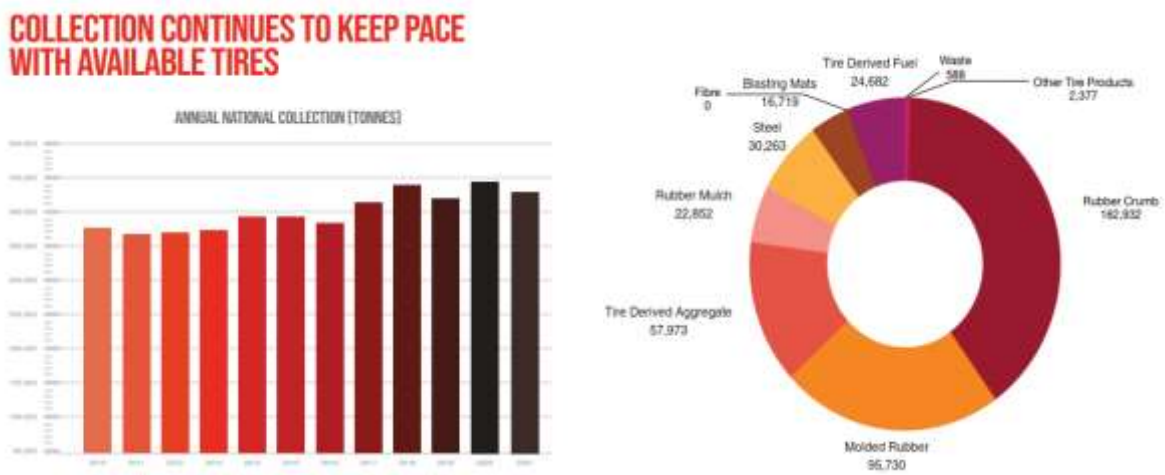


Figure 2.10: CATRA Annual Report 2022

From the year 2016 onwards, every year more than 400,000 tonnes of waste tire collection have been recorded. In the year 2022 around 437,000 tonnes of scrap tires were procured and recycled into useful products. Based on the report around 414,116 tonnes of end-life tires were diverted from waste stockpiles and recycled into distinct valuable resources, amongst which 57,973 tonnes of scrap tires were converted into tire derivative aggregates.

➤ **Mechanical, Fracture, and Microstructural Investigations of Rubber Concrete**

(Reda Taha et al., 2008), The mechanical, fracture, and microstructural properties of concrete mixes containing tire rubber aggregates brought in as coarse and fine aggregate replacements were investigated in this research. Tire derivative aggregates that had been chipped and crumbed were utilized to substitute coarse and fine aggregates, correspondingly. The coarse and fine aggregate substitution amounts were 25, 50, 75, and 100% by volume. The tire rubber has been shredded into two distinct sizes: 5 to 10 mm and 10 to 20 mm. The two categories of shattered tire rubber fragments were combined in a 1:1 ratio. The size of the crumpled tire rubber fragments varied between 1 to 5 mm. Crushed stone that complied with {ASTM 2003} aggregate specifications constituted the coarse aggregate. The sand exhibited a fineness modulus of 2.3 and was naturally siliceous sand. A sieve analysis of the fine and coarse aggregate was performed with the broken and crumbled tire rubber fragments. The concrete mix proportions with various percentages of fine and coarse aggregate replenishment with chipped and crumbled tire aggregates are shown in Table 2.6 Concrete Mix Proportions. The testing of mechanical properties involved calculating the impact resistance strength at 28 days in addition to evaluating the compressive strength at 7 and 28 days. Three separate specimens of each batch of rubberized concrete mix were utilized for every test. It was

essential to regulate the air concentration of fresh rubberized concrete mix due to the tire rubber particles' low Young's modulus.

The aggregate correction factor was calculated by applying the calibrated force to a sample of coarse and fine aggregate, which included rubber tire fragments in roughly the same moisture condition, amount, and percentages as existing in the concrete sample. The concrete was cast into beam dimensions measuring 100X100X500 mm. The impact test was conducted with the help of a drop hammer rig. To execute the test, a 10 kg drop hammer was dropped from a typical 60 mm height exactly at the beam's midspan. The impact energy (IE) is calculated as the energy acquired by the specimen until failure.

Table 2.6: Concrete Mix Proportions (Reda Taha et al., 2008)

Aggregate replaced by tire particles	Replacement ratio (%)	Portland cement (kg/m ³)	Water (kg/m ³)	Coarse aggregate (kg/m ³)	Fine aggregate (kg/m ³)	Chipped rubber (kg/m ³)	Crumbed rubber (kg/m ³)
Coarse aggregate	0	350	200	1,160	630	—	—
	25			870	630	290	—
	50			580	630	580	—
	75			290	630	870	—
	100			—	630	1,160	—
Fine aggregate	25	350	200	1,160	472	—	158
	50			1,160	315	—	315
	75			1,160	157	—	473
	100			1,160	—	—	630

$$IE = \sum_{i=1}^{N_f} w_i h_i$$

where

w_i = drop hammer weight equal to 10 kg = 0.1 kN

h_i = height of drop hammer being 60 mm

N_f = the total number of drops up to failure

Rubberized concrete's fracture toughness was assessed using both notched and unnotched beams. For every rubberized concrete mix, three samples of each specimen type were examined. The testing beams had dimensions of 100 mm in width, 75 mm in depth, and 350 mm in length. They were loaded across a 300 mm span, implementing a four-point bending technique, and were equipped with a 4.0 span/depth ratio. A carbide saw having a 3 mm width was used to notch the specimens. The initial notch in the notched specimens was 25 mm deep. A response signal from linear variable differential transducers, or LVDTs, which measure the midspan deflection, was used for the testing. The specimens failed progressively and under control as a result of this feedback technique. Both the applied load and the midspan deflection were consistently recorded.

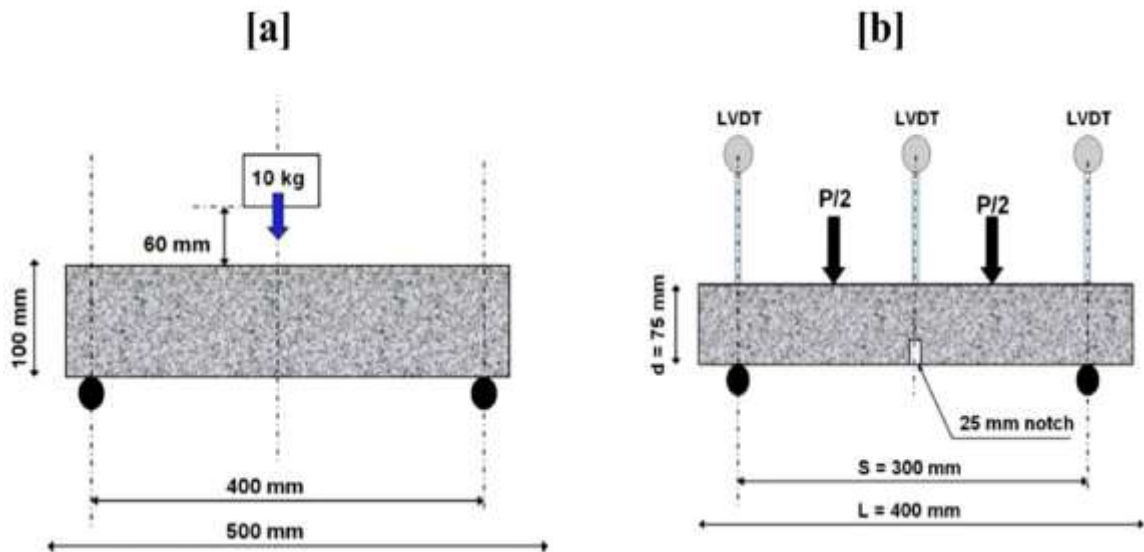


Figure 2.11: Schematic Representation of A. Impact Test Setup B. Fracture Toughness Test Setup (Reda Taha et al., 2008)

To reduce the inaccuracy caused by specimen deformation at the supports, two additional LVDTs were installed there. The stress was imposed steadily for 180 seconds, attaining its peak load after around 30 seconds. The data-gathering system was used to gather load and displacement measurements at a sampling frequency of 5 Hz. The unit weight of the fresh

and hardened concrete has dropped by using tire derivative aggregate in place of coarse and fine aggregates. The reduction in unit weight is attributed to two other factors. First, it entraps air in the jagged surface, second low specific gravity of Tire aggregates. Despite having an average specific gravity of approximately 1.10, the tire aggregates specific gravity allowed them to float in water, validating the theory that they were entrapping air. Conversely, when the amount of tire aggregate increased, there was a noticeable decrease in the slump of the rubber concrete, indicating that increasing the tire rubber content had a negative impact on the workability of fresh concrete.

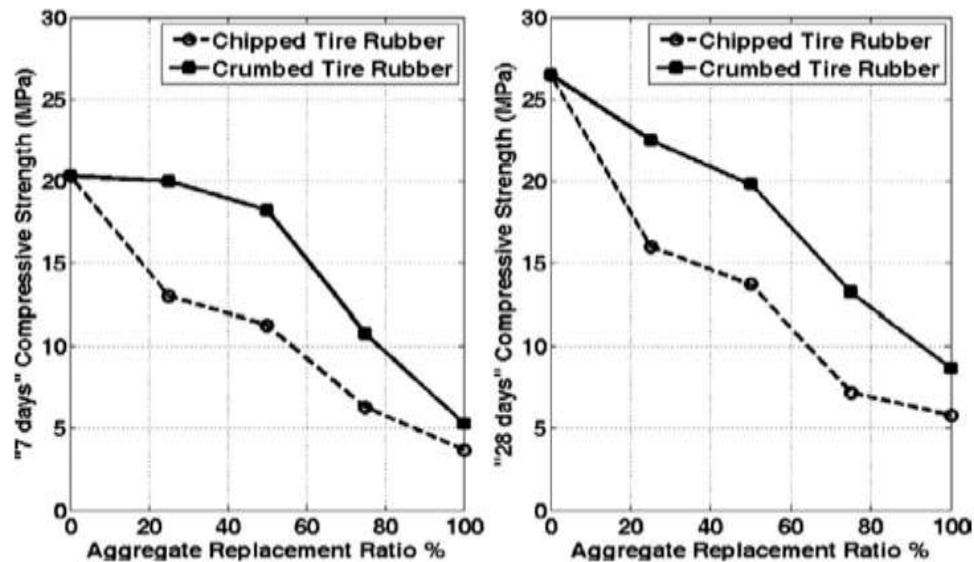


Figure 2.12: Compression Strength of Rubber Concrete (Reda Taha et al., 2008)

For substitution percentages of 25, 50, 75, and 100%, respectively, the 7-day compressive strength was reduced by 1, 10, 47, and 74% when crumbed tire aggregates were implemented in place of fine aggregate. The 7-day compressive strength diminished by 36, 44, 69, and 82% for substitution percentages of 25, 50, 75, and 100%, respectively, when chipped tire aggregates were used as a substitute for coarse aggregate. Furthermore, for substitution percentages of 25, 50, 75, and 100%, respectively, the 28-day compressive

strength diminished by 15, 25, 50, and 67% when crumbed tire rubber particles were used instead of fine aggregate. Likewise, for 25, 50, 75, and 100% substitution percentages, respectively, the 28-day compressive strength declined by 40, 48, 73, and 78% when chipped tire aggregates were used instead of coarse aggregate. Based on the percentage of aggregate substitution by tire particles R , a model to forecast the 28-day compressive strength of rubber concrete F_{RC} can be expressed as follows.

$$f_{RC} = f_C - 0.1236R - 0.0006R^2$$

$$f_{RC} = f_C - 0.4496R + 0.004R^2 - 1.65 \times 10^{-5}R^3$$

Where,

f_C = 28 days compressive strength of concrete without tire rubber particles

R = replacement percentage of the aggregate with tire rubber particles.

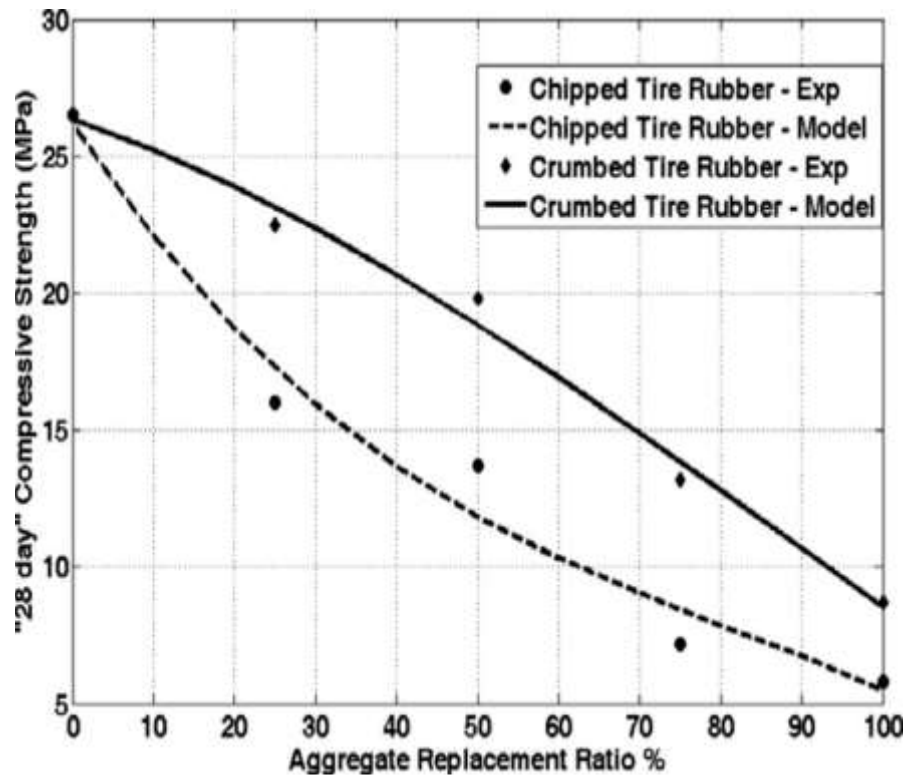


Figure 2.13: Experimental Vs Analytical Model (Reda Taha et al., 2008)

The experimental findings were compared with the analytical model predictions for the 28-day compressive strength of rubber concrete at different percentages of aggregate substitution with tire aggregates. Investigating the rubber-concrete interface's microstructure suggested that the area surrounding the tire aggregate may have significant microcracking. It is evident that, depending on the application, the optimal substitution ratio of tire aggregate in rubberized concrete should be determined by maintaining an equilibrium between strength and fracture toughness.

➤ **Using TDA To Partially Replace Coarse Aggregates in Concrete Mixtures**

Rubberized concrete has significantly increased in various applications over the past decade as an alternative to the problems of waste tire accumulating and the related environmental concerns. This research aims to examine the impact of substituting coarse aggregates in concrete mixtures with recycled Tire Derived Aggregates (TDA). A portion of the 0.5-inch coarse aggregates utilized in the regular concrete mixtures were substituted with 10%, 20%, and 30% TDA. Conventional concrete mix is deficient in impact resistance, damping qualities, and toughness which were desired attributes of dynamic load resistance. In reality, when exposed to extremely sudden dynamic forces, structures that are not impact-resistant may sustain significant damage and fractures. The addition of TDA would provide concrete mixtures with the necessary seismic resistance and damping capabilities. (Naggar et al., n.d.)

To minimize the impacts of experimental error and be certain that the test data delivered precise and accurate results, three (150 mm X 300 mm) cylindrical specimens were prepared for each TDA content. TDA-0 denotes a regular concrete mix with 0% TDA,

TDA-10 denotes a mix with 10% volume of coarse aggregate substituted with TDA, and furthermore. (Naggar et al., n.d.)

Table 2.7: Test Matrix (Naggar et al., 2019)

Specimen ID	TDA content (%)	Number of specimens
TDA-0	0	3
TDA-10	10	3
TDA-20	20	3
TDA-30	30	3
Total	-	12

The size of coarse aggregate in gravel was 0.5 mm. Similarly, the TDA aggregate sizes were 4.75 mm to 19.05 mm; any aggregate size outside of these ranges was eliminated. ASTM C-136 sampling method along with sieve analysis were used to segregate the required amount of TDA quantity according to the required size. ASTM C29 was used to determine the bulk density of the aggregates. The bulk density for coarse, fine, and TDA aggregates was 1601, 1817, and 557 kg/m³, respectively. (Naggar et al., 2019). 12 concrete cylinders of 150mm X 300mm were constructed as shown in Table 2.7. A 2 MN universal testing machine was used in this investigation. A uniaxial compression test, which was performed at a rate of 0.5 mm/min utilizing a displacement control technique was imposed on the concrete cylinders. Four linear potentiometers (LVDTs) displacement gauges were placed on a two-steel ring yoke setup around the concrete specimens to measure the lateral and horizontal displacements. (Naggar et al., 2019).

The standard deviation, which demonstrates little variation in test results from the mean, fluctuates between 0.6 to 1,96 MPa. Substitution of 10% (by volume) of the coarse aggregates with TDA results in a 29% reduction in compressive strength. Following that, the strength reduction rate drops and stabilizes at 34% and 36%, respectively, in comparison to the control specimen with 20 and 30% of TDA. The elastic modulus of

concrete drops by 8, 11, and 17% in comparison to the control specimen's elastic modulus when the TDA concentration is increased to 10, 20, and 30%, respectively. The result shows it is evident that TDA has a less detrimental effect on elastic modulus than it does on concrete's compressive strength. The blue bar graph exposes the difference in compressive strain at peak load according to TDA content. When the TDA concentration is increased to 10, 20, and 30%, the strain enhances to 12, 26, and 37% compared to the control specimen. Based on the behavior, it appears that following the initial cracking, the TDA produces numerous microcracks. This gives a practical sense, as concrete compressive strength decreases.

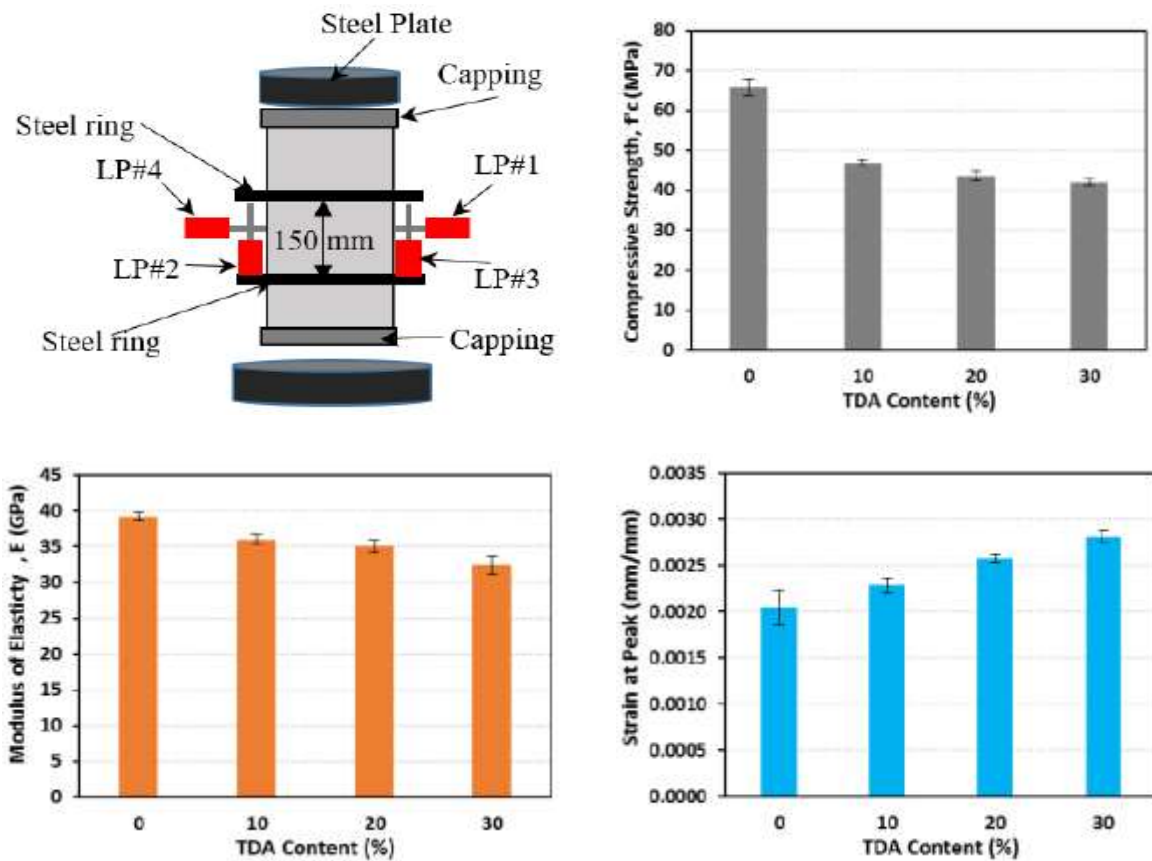


Figure 2.14: Test Setup, Compressive Strength, Elastic Modulus, Strain at Peak of TDA Concrete Cylinder (Naggar et al., 2019)

Through experiments by analyzing the behavior of concrete combined with aggregates obtained from tires, we were able to determine that the total compressive strength and elastic modulus of the concrete reduces as the TDA concentration rises. Furthermore, compared to plain concrete, the incorporation of TDA into the mixture produced concrete with ductile post-peak behavior.

➤ **Evaluation of the Incorporation of Tire-Derived Aggregates (TDA) in Rigid Pavement Mix Designs**

Tire-derived aggregate (TDA) is an innovative building material made from recycled tires broken down into small fragments between 12 and 305 mm. TDA weighs 70% less than regular gravel and offers beneficial qualities in addition to maintaining its structural integrity. Numerous investigations have been carried out to examine the effects of TDA addition to PCC mixtures. Results indicate that although a higher rubber percentage increases material toughness and ductility, it negatively affects the desirable PCC mechanical characteristics. Therefore, this study aims to examine the consequences of using tire-derived aggregates (TDA) instead of coarse aggregates. coarse aggregates were substituted with 0, 10, 20, 40, 60, 80, and 100% TDA by volume in PCC mixes, and the specimen's characteristics were examined in a research facility.

As per ASTM C136, sieve analysis was performed to obtain the recycled TDA rubber under the required size, particles larger than 19 mm were discarded, and the necessary amount of TDA was gathered. Seven concrete mixes with various TDA percentages were made to examine the impact of adding TDA to PCC blends. A control mix containing zero percent TDA was also made for comparison. For every mix, the volume of FA, the volume of water, the W/C ratio, and the proportion of cement content remained unchanged. From each

combination, three 150 mm diameter by 300 mm high cylinders and 150 x 150 x 500 mm beams were constructed to determine the average for each TDA combination examined. The ASTM testing protocols ASTM C39, ASTM C469M, and ASTM C78, respectively, were used to determine the impact of each TDA content on the concrete's 28-day compressive strength, elastic modulus, and flexural strength (Abu Abdo & El Naggar, 2022).

From Figure 2.15 the compression strength on the 28th day obtained for the seven TDA variant concrete mix can be examined and compared. From the bar graph, it is evident that there is a reduction of compressive strength for concrete mix with a higher TDA percentage when compared to the no TDA control specimen. The control specimen had a compressive strength of 39.8 MPa. On comparing the results, a 25% strength drop was reported for a mix in which TDA substituted 10% of the coarse aggregate with a strength of 29.8 MPa, and for 20% TDA substitution around 34% of strength got reduced (26.5 MPa). In comparison, a 79% strength reduction was recorded for a mix in which 100% TDA (9.2 MPa) was utilized. This diminution in strength is mostly due to the poor stiffness of rubber in comparison to the other concrete elements once the initial crack is exerted by the load TDA in the concrete compresses and leads to the development of several micro-cracks. Thus, the rubber functions as a void in the concrete matrix. Moreover, the smooth surface of the rubber causes limited adhesion between the tire derivative aggregates and the cement mixture.

Although the incorporation of rubber into concrete mix significantly increases its ductility but decreases its modulus of elasticity which can be observed through the second graph in Figure 2.15. In comparison to the control specimen containing 0% TDA which

had an elastic modulus of around 33,500 MPa, for 10% TDA blended concrete mixtures the elastic modulus diminished by roughly 36% with a modulus of almost 21,500 MPa, in terms of 20% TDA reinforced concrete there was a decrement of 48.5% exhibiting a modulus of about 17,200 MPa, and about 84% in concrete mixtures with 100% TDA as it had significantly very less amount of elastic modulus(nearly 5800 MPa).

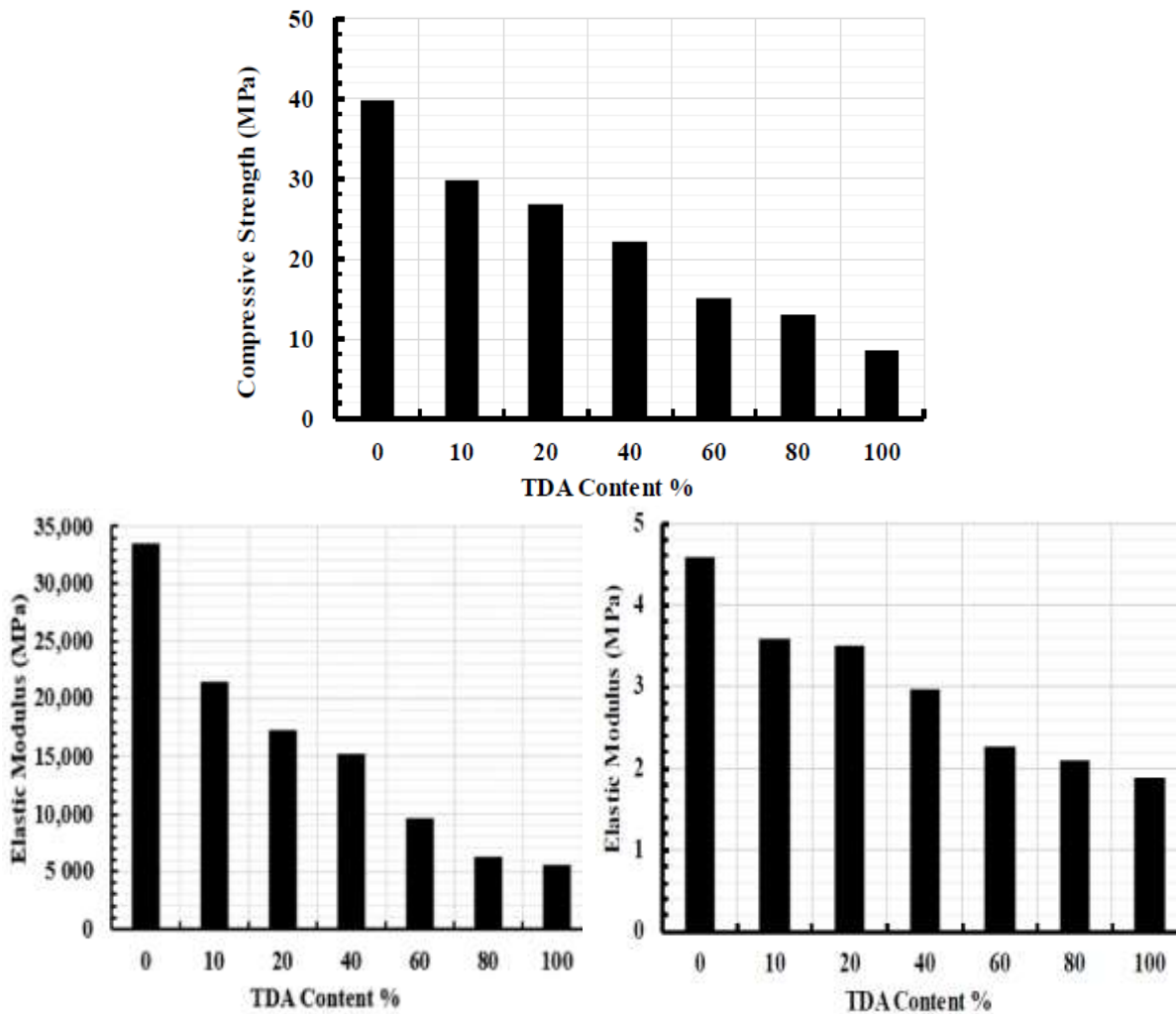


Figure 2.15: Variation of Compression Strength, Elastic Modulus, and Modulus of Rupture of TDA-Reinforced Concrete (Abu Abdo & El Naggar, 2022)

Congruent with the apparent loss in compressive strength, the study's results indicate a comparable decline in the flexural strength of TDA-reinforced concrete. The third bar

graph in Figure 2.15 exposes the variation in the modulus of rupture plotted against the TDA percentage utilized in the concrete. The control specimen had a flexural strength of 4.6 MPa. When comparing the outcomes of all 6 variants of TDA reinforced with the control specimen, it is evident that 10% TDA reinforced concrete has a fall of 22% with a strength of 3.6 MPa, the 20% TDA-reinforced concrete specimens having around 3.5 MPa exhibited a reduction of 24% of flexural strength and then it started to drop significantly from 30% TDA content. The 100% TDA-reinforced concrete specimens gave flexural strength of 1.85 MPa, leading to a decrease of 59% in flexural strength. To conclude, the advantages of using TDA surpass any potential decrease in rigid pavement's ability to withstand cracking. Furthermore, the application of TDA increases the concrete mixture's flexibility, which can aid in lowering the possibility of failure and increase endurance in various loading circumstances. In proportion to the TDA content, the concrete's strength and stiffness declined. Concrete slabs with TDA provided more ductility and flexibility than concrete mixes without TDA. Due to the influence of TDA the concrete slabs become more elastic, which enhances the deflection resistance significantly more than the no TDA slab. Therefore, as this study has shown, environmentally friendly, long-lasting rigid pavement design solutions can be achieved by substituting coarse aggregates with TDA during the construction of concrete pavements.

➤ **Lightweight Rubberized Concrete Slabs for Sustainable Road Pavements Serving Non-Auto Traffic**

Over the past decades, Bike paths and walkways have been examples of non-automotive transportation systems that effectively facilitate physical means of transit. Enhancing the environmentally and economically advantageous design and construction

of the concrete slabs with TDA, that make up these types of transport routes can contribute to lower maintenance costs as well as the use of recyclable waste substances. This paper examines the use of recycled tires - tire-derived aggregate (TDA), in conjunction with expanded clay (EC) produced in rotary kilns as coarse aggregates in concrete, along with a life-cycle cost analysis. Three mix designs were calculated for this project based on ACI 211.1. The control mix (Mix A) has been designed only with expanded clay as the coarse aggregate, Mix B was designed to facilitate 80% TDA and 20% expanded clay as the coarse aggregate. Mix C was designed to replace 100% of the coarse aggregate utilizing TDA. The TDA contained no steel fibers, possessing a specific gravity of 1.15, a unit weight of 1150 kg/m³, and an average size of 9.525 mm. EC aggregates had a specific gravity of 1.73 and a unit weight of 1728.4 kg/m³.(Maryam Nazari et al, 2022).

This study combines a testing stage with a life-cycle cost analysis to assess lightweight rubberized concrete pavement slab performance and durability. Three mix formulations with varied TDA and expanded clay aggregate percentages were tested in concrete cylinders and beam specimens for compressive strength and flexural modulus of rupture. Subsequently, three slab structures were developed and constructed utilizing the three different concrete mixes. The fatigue durability of these slabs was assessed by subjecting them to many cycles of impact loading with a drop-weight impact machine. Slab impact-fatigue testing was utilized to quantify maintenance expenses throughout their lifespan.




The cylinder specimens were placed in the UTM machine and compressed according to ASTM standards with a loading rate of 4 kN/sec. The final attained compressive strength of the rubberized concrete mixtures was adequate to support the loads in non-automotive traffic pathways, even though MIX B had a 70% reduction in strength (6.3

MPa) and MIX C attained an 83% reduction of strength (3.6 MPa) when comparison to MIX A strength of 20.7 MPa.



Figure 2.16: CA And FA Used in Mix Design (Maryam Nazari et al, 2022)

Table 2.8: Test Specimen Types and Test Method (Maryam Nazari et al, 2022)

Test Specimen	Size/ Number of Specimens per Mix	Testing Procedure
	152.4 mm (diameter) × 304.8 mm (height) Cylindrical Specimens / 3	Compressive Testing following ASTM C39 Standard [19]
	152.4 mm square section × 533.4 mm (length) Beam Specimens / 3	Static Flexural Testing following ASTM C78 Standard [20]
	685.8 mm (length) × 457.2 mm (width) × 101.6 mm (thickness) Slab Specimens / 2	Impact-Fatigue Testing of Slab Assemblies

All beam specimens were subjected to four-point flexural loading by ASTM C78 to determine the stiffness and flexural strength (modulus of rupture) of the rubberized concrete specimens. These results were then compared to those obtained for the control specimen. To simulate the push-release loading condition that the specimens will experience during biking, these simply supported beams were exposed to half-cyclic static loading. The load cycle was executed with load increments of $0.25P_{cr}$ to $2P_{cr}$, where P_{cr} is the critical load measured based on compressive strength.

Table 2.9: Beam Specimen Experimental Results (Maryam Nazari et al, 2022)

Mix Design ^a	Max. Load, kN	MOR ^b , kPa (Experiment/Expected ^c)	Maximum Deflection, mm	Toughness Index (I_5/I_{10})
MIX A	29.4	3544/ 2131	2.03	1.04/1.05
MIX B	14.1	1779/ 1172	18.03	2.8/3.6
MIX C	10.85	1340/ 883	19.81	4.4/7.4

To assess the functionality of road pavement slabs that were used for walking and cycle paths, a sequence of impact-fatigue tests was performed on MIX A, B, and C slab structures. The procedure involved generating impact forces by lowering two 80-N weights from a height of 25.4 mm. The loads were fastened to two gears using a prefabricated 25.4 mm hole to ensure their free fall. The slabs were positioned in a soil box with a longitudinal orientation and fastened to the box at both ends with a set of springs having a stiffness of 62.75 N/mm to create the real constraint situation. To further secure the two slabs together and form a single unit, a No. 3 dowel rod was inserted inside each slab. Accelerometers, SPOTs, and strain gauges measured slab acceleration throughout dynamic impact loading and peak deformation/strain values.

TDA substituted expanded clay coarse aggregates concrete specimens, attained diminishing compressive strength and modulus of rupture. Adding more TDA reduced the strength of rubberized concrete, but it is still strong enough to support bicycle loads on non-auto-traffic routes. The failure pattern of cylindrical specimens with TDA revealed better ductility than the control specimen.

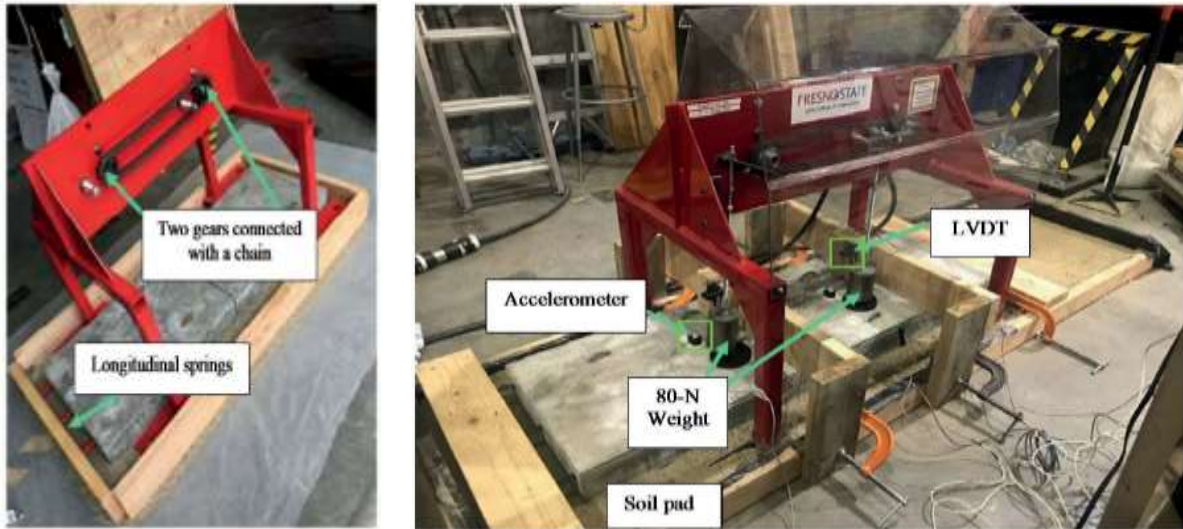


Figure 2.17: Impact-Fatigue Test Setup (Maryam Nazari et al, 2022)

Localized cracks were first noticed at the corners of MIX B and C specimens before failure, while MIX A specimens split into two pieces with one crack. As load increased actuator-induced vertical deflection on TDA-contained beam specimens exhibited cracks on the tensile face. Before the failure, MIX B and C beams had a substantial gap opening, but the control specimen's unexpected failure prevented tracking it. Impact-fatigue tests of slab structures showed that TDA-contained concrete pavements can withstand more loading cycles before failing. Using the TDA improved the service life of pavement slabs, TDA-reinforced concrete is ductile, flexible, and absorbs more energy than expanded clay-reinforced concrete.

2.5 Investigation of GFRP Reinforced Concrete Slab

Glass fiber-reinforced polymer (GFRP) is rapidly replacing steel in North American concrete flat-slab projects owing to its extremely lightweight nature, and excellent mechanical, structural, and durability performance. GFRP's inherent corrosion resistance and ability to transmit electromagnetic fields allow it to prolong the useful life of concrete structures. Establishing related rules and standards in recent years has contributed to this advancement. ACI 440.1R-15 design rules and ASTM D7957/D7957M-176 expose it as an excellent product. Slabs-on-ground is frequently designed using GFRP reinforcement for temperature and shrinkage reinforcement and structural reinforcement due to its lightweight, which makes it easier to transport, handle, and install, enabling a quicker and more effective construction. However, studies focusing on GFRP reinforcement for this particular slab-on-grade application were very limited.

➤ GFRP Reinforced Concrete Slab Under Restrained Shrinkage

The efficacy of glass fiber-reinforced polymer (GFRP) bars as shrinkage reinforcement for slabs-on-grade is examined experimentally and the results of this investigation are presented in this article. Steel frames were used to cast slabs reinforced with GFRP and steel, which significantly reduced the amount of deformation that could occur during shrinkage which eventually created a circumstance where shrinkage cracking could occur. Thus, it would be possible to assess the impact of various reinforcement strategies with more precision. The purpose of the investigation was to examine the performance of GFRP and steel reinforcing bars to control drying shrinkage cracking. Six slabs were cast inside structural steel frames that created the edge forms. Amongst those 6 slabs, three steel forms were positioned inside and cast indoors, and the other three slabs were cast according to

the outdoor conditions. The dimensions of the slab were 3 meters long, 1 meter breath, 0.15-meter height i.e., (10 ft x 3.3 ft x 6 in). Each form was end-connected to 0.75 m (2.5 ft) threaded rods that were inserted into the slab to serve as end restraints. A plastic covering was applied to the underside and lateral sides of the form to diminish friction along the whole slab. the slabs were reinforced with GFRP and steel rebar as per its requirements, these temperature and shrinkage rebars were positioned at one-third height of the slab and supported with the help of serpentine bolsters. For both the indoor and outdoor conditions one slab was reinforced with No.4 (12 mm) steel rebars distributed at 450 mm center-to-center spacing, and one was cast utilizing the No.3 (9.5 mm) GFRP rebars which was distributed at a spacing of 450 mm, and the last slab was supported with No. 4 (12.7 mm) GFRP rebar having a spacing of same 450 mm. An M20 grade of concrete was manufactured to cast all 6 slabs. The concrete was poured and spread evenly using screeding tool, it was then consolidated using a vibrator to optimize the concrete mix without any air voids and honeycomb. To develop a suitable circumstance curing was avoided on the slab's surface; alternatively, the bleed water was utilized to keep the top surface moist in the initial days. Due to the change in Atmospheric conditions, the rapid alternation happening in the temperature and humidity of both the indoor and outdoor conditions were inspected and recorded throughout the test. the average indoor temperature was 18°C (64°F), with a small overall daily variation of $\pm 6^{\circ}\text{C}$ (11°F), while the average outdoor temperature was 17°C (63°F), with an overall daily variation of $\pm 15^{\circ}\text{C}$ (27°F). Both the indoor and outdoor slabs were exposed to atmospheric conditions through the test. The average relative humidity for the indoor slabs was 37% (ranging from 16 to 58%), whereas for the outdoor slabs it was 70% (ranging from 18 to 96%). (Barragan et al., 2023)

To obtain the compressive strength of the concrete cube 150 mm and 75 x 75 x 250 mm size prism were constructed along with respective slab mix. Every specimen was maintained in the identical circumstances as the slabs, except for the indoor compressive strength cubes. The moist room was used to store the indoor cubes. Concrete compressive strength was measured according to EN 12390. Free shrinkage of concrete was measured according to EN 12390-16. Based on these test reports the average compressive strength of concrete on the 28th day was 31 and 35 MPa (4500 and 5130 psi) for the indoor and outdoor specimens, respectively. The compressive strength and the shrinkage cracks macrostrain were plotted against time and shown in Figure 2.18.

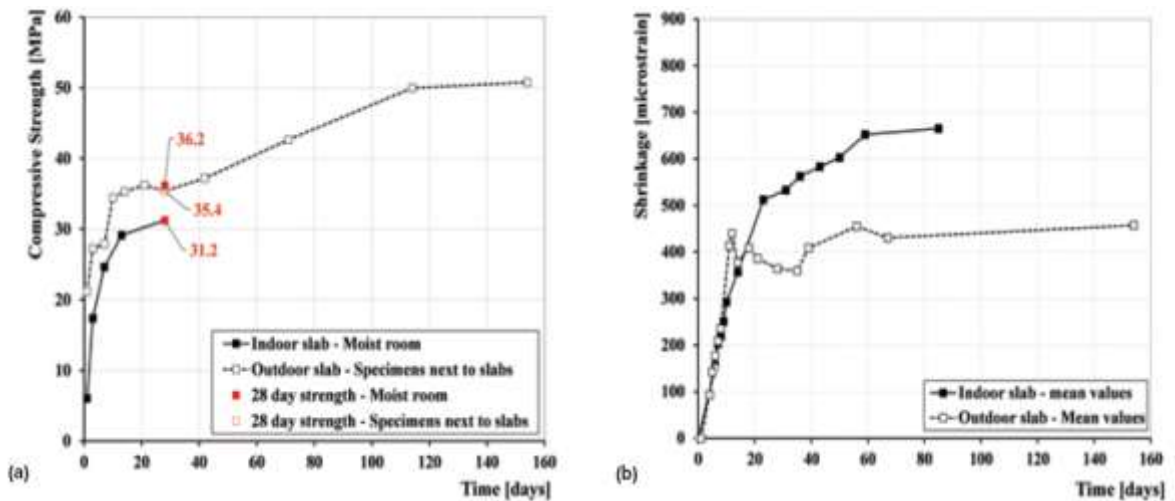


Figure 2.18: Test Results of Indoor and Outdoor Slab (A) Compressive Strength (B) Shrinkage (Barragan et al., 2023)

Approximately 3 months of free shrinkage development were examined for indoor slabs, and it was investigated throughout the test duration for outdoor specimens. Indoor specimens exhibited quick shrinkage over the initial 20 days after casting, followed by a slowing trend until attaining an almost asymptotic behavior at around 60 days. The average shrinkage at 90 days was 665 microstrains, which is appropriate for that concrete class. Post-casting, the outdoor specimens shrank at a high rate for the initial 20 days, then

gradually declined until they reached an almost asymptotic behavior at around 48 days. The average overall shrinkage at 154 days was 457 microstrains.

From Figure 2.19, it is clear that the microcrack patterns were observed in the middle portion of all indoor slabs, where larger stresses were generated. Slabs reinforced with GFRP showed crack openings that were significantly less than 0.1 mm (0.004 in.). The steel-reinforced slabs showed similar behavior up till a macrocrack emerged at 126 days, with an aperture of over 0.65 mm (0.025 in.) after 209 days.

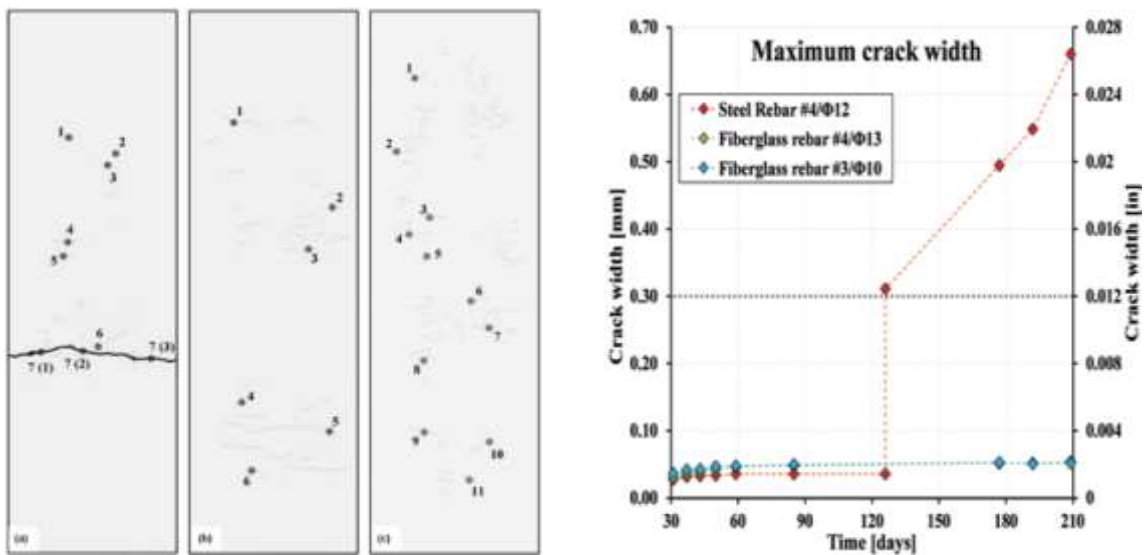


Figure 2.19: Indoor Slab Crack Pattern (A) No.4 Steel Rebar (B) No.4 GFRP Rebar (C) No.3 GFRP Rebar Slab (Barragan et al., 2023)

The slab with No. 3 GFRP bars had more microcracks, which were not apparent to the naked eye. Slabs reinforced with No. 4 GFRP bars exhibited more microcracks than the ones reinforced with No. 4 steel bars. A digital microscope (Dino-Lite AM4113T) using a 200X magnification was utilized to measure the generated crack width and length accurately. To monitor their development over 210 days, precise measuring locations were established along the cracks. Generally, cracks below 0.3 mm in width were negligible and acceptable for a slab on grade concrete. It can be observed from Figure 2.20 that in contrast

to the slab reinforced with No. 3 GFRP bars, which had no evidence of any microcracks, the one strengthened with No. 4 steel bars contained a greater number of these microscopic fractures.

Slabs enforced with No. 4 steel and No. 4 GFRP bars both exhibited surface microcracks, but the steel-reinforced slab displayed additional cracks overall. Observation performed over 210 days proved that the outdoor slabs did not generate any macro-size cracks. Slabs reinforced with No. 4 GFRP bars and No. 4 steel bars display a comparable crack width pattern, however the steel-reinforced slab shows wider cracks.

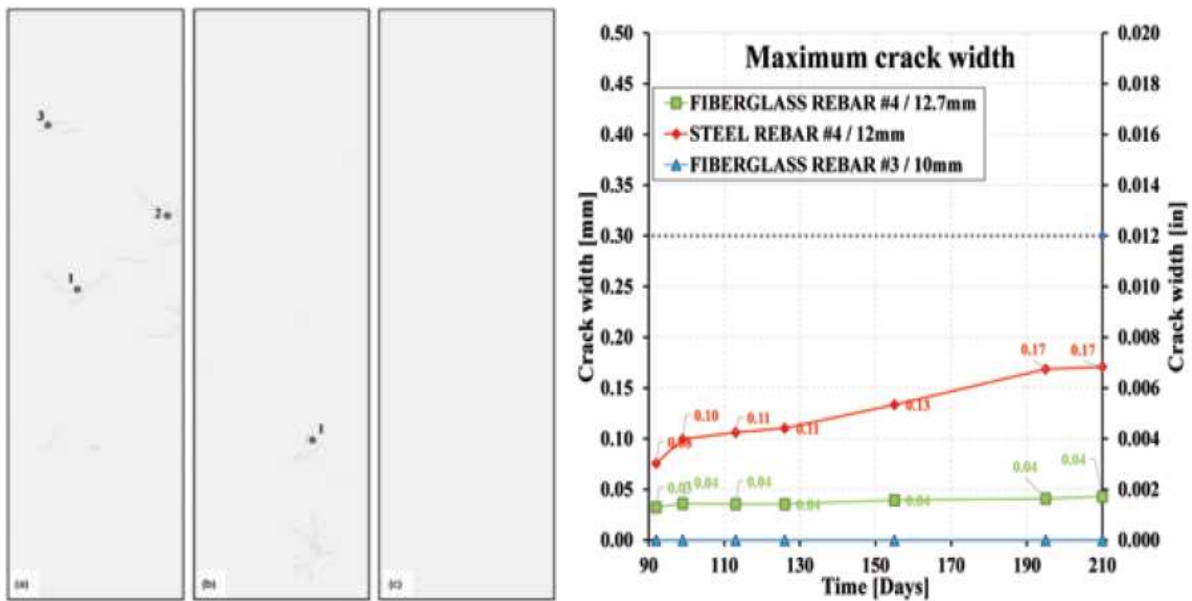


Figure 2.20: Outdoor Slab Crack Pattern (A) No.4 Steel Rebar (B) No.4 GFRP Rebar (C) No.3 GFRP Rebar Slab (Barragan et al., 2023)

All three slabs show fracture widths less than the "visible crack opening" of 0.3 mm. Overall, Slabs reinforced with GFRP bars had little to no cracking, whereas slabs reinforced with steel rebars experienced a greater degree of cracking. In the initial phases of microcracking, when only a small displacement (crack opening) is required to activate an effective bond strength, the GFRP bar's chemical compatibility and unique surface

properties could facilitate the development of an extremely efficient bond strength to subsidize it. Reinforced concrete elements that were embedded with GFRP reinforcement resist shrinkage, as the concrete compresses the reinforcement and rebars generate an equal and opposite tensile stress on the concrete to prevent it.

➤ **Experimental study on flexural behavior of GFRP reinforced concrete slabs.**

To mitigate corrosion in concrete structures such as bridge decks, water treatment facilities, marine engineering, slab-on-grade for industrial structures, and chemical plants, GFRP rebar is increasingly being employed as an improvement material instead of a conventional steel bar. GFRP rebars were a cost-effective alternative to steel rebars because of their unique performance such as high tensile strength, thermal insulation, feasible cutting, and non-corrosive properties.(Li-Xiang et al., 2021) Using a combination of experimental testing and theoretical calculation methods, this study investigated the load-bearing capability of two sets of GFRP-reinforced concrete slabs that varied in strength grades and reinforcement ratios. The experimental data was used to validate the proposed formula for the flexural capacity of GFRP-reinforced concrete slabs. The impact of GFRP bars on concrete slab flexural characteristics remains unclear despite its importance in engineering structural design. This research analyzes the impact of reinforcement ratio and structural strength on crack width, deflection, and flexural behavior in GFRP-reinforced concrete slabs, using experimental data from 8 one-way slabs. Based on the mechanical characteristics of a one-way slab, a rectangular section is selected as the test specimen. In total, eight concrete beams were constructed for this experiment by adding various kinds of GFRP bars as reinforcement. The dimensions of the rectangular slab section were 2400

mm long, 1000mm wide, and 150 mm width was considered for this experimental test. The properties of each concrete slab and the number of GFRP rebars used were all mentioned in Table 2.10. This study conducted an experimental test on two groups of slabs with different grades of concrete and GFRP rebar size. Group one has 4 slabs which were cast with M30 grade concrete, the GFRP rebar size varies as 6 mm, 8 mm, 10 mm, and 12 mm. Group two slabs were cast with M40 grade and the same 4 GFRP rebars as mentioned in the Table 2.10 below.

Table 2.10: Specimen Type Reinforcement Condition(Li-Xiang et al., 2021)

Group	Specimen	concrete		reinforcement					
		Grade	strength (MPa)	Bars	ρ (%)	ρ_{fb} (%)	ρ / ρ_{fb}	Ultimate strength (MPa)	Modulus of elasticity (GPa)
I	GFI-1	C30	36.8	6 ϕ 12	0.45	0.52	0.87	828.3	42.3
	GFI-2	C30	35.9	8 ϕ 12	0.60	0.52	1.15	828.3	42.3
	GFI-3	C30	37.2	10 ϕ 12	0.75	0.52	1.44	828.3	42.3
	GFI-4	C30	37.5	12 ϕ 12	0.90	0.52	1.73	828.3	42.3
II	GFI-1	C40	46.3	6 ϕ 12	0.45	0.52	0.87	828.3	42.3
	GFI-2	C40	45.8	8 ϕ 12	0.60	0.52	1.15	828.3	42.3
	GFI-3	C40	46.2	10 ϕ 12	0.75	0.52	1.44	828.3	42.3
	GFI-4	C40	45.0	12 ϕ 12	0.90	0.52	1.73	828.3	42.3

ρ = area of reinforcement/bh₀; ρ_{fb} = balanced reinforcement ratio.

The three-point loading method is utilized to load the response frame using a 30-ton hydraulic jack equipped with a digital display device. Before a crack, the loading pace is 5 kN per level; with a crack, the loading speed is lowered to 3 kN per level. To measure the strain, a DASP strain meter is installed. The deflection of the slab and the dispersion of the fracture were measured after every phase of loading. To acquire the deflection of the investigated slabs, thirteen transducers were installed, two at each cross-section of one-third of the span, one at mid-span, and two at each cross-section of the supports. Furthermore, all the slabs were equipped with 4 steel strain gauges at the middle of the GFRP rebar, and 8 concrete strain gauges were installed in the positions as mentioned in Figure 2.21.

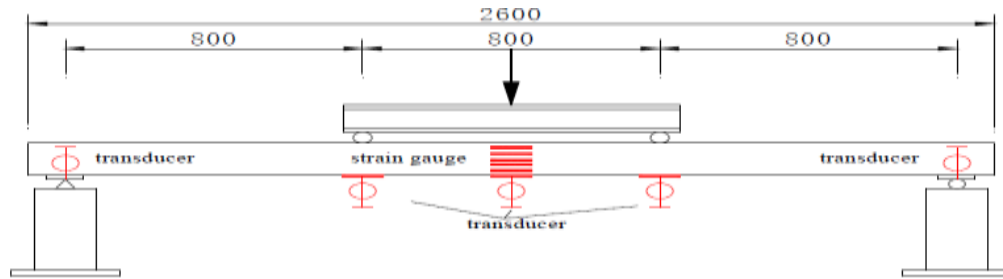


Figure 2.21: Test Setup and Sensor Distribution (Li-Xiang et al., 2021)

Based on the experimental test results, the flexural behavior of conventional and GFRP-reinforced concrete beams demonstrates similar patterns. The initial crack induced by the bending moment emerges near the mid-span and is perpendicular to tensile stress, referred to as the bending crack. As the load increases, the crack develops vertically. Additional bending cracks emerge in the pure bending portion, while diagonal fractures emerge in the shear-bending region between the beam support and the loading point in the bottom surface.

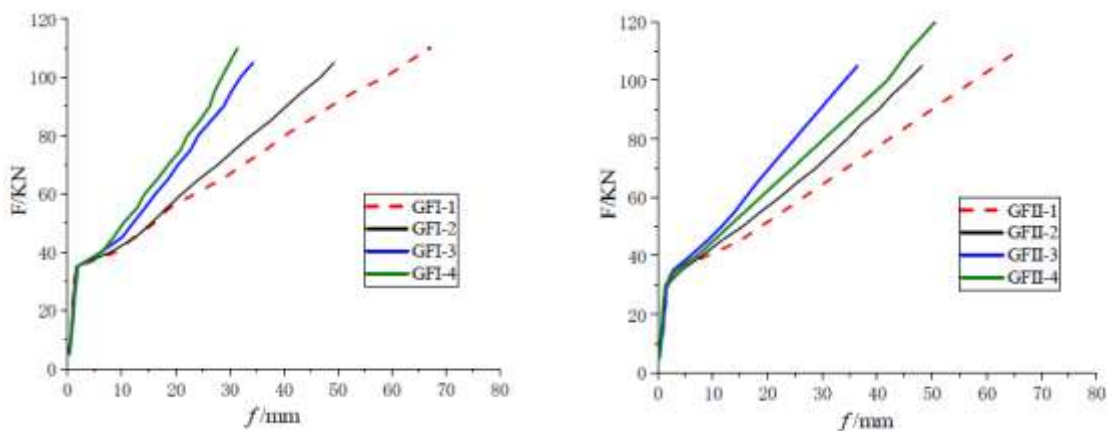


Figure 2.22: Load VS Deflection Curve (Li-Xiang et al., 2021)

In Figure 2.22, Both graphs show that load-deflection curves were almost bilinear, with a change of curve detected when cracks evolve. There were two distinct phases to the curves that were defined by their varying Load vs deflection curves. Stage one is the initial loading phase where there is minimal deformation and strain exerted in the tension and

compression zones are within the limits. The slab maintains its elasticity and the concrete coincides with the GFRP rebars to withstand the stress exerted on it. Once the first crack appears the slab swifts to the flexural stage, which pushes the concrete to its ultimate strength, and the crack develops on the weakest position of the bending location. Once the propagation of cracks starts, it enforced the deflection rises abruptly. Each slab has varying strengths and reinforcing ratios, but the typical crack spacing for pure bending is in the range of 100 to 110 mm, influenced by the bond between GFRP bars and concrete and the thickness of the concrete cover. The maximum crack width obtained was 3.26 mm on the slab GFII-2, each slab had experienced around 7 to 8 cracks before complete failure. The crack widths ranged between 1.4 mm to 3.5 mm which varies regarding the slab type.

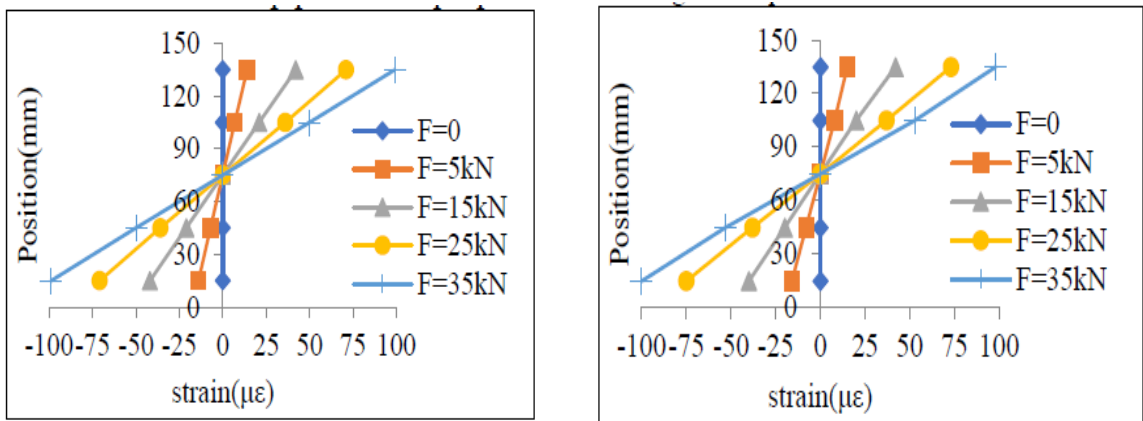


Figure 2.23: Midspan Strain Curve Of GFI-3 and GFII-3 Slab (Li-Xiang et al., 2021)

The midspan strain curve of GFI-3 and GFII-3 slabs is shown in Figure 2.23, this strain curve is exposed till the first crack happens. The strain is very minimal before concrete cracking. Concrete's strain distribution follows the plane section assumption, and the stress-strain connection exhibits proportional behavior in the elastic stage. Once the crack is imposed on the concrete surface the strain value deviates indicating the crack. Except for GFI-4 and GFII-4 concrete slab types, all the other 6 slab types were subjected to a

tensile failure and those two slab types experienced a compression failure. The load-bearing capacity of each slab is calculated with the help of theoretical formulas and compared with the experimental results. the flexural bearing capacity coefficient is from 1.02 to 1.36. Group I's flexural bearing capacity coefficient is enhanced from 1.10 to 1.39, while Group II's increases from 1.02 to 1.26. As the flexural load-carrying capacity coefficient improved gradually, correspondingly improved the flexural bearing capacity. As a result, the safety factor is raised. ACI code and domestic research on GFRP beams indicate that $\rho = 1$ which generates compression failure of members. Tests on concrete slabs with GFRP bars indicate that tensile failure may occur with reinforcement ratios slightly above 1.4. Choose a high reinforcing ratio during design to ensure concrete beam compressive capability. As GFRP bars have a low elastic modulus, the impact of reinforcement ratio on crack strength is negligible, thus it can be ignored for crack resistance in the same strength grade. When the reinforcement ratio is 1.0-1.4 times the equilibrium ratio, cracking and concrete brittle failure can lead to both tensile and compressive failure. Therefore, $\rho_f > 1.4\rho_{fb}$ is recommended to provide a durable design of the GFRP-reinforced concrete slab. (Li-Xiang et al., 2021)

➤ **Punching shear capacity of GFRP bar-reinforced concrete slabs-on-ground**

(Al-Zahrani, M.M et al., 2023) This study examined slabs-on-ground reinforced with GFRP bars under focused loads to evaluate punching shear capacity. Along with loads, reinforced concrete slabs like pavements and slabs-on-ground were exposed to intense seasonal climate variations like freeze-thaw cycles, large temperature fluctuations, and rainfall. Concrete can easily get cracked under these conditions, allowing water and de-icing chemicals like chlorides to seep into the embedded rebars causing corrosion, and

deterioration of concrete. In pavements, sidewalks, industrial floors, bridges, and retrofit works, glass fiber-reinforced polymer (GFRP) bars have been used as a replacement for steel rebars due to their corrosion resistance, lightweight, high tensile strength, and electrical and magnetic transparency. In this study, twelve $1.5 \times 1.5 \times 0.15$ m³ slabs were constructed with a single layer of reinforcing grid, which is superimposed on top of a 100 mm thick extruded polystyrene foam sheet. The study included the two kinds of GFRP bars (RB-ribbed GFRP, SC - sand-coated GFRP) and conventional steel as parameters, with bar spacing of 200 mm and 300 mm, different positioning of the reinforcement grid in the slab at the top-third, middle-depth, and bottom-third of the depth, concentration of load positioned at the center, edge, and corner, and two test loading type which is monotonic and repeated. The slabs were positioned on an extruded polystyrene base, and subjected to laboratory tests on a concrete floor that duplicates the subgrade and offers a modulus of subgrade reaction similar to that of a compacted sand subbase.

Maintaining a consistent subgrade modulus for the slabs was crucial for this study's parameters. The ideal substitute for compacted soil subgrade was determined after extensive testing on several polystyrene foams, including EPS and XPS grades. The research involved examining the modulus of subgrade reaction by subjecting $600 \times 600 \times 100$ mm³ foam specimens to punching shear pressures using a 200×200 mm² steel plate. Tests were conducted on the reaction frame. Position a 100 mm thick XPS panel on the reaction floor beneath the frame, and the GFRP slab specimen was positioned on the XPS base. The equipment used to measure slab reaction consists of 16 LVDTs, strain gauges, and a load cell. The top surface of the specimens was monitored for vertical displacements at 16 places using LVDTs. A hydraulic jack was utilized to apply the load,

along with a steel column made of two steel tubes with an axial load capability of 1000 kN. A 200 mm-wide, 25 mm-thick square steel plate was employed to distribute the stress to the slabs. (Al-Zahrani et al., 2023) One slab specimen (SC-200-REP) underwent testing under repetitive loading, while the other 11 slabs were examined under monotonic loading.

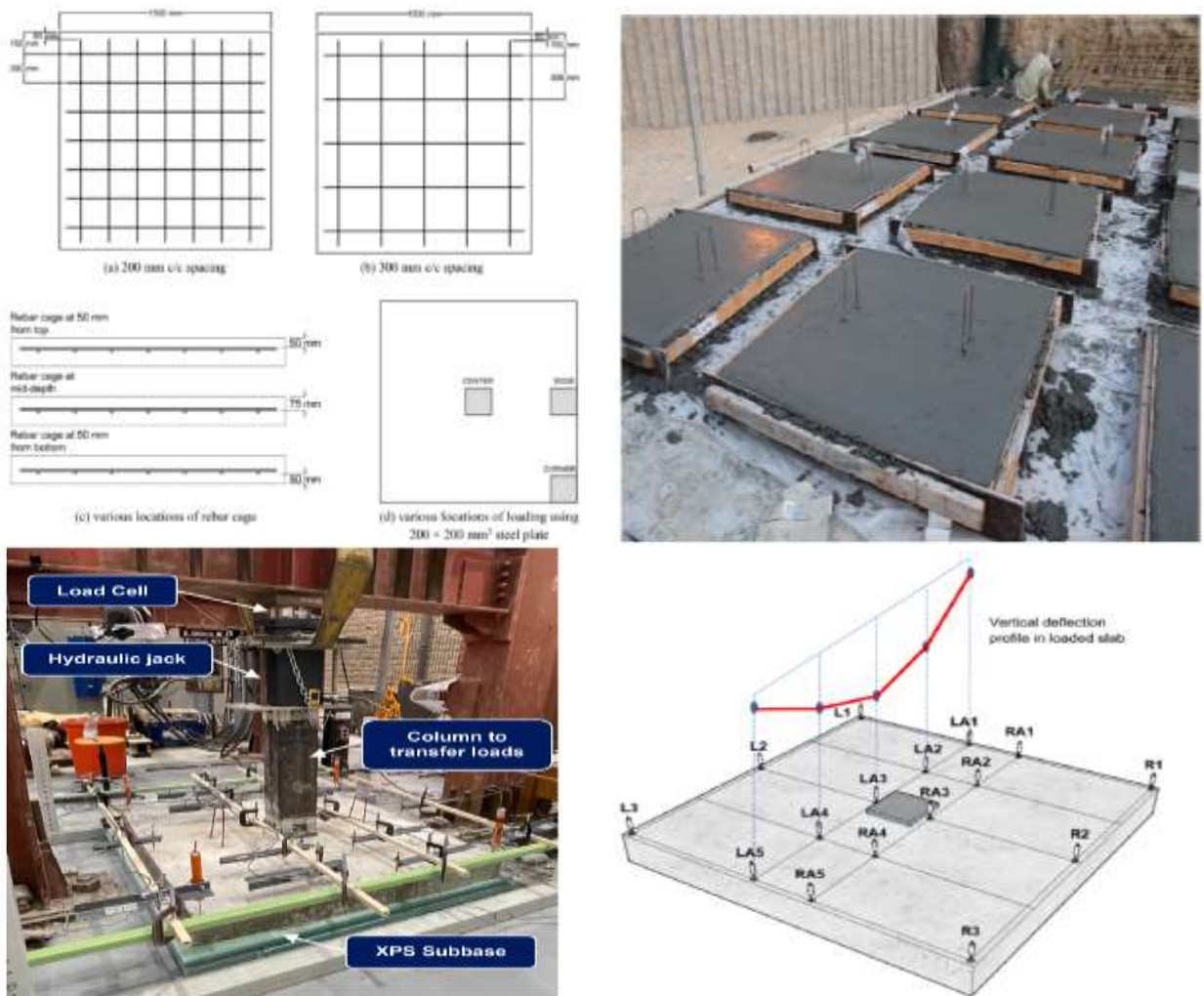
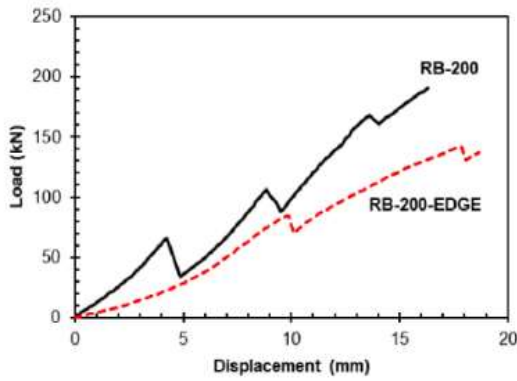
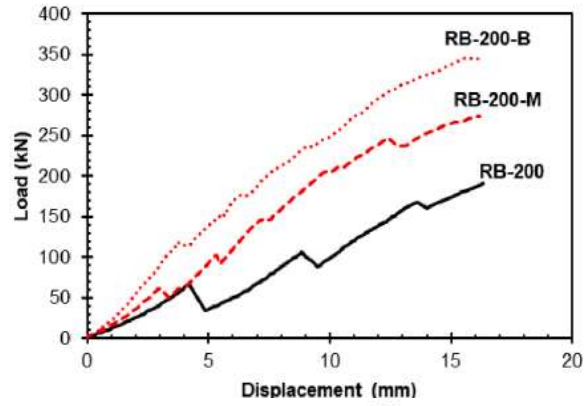


Figure 2.24: Schematics of GFRP Slab Specimen (Al-Zahrani et al., 2023)

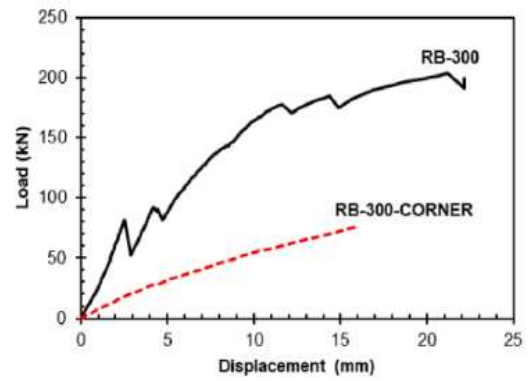
A monotonic loading rate of about 2 mm/min was used. The one-way repeated loading scheme, adapted from ACI 437. Increase load levels per two loading cycles. In each increment, load levels were administered twice for 1 and 3-minute periods before increasing the peak for the next cycle. An initial load equal to 10% of the estimated failure

load (250 kN) and subsequent increments of 25 kN were chosen for the SC-200 specimen. When loading exceeded 225 kN, the load was applied monotonic till failure. All center-loaded specimens exhibited comparable crack propagation, including a punched cone at the loading site and several radial cracks on the bottom surface. The plain concrete slab, (PL), is split into four parts due to lack of reinforcement. Despite variations in specimen specifications, the average punching cone diameter in centrally loaded reinforced slabs ranged from 887 mm to 1039 mm. The RB-200, SC-200, and ST-200 had 11, 10, and 9 radial cracks, whereas the RB-300, SC-300, and ST-300 had 6, 6, and 7 cracks, respectively.(Al-Zahrani et al., 2023) This shows that Closer bar spacing of 200 mm effectively distributed concrete damage when compared to slabs with 300 mm spacing. By lowering the rebar cage in RB-200 from the top-third to the mid-depth of the slab, the number of cracks dropped from 11 to 10, showing identical failure modes in both designs. RB-200-B specimen with rebar grid at the bottom-third of slab depth had 18 radial cracks, while RB-200-M specimen had only 11 to 10 cracks. In RB-200-EDGE, three radial cracks originated at the loading point and the failure cone had a diameter of 910 mm. When RB-300-CORNER was loaded at the corner, the ultimate failure mode was brittle, not influenced by cracking load.

The laboratory findings demonstrate that the 200 mm-thick slabs-on-grade reinforced with GFRP bars provide sufficient strength, stiffness, and punching shear capacity to withstand concentrated loads from vehicles with wheel loads of 35.6 kN (H10 AASHTO truck load), as well as thermal loading and shrinkage. Slabs reinforced with SC-200 had a cracking load that was 38.0% higher than that of RB-200 and 58.0% higher than that of RB-300, respectively.



(a) Load-displacement plot: edge loading



(b) Load-displacement plot: corner loading



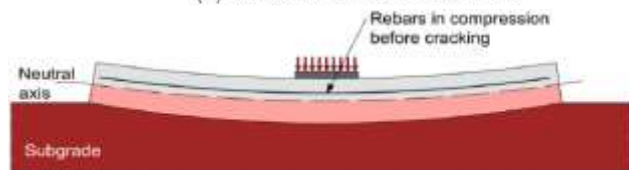
(c) failure in RB-200-EDGE



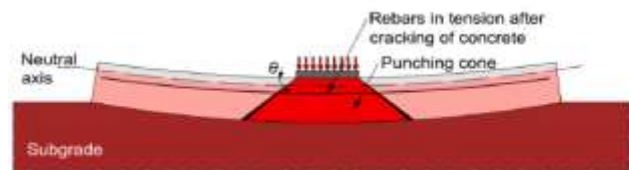
(d) failure in RB-300-CORNER



(h) RB-200-M



(a) compression in rebars before concrete cracking



(b) tension in rebars after concrete cracking

Figure 2.25: GFRP Slab-On-Grade Test Results (Al-Zahrani et al., 2023)

In the steel-reinforced specimen, the cracking loads were 73.5 kN, greater than RB-200 but less than SC-200. When tested at 300 mm spacing, ST-300 had the lowest cracking load compared to RB-300 and SC-300. While RB-300 and SC-300 had lower punching shear loads, the ST-300 exhibited significantly higher loads. In comparison to steel bars, GFRP bars possess ultimate load capabilities that were, on average, around 21.0% lower.

For 200 mm spacing, the deflection at failure is approximately 14.0% more. (Al-Zahrani et al., 2023) Compared to the ribbed bar (RB), the sand-coated GFRP bar (SC) had marginally higher flexural strength, stiffness, and punching shear capacity. Slab spacing reduction led to a higher composite reaction from rebars, which in turn increased capacity and stiffness. Under corner loading, the load-carrying capacity of the GFRP-reinforced specimen diminished by 47.0%, and at edge loading, it was reduced by 9.0%. The ultimate load capacity was found to be significantly increased when the rebar grid was positioned at the top, mid-depth, and bottom of the slab. Punching shear capacity at mid-depth improved by 9.0% and at the bottom by 39% in the RB-200 slab when the reinforcing grid was transferred to the bottom from the top.

➤ **Punching-Shear Strength of Normal and High-Strength Two-Way Concrete Slabs Reinforced with GFRP Bars**

(Hassan et al., 2013) This study examined the punching-shear behavior of two-way concrete slabs using varying grades of glass fiber-reinforced polymer (GFRP) bars. Using CSA S807 CSA 2012 as a reference, this review details the punching-shear behavior of inner slab-column connections reinforced with Grades I, II, and III GFRP bars and built with NSC and HSC concrete, respectively. Two concrete types - normal strength concrete (NSC) and high strength concrete (HSC) with an entrained-air ratio of 5–8% were used to

cast the slab-column connectors. The desired compressive strength for NSC was 35 MPa, while for HSC, it was set at 65 MPa. Ten complete slab-column connections strengthened with GFRP bars of varying grades [CSA S807 2010: Grades I, II, and III], conventional steel rebars were used and subjected to monotonic concentric loading until failure. The slab's dimensions were 2,500 x 2,500 mm with a depth of 200 and 350 mm and a 300 × 300 mm square column stub positioned in the middle of the slab. The column stub projected 300 mm outside the slabs' top and bottom surfaces. Two series were formed based on the specimens. Series I (200 mm thick) possessed four GFRP-RC specimens (0.71-1.56% reinforcement ratio) and a steel-reinforced control specimen. The control steel-RC slab and four GFRP-RC specimens with a ratio of reinforcement (ρ) ranging from 0.34 to 1.61 percent constituted Series II, which had a thickness of 350 mm. Furthermore, Grade-III GFRP bars ($G_{(1,2)} 30/20$) were utilized to reinforce one slab in Series I.

Each specimen was subjected to a monotonic focused load from the bottom, imposing the load on the column stud of the slabs up till failure. The specimens were merely propped up on every side and pressed against the hard floor of the laboratory utilizing a 100 mm wide metallic structure that was held in place by eight 38 mm diameter steel tie rods. Depending on the predicted capacity of each specimen, a couple of 1,500 kN hydraulic jacks were used to apply the load at a rate of 5 kN/min. Installation of two hydraulic jacks necessitated their connection to a single pump and generated a mutual calibration for sequential operation. Furthermore, before testing, the bottom surface (compression side) of the slab was covered with eight electrical-resistance strain gauges at (C1 to C8) positions.

Besides, electrical strain gauges were employed in the steel tie rods that supported the specimen to ensure that the force was symmetrical throughout the test. Eleven linear

voltage differential transformers (LVDTs) recorded the specimens' deflection at various points. The development of cracks was marked, and loads were obtained throughout the test.

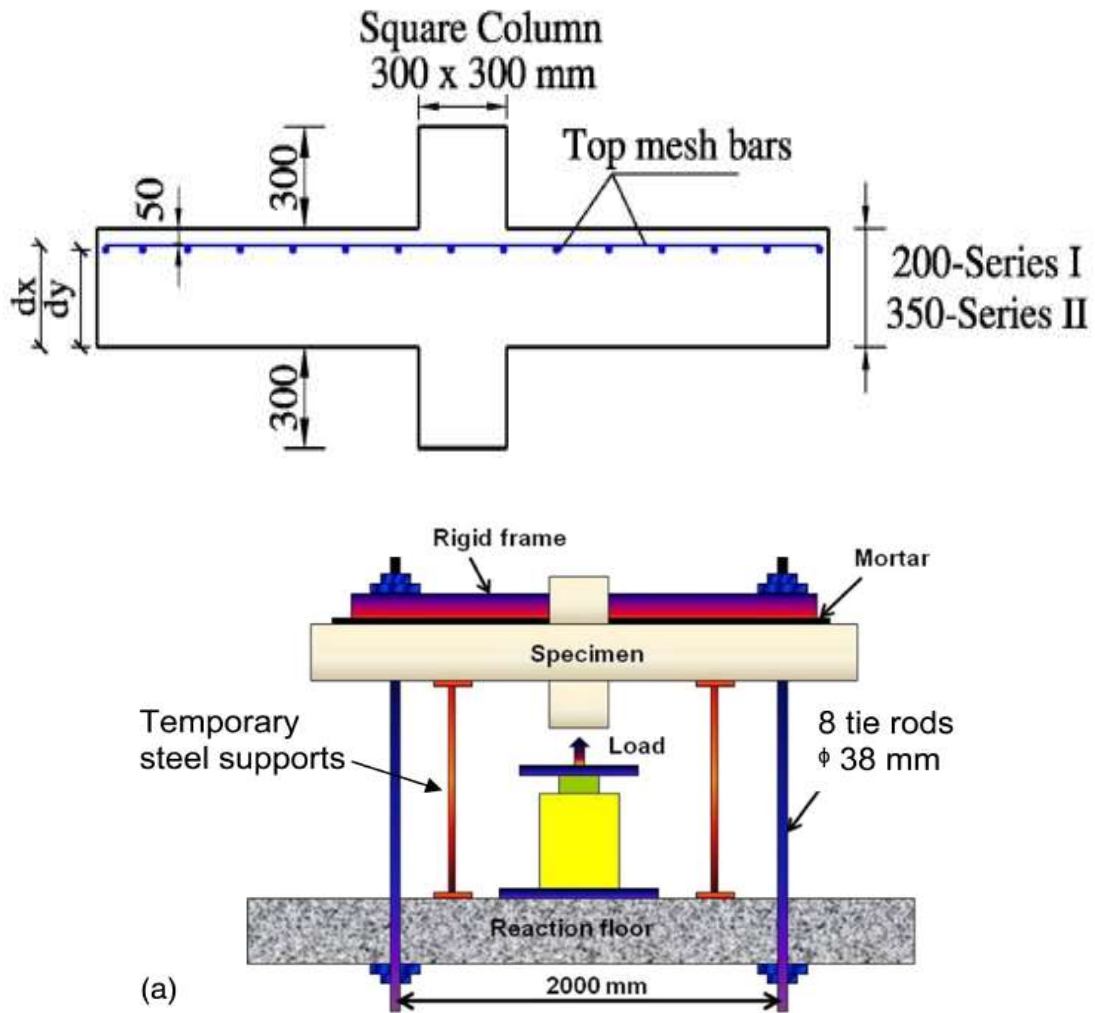


Figure 2.26: GFRP Slab Geometry and Test Setup (Hassan et al., 2013)

Correlations between load and deflection for specimens subjected to testing were determined by LVDTs positioned 40 mm away from the column face. Every single slab exhibited the usual bilinear load-deflection pattern. Both the initial (k_i) and post-cracking (k_p) stiffnesses of the specimens were shown on the load-deflection curve in Figure 2.27. When it comes to FRP RC slabs, most empirical punching-shear strength equations were

altered from the original steel ones, having the lower modulus of elasticity as the main mechanical property that needs to be adjusted. The punching-shear capacity of eight GFRP-reinforced specimens is compared with the predictions generated by the various punching-shear equations in CSA S806 (CSA 2012), ACI 440 (ACI 2006), BS 8110 (BSI 1997), and JSCE (1997). (Hassan et al., 2013). The accuracy of these equations is assessed Against the experimental results.

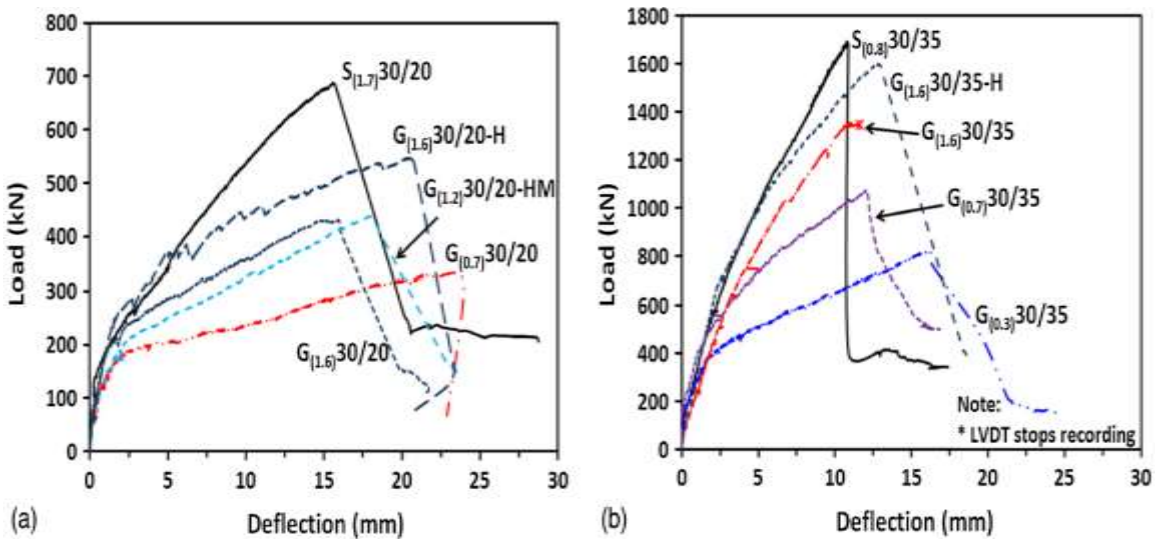


Figure 2.27: Load Vs Deflection Curve (Hassan et al., 2013)

The punching-shear equations were all configured with safety factors of 1.0. Specimens subjected to testing demonstrated that punching-shear failure constituted the ultimate mode of failure, without flexural compression of the concrete or reinforcement bar rupture or slippage. Punching-shear stresses at failure were improved by 35% and 81%, respectively, by elevating the reinforcement ratio from 0.71% to 1.56% for Series I and from 0.34% to 1.62% for Series II. Therefore, Enhancing the GFRP reinforcement ratio contributed to improved punching-shear capacities, diminished reinforcement strains, and minimized slab deflections. The punching shear capability of the GFRP-reinforced specimens was enhanced by utilizing HSC. $G_{(1.6)} 30/20$ -H and $G_{(1.6)} 30/35$ -H experienced an increase

of 27% and 7% in ultimate punching-shear capacity against other specimens. Relationships between load versus deflection were improved by using HSC in specimens $G_{(1.6)} 30/20\text{-H}$ and $G_{(1.6)} 30/35\text{-H}$. Under the same stress level, the two samples showed reduced deflections than the alternative GFRP-reinforced with NSC ones. Furthermore, until approximately 60% of the ultimate capacity, they exhibited identical load-deflection relationships to their steel-reinforced slab. It produced accurate estimates for two specimens with concrete strength of 75.8 MPa, even though the CSA S806 (2012) punching-shear section limits concrete strengths to 60 MPa. Their respective $V_{\text{test}}/V_{\text{pred}}$ ratios were 1.06 and 1.07. (Hassan et al., 2013) The uncracked initial stiffness of the GFRP-reinforced specimens was significantly influenced by the concrete compressive strength. $G_{(1.6)} 30/20\text{-H}$ and $G_{(1.6)} 30/35\text{-H}$ specimens experienced an uplift of 22% and 51% compared with their counterparts $G_{(1.6)} 30/20$ and $G_{(1.6)} 30/35$. On the contrary, the post-cracking stiffness was equivalent to that of the NSC-imposed GFRP specimens (Hassan et al., 2013).

2.6 Validation of Field Data with Plaxis FEM Analysis

In geoenvironmental projects which utilize the Finite Element Method (FEM), it is critical to set soil model parameters as intended. To assist geotechnical engineers in this task, empirical equations have been developed to determine the model parameters for the Plaxis Hardening Soil model with small-strain stiffness (HS_{small}), according to specific soil characteristics such as relative density for sands and plasticity index for clays. This paper presents a validation of these equations for sands, using existing soil testing data. The main objective of these empirical equations is to provide an optimal initial approximation of soil behavior in FEM simulations over a variety of sands. A case study illustrates that these

equations produce an adequate preliminary approximation for deformations and stress distribution in actual engineering projects (Brinkgreve et al., 2010). Over the last two decades, the Finite Element Method (FEM) has gained prominence in geoenvironmental and design. It employs constitutive models to simulate soil behavior, with parameters that quantify certain soil characteristics. This paper shows all the proposed empirical formulae based on relative density for calculating all Plaxis HSsmall model parameters from limited geotechnical data. The intent is to promote the use of advanced soil models in engineering, especially during early project stages with minimal site-specific soil information.

**Table 2.11: Empirical equation to correlate HSsmall model parameter to RD
(Brinkgreve et al., 2010)**

Model Parameter	Empirical Formula	Unit
γ_{unsat}	$15 + 4.0 RD / 100$	kN/m ³
γ_{sat}	$19 + 1.6 RD / 100$	kN/m ³
E_{50}^{ref}	$(60000 * RD) / 100$	kN/m ²
E_{oed}^{ref}	$(60000 * RD) / 100$	kN/m ²
E_{ur}^{ref}	$(180000 * RD) / 100$	kN/m ²
M	$(0.7 - RD) / 100$	-
G_0^{ref}	$(60000 + 68000 * RD) / 100$	kN/m ²
$\gamma_{0.7}$	$(2 - RD / 100) * 10^{-4}$	-
φ (<i>phi</i>)	$(28 + 12.5 RD) / 100$	°
Ψ (<i>psi</i>)	$(- 2 + 12.5 RD) / 100$	°
R_f	$(1 - RD) / 800$	-

The empirical equations concerning the relative density to correlate HSsmall model parameters in Plaxis FEA software are shown in Table 2.11. These formulas were specifically derived for the drained soil conditions. The soil parameters of the HSsmall strain model in the Plaxis FEA software for loose, medium, dense, and very dense states of subgrade were calculated based on these empirical formulae and shown in Table 2.12.

Table 2.12: HSsmall strain Model Parameters for Sand (Brinkgreve et al., 2010)

<i>RD</i>	γ_{unsat}	γ_{sat}	E_{50}^{ref}	E_{oed}^{ref}	E_{ur}^{ref}	G_0^{ref}	<i>m</i>
-	kN/m ³		kN/m ²	kN/m ²	kN/m ²	kN/m ²	-
25	16.0	19.4	15000	15000	45000	77000	0.622
50	17.0	19.8	30000	30000	90000	94000	0.544
80	18.2	20.3	48000	48000	144000	114000	0.450
100	19.0	20.6	60000	60000	180000	128000	0.388

<i>RD</i>	$\gamma_{0.7}$	ϕ'_o	ψ_o	R_f
-	-	o	o	-
25	$1.8 \cdot 10^{-4}$	31.1	1.1	0.969
50	$1.5 \cdot 10^{-4}$	34.3	4.3	0.938
80	$1.2 \cdot 10^{-4}$	38.0	8.0	0.900
100	$1.0 \cdot 10^{-4}$	40.5	10.5	0.875

To verify the formulas for the stiffness parameters of HSsmall, a comparison was conducted between data obtained from actual drained triaxial tests on various sand types and the outcomes of numerical simulations using the HSsmall model. On evaluating the Plaxis FEA results with various field data for different sands at different densities with data from Jeffries & Been (2006). In most scenarios, the formulas tend to slightly overestimate stiffness under triaxial loading. Additionally, there is often a tendency to underestimate both strength and dilatancy. Realistically, high friction and dilatancy can diminish due to shearing and softening, which were aspects not incorporated into the HSsmall model. Consequently, a modest underestimate of peak strength may be appropriate. (Brinkgreve et al., 2010).

This paper also validates these empirical formulas by developing a Plaxis model against an excavation project in Berlin sand. The excavation reaches a depth of 16.8 meters, with a 32-meter-long wall. Anchors were installed in three rows above intermediate excavation levels at 4.8, 9.3, and 14.4 meters. The wall structure is simulated using Mindlin beam elements, and its interaction with the soil is represented by interface elements. Anchors were modeled using a mix of membrane elements for the grouted body and two-node spring elements for the anchor rods. The soil was identified as medium-dense Berlin sand, as determined from an undisturbed sample retrieved at a depth of 8 meters. The surface topsoil had a relative density (RD) of 50% for at least the upper 20 meters, while the next 20 meters were presumed denser with an RD of 80%, and the lower 60 meters were assumed to be very dense with an RD of 100% (Brinkgreve et al., 2010). In this case, the focus was on the unloading and small-strain stiffness parameters rather than loading stiffnesses. Interface strength was correlated with surrounding soil strength, reduced by a factor of 0.8 from benchmark values. Excavation mirrored practical site procedures. Figure 2.28 shows the results of this case study validation against the model developed using the empirical equation parameters.

The wall's calculated maximum displacement reaches 51 mm, exceeding corrected measurements by about 1.5 times. Although the overall deformation shape resembles the reference solution, with a noticeable 15 mm deviation. This discrepancy suggests potential shortcomings in soil stiffness, likely due to insufficient small-strain stiffness. Nevertheless, the distribution of bending moments closely matches the reference, with the maximum value almost identical at 735 kNm/m (Brinkgreve et al., 2010).

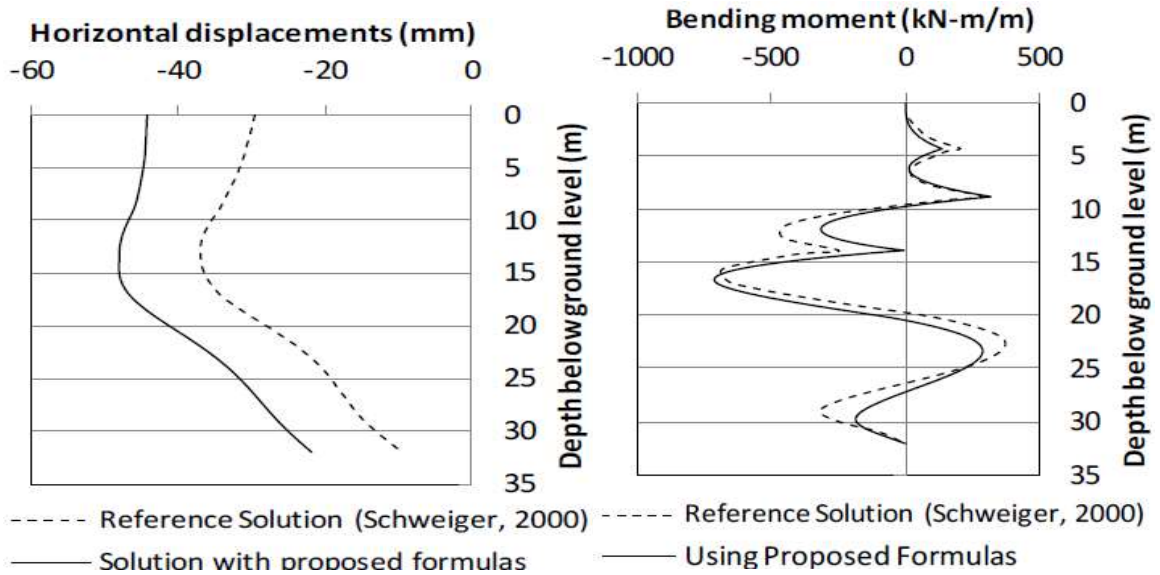


Figure 2.28: Comparison of Horizontal Displacement Profile and Bending Movement of the Wall with Triple Anchors (Brinkgreve et al., 2010)

While anchor forces generally align with expectations, the anchor forces were typically consistent with expectations, and post-installation changes imply decreased soil stiffness. Given the comprehensive soil data utilized for the reference solution, these findings provide a satisfactory preliminary assessment.

CHAPTER-3 SPECIMEN PREPARATION AND EXPERIMENTAL TEST SETUP METHODOLOGY

3.1 Introduction

The outline of this chapter is about laboratory experimental setup on soil structure interaction of “Tire derivative aggregate” (TDA) and GFRP reinforced concrete slab on grade tested under unreinforced and geocell reinforced sandy soil is illustrated in this section. The properties of all the materials utilized in this research were presented with a detailed description. The mix design, casting, and curing of the concrete specimens were explained. The soil preparation, compaction method, and soil test procedures were discussed. The Plate load test and monotonic load testing procedures are described precisely. This research focuses on the load vs settlement curve, stress vs strain curve, and the number of cracking points concerning the load at that moment (P_{cr}) were all reviewed in detail for all slab specimens to obtain the optimum TDA content and exalt the geocell reinforcement for weak soil structures.

3.2 Test Matrix

In this research, the slab-on-grade specimens were reinforced with TDA and GFRP rebars and examined by superimposing them on both unreinforced sandy soil and geocell-reinforced sandy soil. Three mix designs were considered for this investigation, first mix design was for the control specimen, second one incorporated $\frac{3}{4}$ inch size TDA as a partial 10% replacement based on the volume of the coarse aggregate. The third mix was designed for 20% volumetric replacement of coarse aggregate with $\frac{3}{4}$ inch size TDA. A total of seven slab-on-grade specimens were cast based on these three mix designs. One specimen was cast as a control specimen (CS) with a normal concrete mix design with steel rebars. Two

slab specimens were cast with the CS mix design but were reinforced with No.3 10 mm GFRP rebars as structural reinforcement. Two specimens were constructed utilizing the 10% TDA mix design and they were reinforced with No.3 10 mm GFRP rebars. The last couple of specimens were cast using the 20% TDA mix design and they were incorporated with No.3 10 mm GFRP rebars. The control specimen was specified with a specimen ID as CS. Slabs reinforced with glass fiber-reinforced polymer (GFRP) rebars were identified as GFRP – 1 and GFRP – 2. TDA-reinforced slab-on-grade is mentioned in terms of its replacement percentage, such as 10%-TDA – GFRP-1, 10%-TDA-GFRP-2, 20%-TDA-GFRP-1, and 20%-TDA-GFRP-2, where TDA implies tire derivative aggregate and, the number at the end indicates the batch number.

The Test matrix was created to examine the effectiveness of TDA in terms of percentage and GFRP reinforced slab-on-grade which is positioned and tested on top of both unreinforced and geocell-reinforced sandy soil subgrade, a comparison was done regarding its strength, stiffness, flexibility, load versus settlement curve, stress-strain curve, soil surface cracking load, soil surface crack pattern for both subgrade types, and cracking points of the concrete. The test matrix is summarized in Table 3.1. All the slab-on-grade specimens were exposed to a concentric point load imposed by a double-way hydraulic actuator (500 kN) and tested under a monotonic load test schedule. The bearing plate was 200 mm in diameter and 30 mm thick steel plate.

Table 3.1: Experimental Testing Schedule

Subgrade Type	Specimen Type	Testing Method
Unreinforced sandy silt soil	-	Plate Load Test
Geocell-reinforced sandy silt soil	-	Plate Load Test
Unreinforced sandy silt soil	CS, GFRP – 1, 10% TDA – GFRP – 1, 10% TDA – GFRP – 2, 20% TDA – GFRP – 1.	Monotonic load test (till failure)
Geocell-reinforced sandy silt soil	GFRP – 2, 20% TDA – GFRP – 2.	Monotonic load test (till failure)

Table 3.2: Slab-On-Grade and Subgrade Composition (Monotonic Load)

Specimen Type	Mix design	TDA and CA content	GFRP/Steel Rebar	Subgrade condition	Relative Density
CS	CS Mix design	100 % CA	No.3 10 mm steel	Unreinforced subgrade	68.03%
10 % TDA – GFRP – 1	10% TDA Mix design	10% TDA and 90 % CA	No.3 10 mm GFRP	Unreinforced subgrade	70.59%
GFRP – 1	CS Mix design	100 % CA	No.3 10 mm GFRP	Unreinforced subgrade	48.69%
10 % TDA – GFRP – 2	10% TDA Mix design	10% TDA and 90 % CA	No.3 10 mm GFRP	Unreinforced subgrade	49.82%
20 % TDA – GFRP – 1	20% TDA Mix design	20% TDA and 80 % CA	No.3 10 mm GFPR	Unreinforced subgrade	50.28%
GFRP – 2	CS Mix design	100 % CA	No.3 10 mm GFPR	Geocell-reinforced subgrade	50.36%
20 % TDA – GFRP – 2	20% TDA Mix design	20% TDA and 80 % CA	No.3 10 mm GFPR	Geocell-reinforced subgrade	50.11%

3.3 Material Properties of Components Used in This Research

3.3.1 Tire Derivative Aggregates (TDA)

The Tire derivative aggregates were originally derived from the scrap tires through recycling. A tire is a combination of rubber elastomer sheets solidified with transversely running steel fibers, and nylon threads. Rubber tires, when formed into rubberized materials, exhibit excellent tensile and shear strength with exceptional fatigue resistance. Rubber has great adherence to metallic wiring and minimal hysteresis, which contributes to its long-term integrity. Since 1996 Divert Nova Scotia (Divert NS) has been processing and recycling scrap tires throughout Nova Scotia. The organization reports that over one million used tires were eliminated from the province's landfills, with 70% going to Halifax construction and demolition Recycling to be processed into a tire-derived aggregate (TDA) for engineering purposes. The TDA was obtained from a recycling company “WEIBOLD Tire Recycling Ltd”. However, the Shredded tires will be in different sizes and will contain a lot of dirt and waste-rusted steel in it. All the rusted steel and dirt were segregated from TDA and disposed away. To consolidate the TDA according to the required size of $\frac{3}{4}$ inch, all the segregated TDA particles were processed through sieve analysis to obtain the necessary amount of TDA. As TDA is composed of various irregular dimensions several large aggregates would pass through the $\frac{3}{4}$ -inch sieve, hence all the larger particles were hand-cut to the required size and dimensions. As the tire shredded dimensions grew, hydraulic conductivity elevated from 0.2 to 0.85 cm/s. The friction angle varied between (15-32°) and the cohesiveness range (349-394 N/m²) was observed. As the particle size of TDA escalated from 50 to 300 mm, the scrap tire's shear strength enhanced. (Moo-Young et al., 2003). As TDA is composed of compressed rubber, its material properties will not allow it to absorb any water. The specific gravity of TDA generally

ranges from 1.06 to 1.10. The specific gravity of TDA was determined as 1.08 through ASTM D – 845 – 23. The sieve analysis results are presented in Appendix B.



Figure 3.1: TDA Cutting and Size Segregation

3.3.2 Glass Fiber Reinforced Polymer (GFRP)

In this research, the GFRP rebars were utilized to replace the conventional steel rebars, which have been investigated and proven effective in the past decades. There were several mechanical and physical properties in which the GFRP rebars outperformed the steel rebars. The type of GFRP rebars used in this research was V-Rod 46 type which is specifically designed for structural purposes. These V-Rod 46 GFRP rebars were manufactured by Pultrall Ltd. The #3 (10 mm) GFRP rebars were implemented as reinforcement in the slab-on-grade specimens. These 10 mm GFRP rebars exhibited a guaranteed tensile strength of 1000 mpa, and a minimum tensile modulus of 46 GPA which was obtained according to ASTM D7205 standard. The guaranteed transverse shear capacity of these 10 mm GFRP rebars has been specified as 160 mpa based on the ASTM

D7617 standard in its technical data sheet. These 10 mm GFRP rebars were incorporated with calcium aluminosilicate glass fibers and a urethane-modified Vinylester resin matrix with a minimum fiber percentage of 70% by weight is utilized to coat the rebars. The Effective weight of these 10 mm GFRP rebars ranges between 150 to 152 gm/m which is $\frac{1}{4}$ the weight of conventional steel rebars which range between 620 to 625 gm/m, thus reducing the weight of the structure drastically. The effective diameter of the 10 mm GFRP rebar is 9.49 mm (0.374 inches) and the effective cross-sectional area including the glass fiber coating is 71.12 mm^2 or 0.11 inch^2 according to CSA S806.



Figure 3.2: V-Rod 46 GFRP Rebar

Table 3.3: Properties of 10 mm V-Rod 46 GFRP rebar

Material properties	Estimated values
Guaranteed Tensile strength ASTM D7205	1000 Mpa
Minimum Tensile Modulus ASTM D7205	46 Gpa
Guaranteed Transverse shear capacity (ASTM D76170)	160 Mpa
Resin coating	urethane-modified vinyl ester resin
Weight	150.8 gm/m
Effective Diameter	9.49 mm (0.374 inch)
Effective cross-sectional area	71.12 mm ² (0.11 inch ²)

3.3.3 Geocell

There are several types of geocells with different patterns, made out of various materials, and with different dimensions. In this research, we will be utilizing a geocell type called GF30 which was manufactured by Gridforce. Inserting these types of geocells in the soil as soil reinforcement and assessing, its performance exposed an increase in bearing capacity, under the same relative density. The geocell panels were fabricated using low-density polyethylene (LDPE) in the shape of three-dimensional interconnecting cell panels. The dimensions of each geocell pocket were 70 mm in width, 70 mm in length, and 30 mm in depth. All the cells in each geocell panel were designed with a wall thickness of 3 mm. The geocell panels were manufactured with an interlocking mechanism which is present on the outer side of each geocell panel. All the geocell panels are square and have a width of 500mm. Each panel was designed with (7 X 7) adjacent geocell pockets which were placed perpendicular to each other to increase the friction between the soil particles and to ease out the lateral stress distribution pattern through the subsequent geocell pockets. Figure 3.3 indicates that all the geocell pockets were shaped as interlocking concrete blocks

for better integrity and stress dispersion. Geocell pockets have two 5 mm thick strips running diagonally across the pockets to arrest the soil firmly within the geocell walls. The low-density polyethylene (LDPE) geocell panel had a Young's modulus of 300 Mpa and a tensile strength of 20 Mpa. (Mahgoub, 2019)



Figure 3.3: GF 30 Geocell Panel (Gridforce)

3.4 Design of Slab-on-Grade

Several methods can be utilized to design slab-on-grade. In this research, the PCA method has been integrated to design the slab-on-grade according to ACI 360R standard. Eventually, slab-on-grade were reinforced with several mesh and rebars to accomplish one of these reasons, to control concrete cracks caused due to atmospheric conditions, to provide shrinkage compensation by providing steel bars as shrinkage reinforcement, to provide transverse load carrying capacity, and to reduce the thickness of floor slab by enforcing the slab with structural reinforcement this is done for industrial flooring which

involves heavy loading conditions. The slabs were designed with structural reinforcement with the help of PCA design chart and design of structural slab-on-grade with vehicle loading methodology.

Initially, the concrete slab was designed as a plain slab-on-grade without any rebars or joint spacing with the help of a PCA design chart based on a forklift axle load, tire spacing, lift truck capacity, and vehicle weight. The stress per 1000 lb axle load (Psi) on a single wheel is calculated, the wheel spacing (inch), and effective single wheel contact area (sq in) were determined according to the forklift truck type. Based on these data and the subgrade modulus (K) of the soil an imaginary line was plotted in the PCA chart to identify the slab thickness. The PCA design chart along with the imaginary line is depicted in Figure 3.4. The thickness of the plain concrete slab was obtained as 6 inches based on the Forklift truck specifications through the PCA thickness selection chart.

Depending on this plain concrete slab-on-grade thickness the structurally reinforced concrete slab-on-grade is designed to bring down the thickness of the slab by infusing reinforcement in the slab. The reinforcement design was incorporated from a methodology mentioned under the topic designing of structural reinforcement for a slab with vehicle loading in the book “Designing Floor Slabs on Grade” (Ringo & Anderson, 1996).

Table 3.4: Forklift Details

Load Carrying capacity	3000 lb
Vehicle Weight	5890 lb
Total critical load	8890 lb
Wheel spacing	37.2 inches
Effective contact Area	31.3 inches

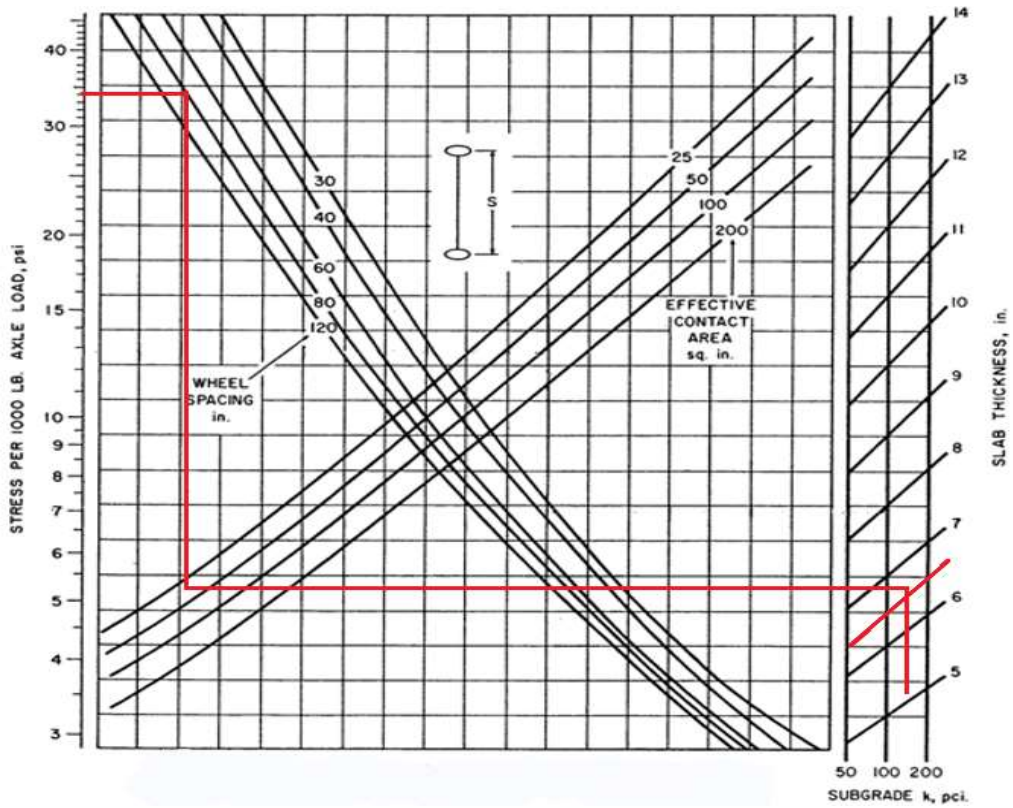


Figure 3.4: PCA Thickness Selection Chart for Single Axle Load (Ringo & Anderson, 1996).

The structural design procedure followed for this method is as mentioned:

1. Calculate the applied moment due to the actual load.

$$\text{The Applied moment of the slab: } M_{app} = SM \times fb \quad \text{and} \quad SM = \frac{bt^2}{6}$$

Where,

fb = allowable stress

b = Base width of the slab section

t = Thickness of the slab section

2. Determine the thickness required for a safety factor of close to 1.10.

$$\text{Allowable stress} = fb_{1.1} = \frac{MOR}{1.1} \quad SM = \frac{M_{app}}{fb_{1.1}} \quad t = \sqrt{\frac{6 \times SM}{12}}$$

3. Using this new thickness, check the slab's actual safety factor for the load-induced cracks.

Assume the nearest thickness value to the derived thickness. Then determine the section modulus for that reduced thickness value and evaluate the safety factor for that slab thickness.

4. Select the load factor to give the design moment (greater than the applied moment).

$$M_u = SF \times M_{app} \quad \text{where } SF - \text{Safety factor.}$$

5. From the design moment, which is the ultimate moment, select the required steel areas and spacings.

$$M_u = \Phi A_s f_y (j_u d)$$

Where,

Φ = capacity reduction factor (0.90 for bending)

A_s = Area of steel

F_y = Yield strength of steel

$j_u d$ = Moment arm (assumed to be 0.9)

Based on this method the slab has been structurally designed to incorporate 10 mm steel rebars as both the main and distribution rebars which has led to the reduction of slab thickness to 5 inches. According to the design of slab-on-grade, the steel rebars and the GFRP rebars were distributed as shown in Figure 3.5, the main rebars were positioned at a distance of 130 mm center to center (C/C), and the distribution rebars were separated by a distance of 125 mm (C/C). The concrete formwork was built out of plywood for a dimension of 805 mm length, 405 mm height, and 127 mm (5 inches) height. Instead of cover blocks, five binding wires were run laterally (breadthwise) inside the form to suspend

the rebars on top of it, at a distance of 75mm from the bottom of the slab. The suspension wires were pulled out of the formwork and wound around a screw placed on the formwork. Both the steel and GFRP rebars were placed inside this foam work with a bottom and side cover distance of 75 mm as mentioned in ACI 360R. The Steel rebars were held in position with each other with a binding wire, whereas the GFRP rebars were held in accurate position and spacing by tightening them against the distribution rebars with zip tags.

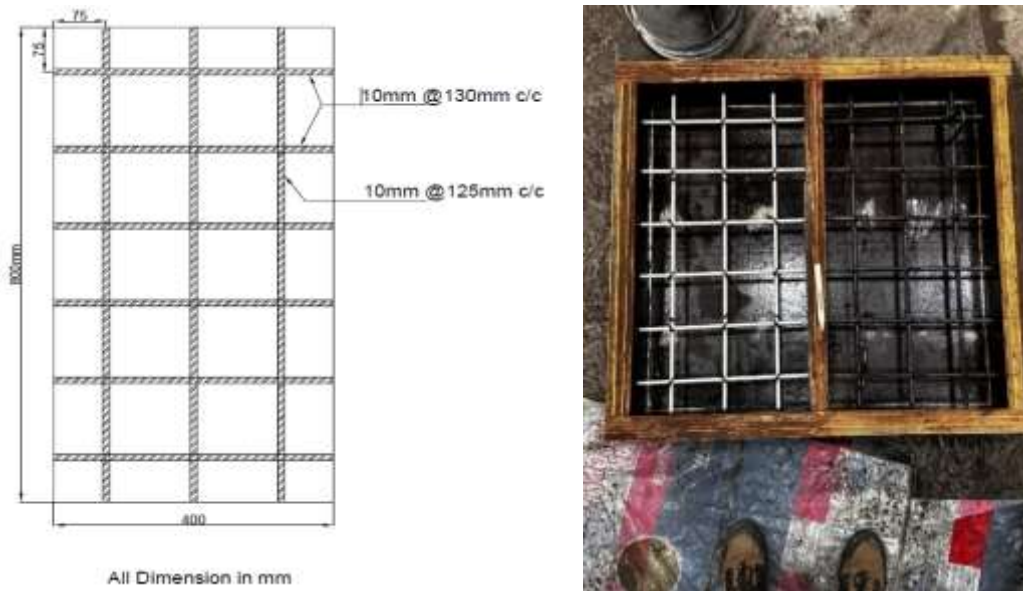


Figure 3.5: Reinforcement Distribution Diagram and Slab Formwork

All slab specimens were provided with U-hooks diagonally at the corners, these U-hooks were connected to the rebars to create a substantial bond with the slab specimen. These U-hooks were utilized to lift the slab out of the form, place it for curing, and also for placing the slab inside the soil tank for testing.

3.5 Concrete Mix Design

In this investigation, three different concrete mix designs were formulated according to the ACI 211.1 standard. The slump was selected as 3 to 4 inches, and the aggregate size was 19 mm, the concrete was designed according to a non-air-entrained concrete mix. The water-cement ratio was estimated to be 0.435 to attain a reliable compressive strength of 38.5 kN on the 28th day. Based on these derived values, the normal concrete mix design for 1 m³ volume was estimated for an M30 grade of concrete following the ACI 211.1 “Recommended practice for selecting proportions for concrete”. Once the base control specimen mix was formulated, the 10%-TDA and 20%-TDA concrete mix designs were calibrated by replacing the coarse aggregate with TDA in terms of its volume (10% and 20%). A mid-range water-reducing and plasticizing admixture “Plastol 341” has been utilized as a superplasticizer in all the mix designs. Plastol 341 provides improved finishability, workability, and superior slump retention, develops a greater strength at an early age, drops down the permeability, and increases the durability of the concrete mix. The Normal concrete mix (NCM) design is shown in Table 3.5. The mix design for one slab and three cylinders (CS, 10%-TDA-CM, and 20%-TDA-CM) is exhibited in Table 3.6. Eventually, three cylinders of size (4-inch diameter X 8-inch height) were cast for each mix design and examined to determine their compressive strength, which is presented in Appendix C.

Table 3.5: M30 Grade Concrete Mix Design

Volume	Mass of Water	Mass of Cement	Mass of FA	Mass of CA	Mass of SP
1 m ³	205 Kg/m ³	472 Kg/m ³	693 Kg/m ³	1013.2 Kg/m ³	944 ml/m ³

**Table 3.6: Mix Design for One Slab and 4 Cylinders
(NCM, 10%-TDA-CM, and 20%-TDA-CM)**

Mass of Material	NCM	10%-TDA-CM	20%-TDA-CM
Mass of Water	10.2	10.2	10.2
Mass of cement	23.92	23.92	23.92
Mass of FA	35.12	35.12	35.12
Mass of CA	51.35	46.23	41.2
Mass of TDA	-	3.4	6.8
Mass of SP	50 ml	50 ml	50 ml
Mix Ratio	1: 1.46: 2.14	1: 1.46: 1.93	1: 1.46: 1.72
Slump	3 to 4 inch	3 to 4 inch	3 to 4 inch

3.5.1 Casting of Concrete Slab-On-Grade

Casting of all slab specimens was done outside the soil tank as the soil tank cannot accommodate all the specimens in it simultaneously. Figure 3.6 presents the concrete casting according to the casting methodology. All the concrete ingredients were batched weighed, and mixed using a concrete mixing machine, the superplasticizer “Plastol 341” was measured using a clinical syringe according to the required quantity and was mixed with the water before mixing. Every concrete slab mix was evaluated by executing a slump test to ascertain the slump range. Once the slump was determined, the concrete mix was shoveled inside the concrete slab formwork. After filling up to $\frac{3}{4}$ the height of the formwork, the concrete volume was tamped, and later rest of the concrete was shoveled into the formwork. The concrete was tamped and vibrated using a vibrating tool, a tamping rod, and a mallet to avoid air voids and honeycomb formation at the bottom of the slab.

Three concrete cylinders of size (4 inches diameter and 8 inches depth) were cast along with each slab specimen to determine the compressive strength of each slab mix. Table 3.7 exhibits a brief description of all the slab specimens.

Table 3.7: Casting Details of All Specimens

Specimen ID	Mix Design	Reinforcement	Casting date	Slump
CS	NCM	Steel	21 st August 2023	3.5 inch
10%-TDA-GFRP-1	10%-TDA-CM	GFRP	23 rd August 2023	3 inch
20%-TDA-GFRP-2	20%-TDA-CM	GFRP	28 th August 2023	3.25 inch
10%-TDA-GFRP-2	10%-TDA-CM	GFRP	30 th August 2023	3.25 inch
20%-TDA-GFRP-2	20%-TDA-CM	GFRP	28 th August 2023	3.5 inch
GFRP-1	NCM	GFRP	27 th November 2023	3.5 inch
GFRP-2	NCM	GFRP	29 th November 2023	4 inch



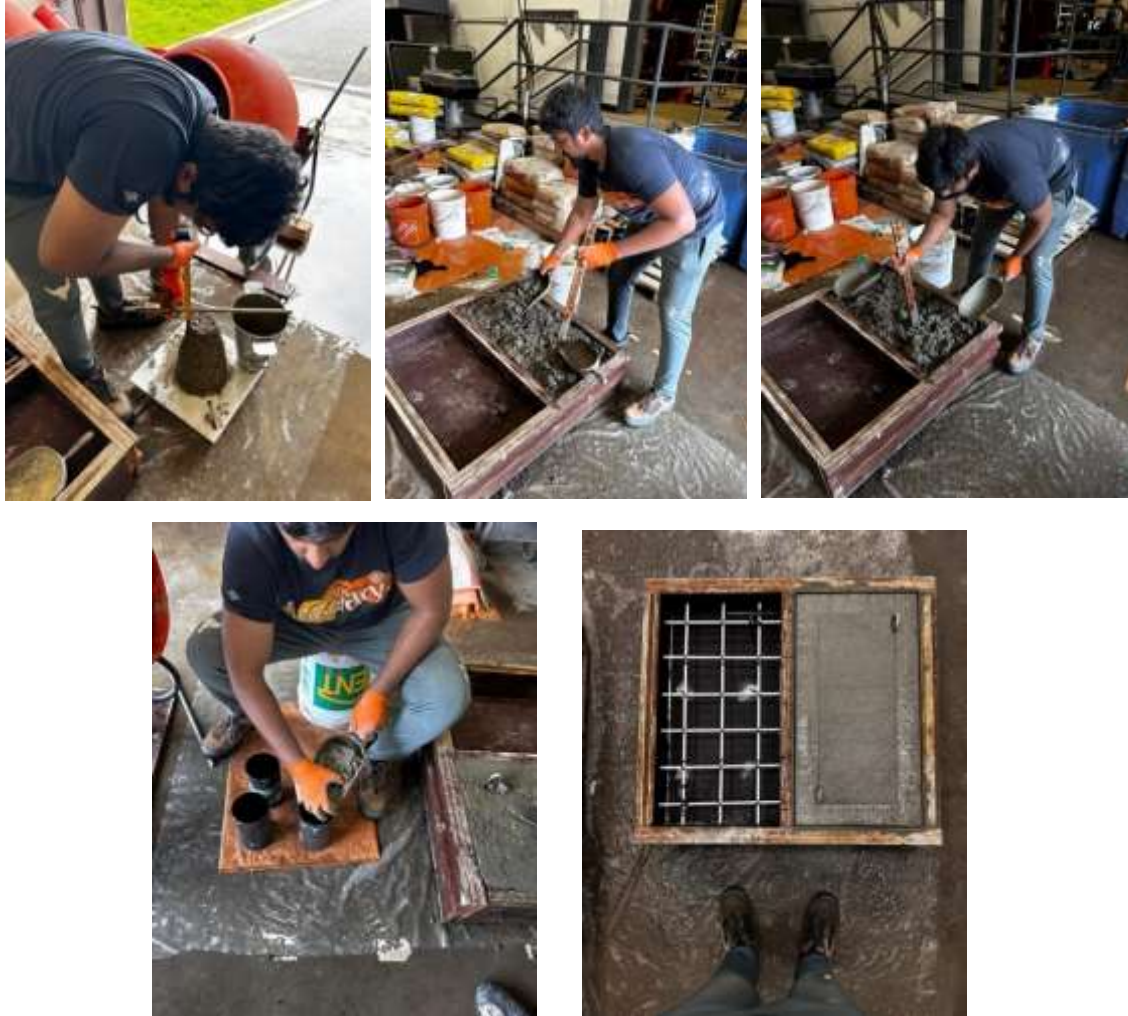


Figure 3.6: Concrete Slab and Cylinder Casting

3.5.2 Concrete Curing Method

Once casting was completed for a slab specimen, it was demoulded from the formwork and placed on a foam sheet for curing. Each cylinder specimens cast along with the slabs were demoulded and marked accordingly, every cylinder was placed on top of its respective slab specimens which allowed them to be cured under the same atmosphere condition. All the specimens were moist-cured with the help of jute burlap layers. The specimens were wet using a water sprinkler and it was covered entirely with jute burlap layers, every layer was soaked in water initially before covering. Then they were enclosed with thick plastic sheets

in all directions and wooden boards were placed on all four sides to conceal them from the exterior lab atmosphere. This was executed precisely for every slab to retain the moisture on the concrete surface and jute burlap layers. Furthermore, during the next seven days, the specimens and their jute layers were soaked completely in water twice daily to maintain the moisture imposed on them. After seven days of moist-curing all the specimens were moved and placed in a dry location for air curing, they were left alone for the rest of the days until testing. Figure 3.7, represents the moist-curing method.



Figure 3.7: Slab Specimen Moist-Curing.

3.6 Soil Subgrade Preparation Method

The Soil tank used in this research is made out of steel, initially, the tank contained soil for $\frac{3}{4}$ of its depth. The soil in the tank was completely excavated manually with a shovel. To procure a subgrade that was leveled out and with the same subgrade modulus, comparatively oscillating wet and dry unit weight and similar relative density. The excavated soil was shoveled into the heavy-duty industrial nylon sandbags which can acquire up to 2 tons of soil. The steel soil tank dimensions were 2.75 m in length, 2.25 m in breadth, and 1.80 m in depth. The steel tank's walls were intentionally made with

significant rigidity to avoid any lateral displacement caused by the load distribution inside the soil tank during testing. All four walls were surrounded with high-density polyethylene sheets. Before restoring the soil in the tank, the interior steel tank wall conditions were inspected, to identify any wear and tear on the high-density polyethylene sheets which protect the steel walls from soil and moisture. The torn portions of the polyethylene sheets were patched up with the help of 3M duct tape, to prevent the soil from breaching through those holes and corrode the steel tank due to its moisture content. The soil was filled in the tank with the help of an industrial lift crane, the nylon sandbag was positioned on top of the soil tank and opened from the bottom, dumping the whole volume of soil inside the soil tank. Once loosened, the bottom layer of the soil was distributed evenly with the shovel and leveled out accurately with a plywood sheet to obtain a flat surface. The leveled-out soil was moist uniformly with cold water through a water sprinkling tool with 12 liters of water, the soil was then compacted utilizing a hand tool. A wooden plank (500mm X 500mm) was placed on top of the leveled soil, and on top of that, the hand compacting tool was placed. The compaction method is exposed in Figure 3.9. The drop weight present in the compaction tool was lifted to 2 feet and dropped three times in a single spot. Then the wooden plank was moved to the next position beside it, and again the same mechanism was followed to compact it. Likewise, the whole soil layer was compacted by repeating the same compacting mechanism. Once the soil layer is compacted, two distinct locations are selected, and the sand cone test is executed based on the ASTM D1556 standard. The wet unit weight and dry unit weight were calculated corresponding to this standard. The compaction method has been designed accordingly to attain a relative density of 45% to 50% accomplishing a medium state of the soil. The relative density was determined

according to the ASTM D 698 standard. The rest of the soil mass was poured and compacted layer by layer utilizing the same compaction mechanism, followed by the sand cone test, and calculation of relative density. Every day the soil layers were covered with 2-inch-thick foam sheets and the corners were covered with plastic bags to maintain the moisture content in the soil subgrade. A single heavy-duty industrial bag can give up to a 150 mm thick soil layer in the soil tank. Thus 10 layers of soil were compacted to attain a soil subgrade with a depth of 1.5 meters. Figure 3.8 shows the soil layer compaction model. The top layer of the soil was measured meticulously with a spirit level scale to validate the horizontal soil surface level. After examining every specimen, the test specimen was removed and the top layer of soil was disturbed and shoveled out into the heavy-duty sandbags. Around 250 mm to 300 mm top layer of the soil was removed which procures around 2 industrial sandbags.

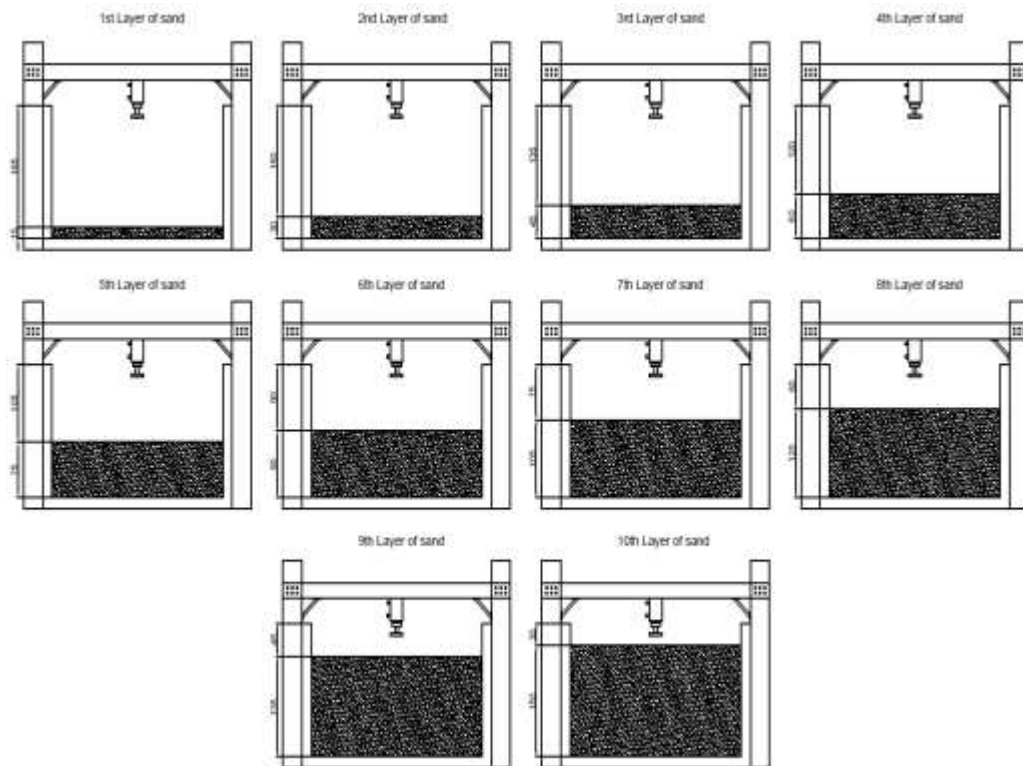


Figure 3.8: Soil Layer Compaction Model

Apart from that the Top -1 Layer of the soil will be disrupted by scooping and inverting the whole soil layer with an excavation shovel, this method disorients the soil particles up to an additional depth of 250 mm to 300 mm and loosens the soil layer. Therefore almost 500 mm to 600 mm soil subgrade is disrupted by easing out the soil particles from the compressed state which was caused by the previous test. Eventually, the same compaction mechanism adheres to prepare the soil subgrade layer by layer till top soil is leveled out, compacted, and tested for relative density. The compaction method was modified for the CS and the 10%-TDA-GFRP-1 specimen's test alone. The top 500 to 600 mm of soil layer was compacted layer by layer, based on the same compaction procedure with a slight modification. The drop weight was lifted and dropped eight times in a single spot and it was repeated throughout every soil layer to attain a subgrade with 70% relative density.

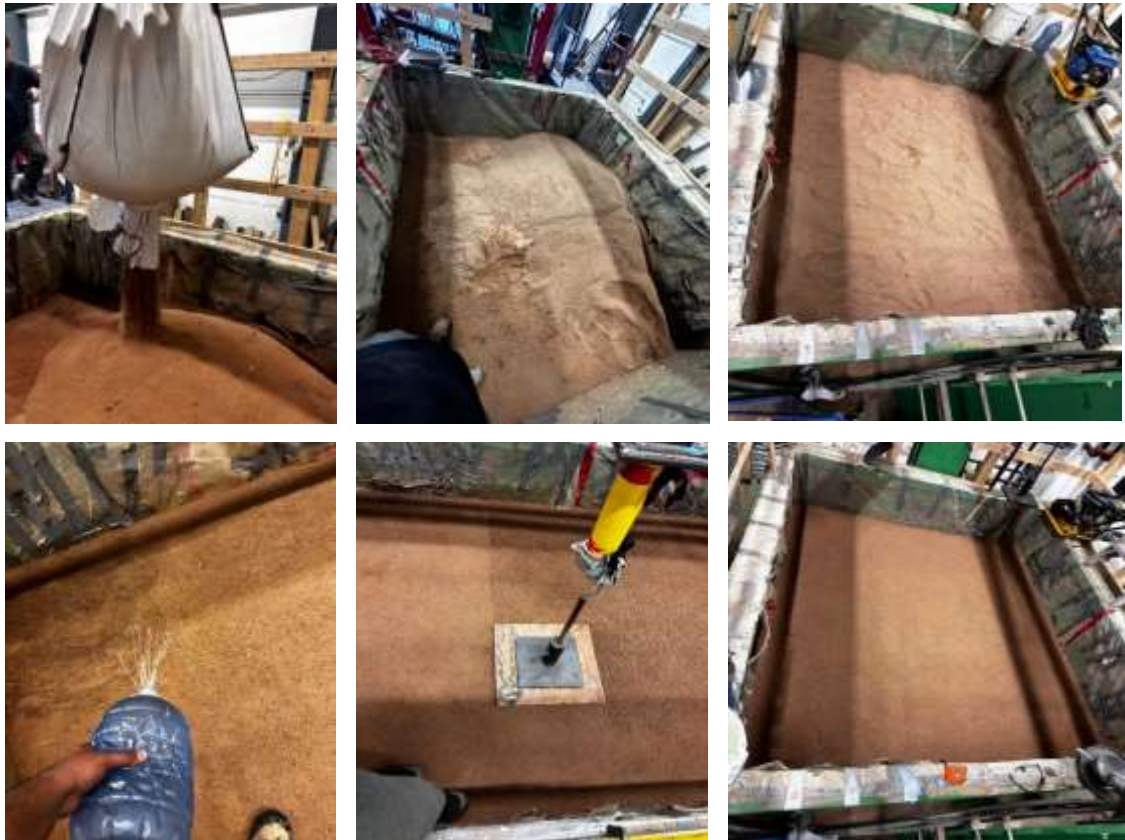


Figure 3.9: Soil Tank Preparation Method

3.7 Subgrade Test Methodology

3.7.1 Sand Cone Test

The Sand cone test was executed according to ASTM D1556/D1556M standard. Measure the weight of the sand cone container with and without silica sand in it. Spread a plastic sheet on a flat surface and position the sand cone container on top of the sheet, open the nozzle, and let the silica sand follow through it and fill the cone. Measure the overall weight of the container and calculate the weight of silica sand in the cone. Repeat this procedure thrice to obtain an average weight of silica sand in the cone (W_{CON}). Select a location in the sand layer at which the sand cone test can be executed. Once, the location is selected make sure that it is flat and leveled evenly. Place the base plate from the apparatus, and ensure that it is in contact with the soil around the edge of the flanged center hole. The volume of the test hole depends on the maximum soil particle size and the depth of the compacted layer. The minimum volume of the test hole depending on the maximum particle size is shown in Table 3.8. Mark the circumference of the central base plate hole, excavate the soil with a scoop, and accumulate the entire soil mass which was scooped out from the test hole in a zip-lock plastic bag. Preserve this soil airtight to avoid moisture reduction from the soil. Clean the base plate completely, invert the sand cone apparatus, and place the funnel precisely on the hing of the central hole. Open the nozzle and let the silica sand fill the hole and the cone. Do not vibrate or touch the apparatus during the flow of sand, once the silica sand fills up and the flow is disrupted, conceal the nozzle and determine the weight of the sand cone container with the rest of the silica sand and evaluate the weight of silica sand present in the hole alone (W_H). Obtain the weight of the wet sand (W_{Wet}) removed from the sand layer initially. Mix the wet soil thoroughly, collect two soil samples

in a small soil sample container, and investigate the moisture content in the soil by performing a moisture content test. The moisture content test was implemented following ASTM D2216-19. The mass of the sample container was noted, and the wet soil sample was placed in the container and weighed to obtain the wet soil sample mass. Then the samples were kept inside an oven and dried at a temperature of $110 \pm 5^\circ\text{C}$. The samples were left to dry for 24 hours, then the mass of dry soil was obtained, and the moisture content (ω) was calculated in percentage. The wet and dry unit weight of the soil will be evaluated based on these obtained parameters using these equations. The sand cone test calculation is presented in Appendix A.

$$V_{\text{Hole}} = \frac{Wh}{\gamma_{\text{silica}}}$$

$$\text{Wet unit weight } \gamma_{\text{wet}} = \frac{W_{\text{wet}}}{V_{\text{hole}}}$$

$$\text{Dry unit weight } \gamma_{\text{dry}} = \frac{\gamma_{\text{wet}}}{1 + \frac{\omega}{100}}$$

Where, V_{Hole} – Volume of the hole.

W_{wet} – Weight of wet soil

ω - Moisture content in the soil

γ_{silica} – Unit weight of silica sand (1.44 gm/cm^3)

Table 3.8: Minimum Test Hole Volume (ASTM D1556/D1556M)

Maximum Particle Size		Minimum Test Hole Volumes	
in.	mm	cm^3	ft^3
1/2	12.7	1415	0.05
1	25.4	2125	0.075
1 1/2	38	2830	0.1

3.7.2 Laboratory Compaction Test of Sandy Soil

A substantial amount of soil was collected from the soil present in the tank. The laboratory compaction test was conducted according to ASTM D698. The soil was spread evenly on a steel tray and then dried completely in an oven for 48 hours at 105°C. A certain amount of soil was poured into the test mold in three layers for a selected molding water content. Each layer will be compacted using a drop weight of 5.50-lbf (24.47 N) for 25 to 56 blows. The rammer was dropped from a height of 12.00 in. (304.8 mm), subjecting the soil to a total compaction effort of about 12400 ft-lbs/ft³ (600 kN-m/m³). A 4-inch mold was used to compact the soil and sustain the guide sleeve at an angle of 5°. Implement the strikes consistently, averaging approximately 25 blows per minute, to ensure that the entire surface of the specimen was uniformly covered. Once all three layers were compacted, the corresponding dry unit weight of that soil sample for a certain water content was estimated. The exact procedure was done repetitively for the new soil mass with incremental moisture content (ω), the moisture content was escalated by 2 to 4 percent for every new sample. The test was repeated until the dry unit weight started to decline linearly after a certain amount of moisture content. From the obtained data a relationship was derived out of dry unit weight and molding water content of the soil. Based on this relationship, a graph can be plotted with moisture content on the X-axis and dry unit weight on the Y-axis, which produces a curvilinear pattern known as the compaction curve. A thorough analysis of the compaction curve yields the optimum moisture content and maximum dry unit weight. The Minimum dry unit weight was evaluated using the mold, water, and dry soil sample. Initially, the weight of the empty mold was measured, then the mold was filled with water and the weight was recorded, again the mold was entirely filled with sand and weighed

without any compaction. Depending on these terms the minimum dry unit weight was measured. These parameters were determined to derive the relative density of the soil layer. The relative density was evaluated for each layer to maintain the compaction of the soil layer between 45 to 50% to replicate a medium soil subgrade. The relative density (RD) is ascertained based on this formula.

$$Rd = \frac{\gamma_{dmax} (\gamma_d - \gamma_{dmin})}{\gamma_d (\gamma_{dmax} - \gamma_{dmin})}$$

Were,
 γ_{dmax} – Maximum dry unit weight
 γ_{dmin} – Minimum dry unit weight
 γ_d – nominal dry unit weight of soil layer.

3.8 Slab Test Setup Procedure

Once all the soil layers were compacted, the sandy subgrade was prepared to execute the test. A load cell which is calibrated for 300 kN was affixed to the bottom of a two-way acting hydraulic actuator. This load cell was interlinked to the testing data acquisition system, to track the total amount of load which was exerted on the slab. A circular bearing Plate of diameter 200 mm and height 30 mm with a steel lever arm that is 150 mm long was connected to the bottom of the load cell. Every slab specimen was installed with four 120-ohm strain gauges. Two strain gauges were positioned on the top surface of the slab and the other two were positioned at the bottom surface of the slab. The location of the strain gauges is shown in Figure 3.10 (a). Each slab specimens were lifted and instated precisely in the middle of the top surface, beneath the two-way acting hydraulic actuator. The hydraulic actuator was connected with the advance and retrieve oil valves, and the actuator was jogged down to bring the bearing plate in contact with the concrete slab top surface. The slab was positioned in such a way that the bearing plate meets accurately in

the middle of the slab leaving a 100 mm gap between the length side of the slab. The cross-section diagram of the slab testing method is depicted in Figure 3.10 (b). Two I-section steel beams were placed on top of the soil tank boundaries in the length direction about 1 foot above the slab. It was held in position with the help of clamps on either end of the I-section beam. These Steel beams were utilized as supporting beams to align all the linear Variable Differential Transformers (LVDT) according to their orientation. For every slab specimen, 6 LVDTs were installed in their positions, coexisting on the top alongside the length of the slab. Two LVDTs were imposed at the corners and one LVDT was situated in the middle, on both sides in the length direction. The corresponding orientation of the LVDT is depicted in Figure 3.11.

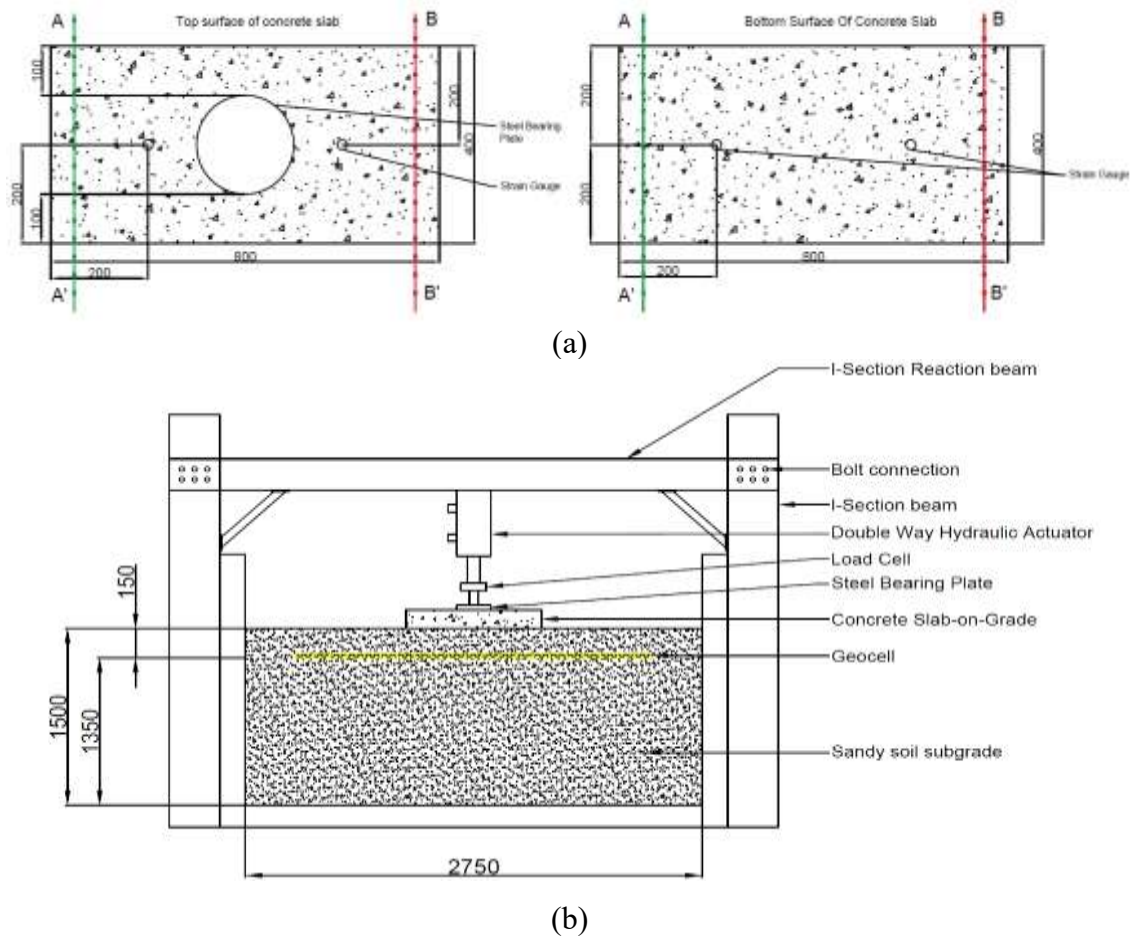


Figure 3.10: (A) Strain Gauge Position (B) Slab Testing Cross-Section Diagram

After every LVDT was aligned in its position, each one was assessed if it was exactly vertical to the slab with the help of a digital angle gauge leveling tool. All the six LVDTs were bridged with separate channels to the data acquisition system.

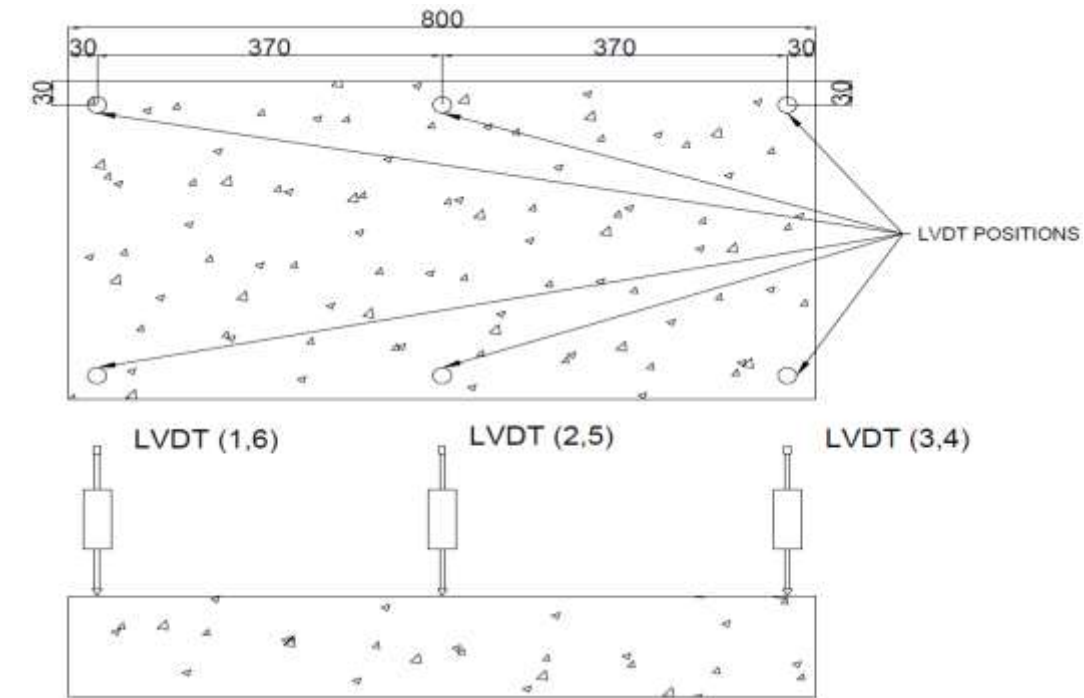


Figure 3.11: LVDT Layout and Positioning

Once all the LVDTs were set, the moveable displacement measurement shaft was disturbed to check if all the LVDTs were transmitting displacement data to the system. The CS, 10%-

TDA-GFRP-1 were tested on normal soil subgrade with relative density varying between 65% to 70%. While the GFRP – 1, 10%-TDA-GFRP-2, and 20%-TDA-GFRP-1 slab specimens were experimentally tested on top of a normal sandy soil subgrade condition, maintaining the relative density of soil between 45 to 50 percent. Whereas GFRP – 2, and 20%-TDA-GFRP-2 specimens were examined over a geocell-reinforced sandy soil subgrade condition. The geocell was incorporated in the soil strata at a depth of 150 mm below the top surface. These two specimens were investigated on top of this soil condition, constituting a relative density of 45 to 50 percent. All the slab specimens were examined under monotonic load test methodology.

3.9 Testing Procedure

3.9.1 Compression Test on Concrete Cylinder

The compressive strength of the concrete mix was assessed following the test procedure prescribed in ASTM C39/C39M standards. All the cylinder specimens were cast using a cylinder mold along with their corresponding slab specimens and cured with them to attain similar strength. Every cylinder specimen was capped using sulfur mortar to obtain a flat surface on both phases. The experimental procedure involves subjecting concrete cylinders to a compressive axial load at a rate within a specified range until failure transpires. Each cylinder was tested separately with an ultimate testing machine (UTM) which loads the specimen at a rate of 2 mm/min. Dividing the peak load achieved during the test by the cross-sectional area of the specimen results in the specimen's compressive strength. Initially to validate the concrete mix Design 3 cylinders with dimensions 150 mm X 300 mm (diameter X height) were cast for the plain concrete mix, 10%-TDA concrete mix, and 20% TDA concrete mix and tested. Apart from this, all the other cylinder

specimens were cast with the corresponding slab specimens with a dimension of 100 mm X 200 mm (diameter X height).

3.9.2 Plate Load Test

The Load-bearing capacity of soil is one of the most important parameters of soil investigation which can be used to design slab-on-grade, pavements, design of foundations, and so on. In this research, a non-repetitive static plate load test was performed on the sandy soil to determine the bearing capacity of the soil. This test was executed following the ASTM-D1194 standard. The test was implemented with the displacement-controlled method. This testing procedure evaluates the soil's load-bearing capacity under field loading circumstances using a specified bearing plate and depth of embedment. A two-way acting hydraulic actuator with a loading capacity of 50 tons (440 kN) has been installed and utilized for this test. A load cell which was calibrated for 300 kN has been screwed and secured at the bottom of the actuator to electronically transmit the quantity of load superimposed on the soil layer. A steel bearing plate with 200 mm diameter and 30 mm thickness, with a 150 mm lever-arm (stem) was interconnected underneath the load cell. A similar steel plate of the same dimensions without a lever-arm was rested on the soil layer precisely beneath the bearing plate. The actuator was jogged down and brought into contact with the resting steel plate. Two LVDTs were calibrated and installed on top of the bearing plate with the help of supporting beams, to transmit the settlement values to the Data Acquisition system. The data will be recorded for every second with an accuracy of 0.001 mm. Two LVDTs were positioned on opposite sides of the circular plate to quantify the extent of settlement, and the mean settlement value derived from these two measurements was considered. The Test was executed with a displacement rate of 1 mm/min. The test was continued at the same rate till the soil subgrade collapsed or if the soil subgrade settled to

a depth of 40 mm. The plate load test was executed for unreinforced and geocell-reinforced sandy soil subgrade conditions. Figure 3.12 depicts the plate load test setup and the response of the soil surface.



Figure 3.12: Plate Load Test Setup

3.9.3 Monotonic Load Test on Concrete Slab-On-Grade

The monotonic load test is implemented successfully following the ASTM-D1196 standard. Monotonic load test is the application of continuously increasing load or stress on a structure without any intermediate reversal of load. The Load will be imposed in one direction, without any repetitive load cycles. A two-way acting hydraulic actuator with a capacity of 50 tons (440 kN) was mounted and employed for this test. A load cell calibrated for 300 kN has been screwed to the bottom of the actuator to electronically

propagate the amount of load superimposed on the concrete slab specimen. A steel bearing plate with a diameter of 200 mm and a thickness of 30 mm was interconnected beneath the load cell with a 150 mm lever arm (stem). The test procedure follows these loading mechanisms and imposes the load at an appropriate rate with constant increments. To generate a precise load-deflection curve, the magnitude of each load increment must be modest enough that enable the recording of a minimum of six load-deflection points. The Application of load was done with the hydraulic actuator at a load incremental rate of 20 kN. Following the application of each load incrementation, allow the slab to enact for that magnitude of load, and ensure that the settlement rate prevails under 0.001 in (0.03 mm)/min for three consecutive minutes. Record the load and settlement of all six LVDTs for consecutive three-minute intervals until attaining 0.03mm/min of deflection rate. Apart from recording the load and settlement data during the load intervals, the slab specimen and the soil layer were meticulously examined to identify cracks at every 5-minute interim. Once, the concrete yielded and the initial crack developed, the crack width was recorded at every load increment interval, and the soil crack distribution pattern was observed. Repeat this process until the desired total settlement of 30 mm has been accomplished or until the device reaches its maximum load capacity. As the slab specimen acquires 30 mm of settlement maintain the magnitude of load at the same level until the settlement rate endures under 0.001 in (0.03 mm)/min for three consecutive minutes. Substantially start releasing the load with a slow decrementing manner, and continue this decrementation process till the load drops down to zero setting load. Record the settlement of the slab specimen at zero setting load. This methodology is followed for all specimen types under unreinforced and geocell-reinforced soil subgrade conditions.

CHAPTER-4 PLATE LOAD TEST AND MONOTONIC LOAD TEST RESULT COMPARISON

4.1 Introduction

The experimental laboratory investigation results acquired from plate load tests conducted under both sandy soil subgrade conditions, and monotonic load tests on slab-on-grade specimens under unreinforced sandy soil subgrade, were presented in this chapter. Plate load tests examined the sandy soil response for unreinforced and geocell-reinforced subgrade. The generated test data was discussed and analyzed to determine the appropriate subgrade bearing capacity and peak load attained for both soil conditions. The experimental response for each slab specimen is characterized by generating a graph with the centrally applied load against the settlement of the slab strip, the stress-strain curve was plotted using the strain values exhibited by the concrete slab, the soil cracking load, soil crack pattern, and the concrete crack loads are investigated.

4.2 Plate Load Test Results Comparison

Response of Sandy Soil Subgrade on Both Subgrade Conditions

Preceding the plate load test setup, the soil subgrade forming the top two layers is excavated manually using a shovel, and the third layer of the soil subgrade is inverted utilizing a shovel inside the soil tank. This is done to loosen the top 1/3 (500 mm) depth of the soil subgrade and disintegrate the compressed soil mass. Once loosened, the third layer of the soil is spread evenly all around the tank with a wooden plywood sheet to obtain a flat soil surface. Three bottles of water with a capacity of 4 liters would be sprinkled uniformly throughout the surface. The soil layer was compacted using the compaction method mentioned above to attain a subgrade with a relative density of around 45 to 50%. The Plate

load test was set, and the soil was assessed according to ASTM D1194 standards. The testing was implemented with the displacement-controlled method, with a 1 mm/min loading rate. Once the normal soil was examined, the top two layers of the soil were removed and the geocells were inserted into the soil subgrade at a depth of 150 mm beneath the surface level, and the soil was compacted. The soil was compacted with one blow instead of three blows, to maintain the relative density of the soil between 45% to 50%. The experimental displacement-controlled plate load test comparison between the response of normal soil subgrade and the response of geocell-reinforced subgrade soil condition has been depicted in Figure 4.1. The non-geocell normal soil subgrade manifested a stiffer subgrade reaction against the load imposed during the initial phase of testing, from the comparison graph it is evident that above kN of load, the soil stiffness plummeted causing excessive settlement in the soil stratum, whereas the geocell-reinforced subgrade proclaimed a stiff behavior throughout the test. The bearing plate attained 25 mm settlement at a load of 6.099 kN for the normal soil, while the addition of geocell enhanced the soil pressure distribution pattern causing the geocell-reinforced soil to settle 25 mm at a load of 8.493 kN.

The Test was terminated once the soil settled 40 mm. Subsequently, the normal soil acquired a settlement of 40 mm at a load of 7.724 kN. The soil subgrade developed several stress-induced cracks. Based on Terzaghi's failure mechanism as the soil lost its stiffness, the radial shear force induced by the bearing plate transmitted the subgrade from its elastic to plastic state, leading to the development of a shear crack pattern, and surface heaving of soil in the passive zone surrounding the plate. Comparatively, the geocell-reinforced soil procured 40 mm of settlement at 10.577 kN.

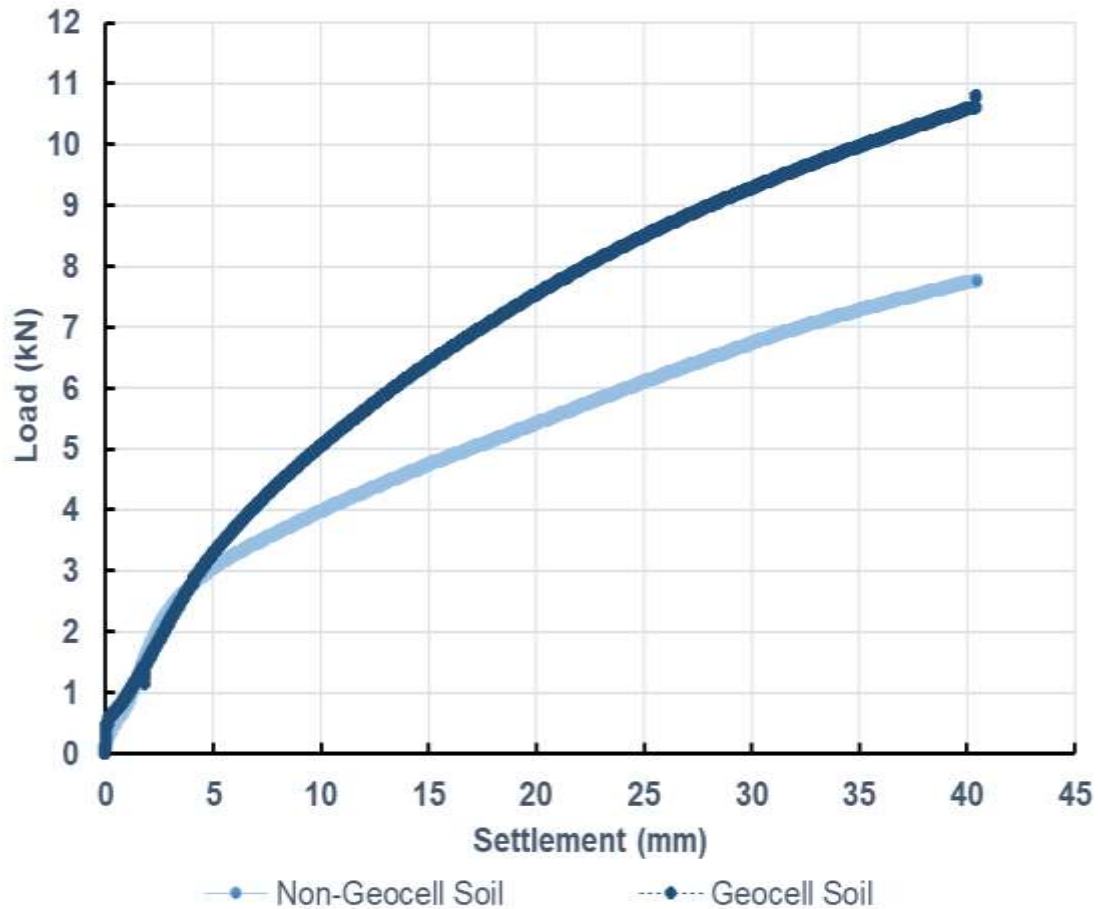


Figure 4.1: Plate Load Test Comparison

The soil had a stress-induced elongated crack deviating outwards from the loading plate. Still, the soil subgrade did not experience any surface heaving pattern in the passive zone, emphasizing that the soil did not lose its elasticity. The insertion of geocell has enhanced the soil properties and structurally made the soil compatible by increasing the loading carrying capacity of the geocell-reinforced soil, avoiding load-induced failure. The normal soil achieved a load-bearing capacity of 235.18 kN/m². In comparison, the soil with geocell attained a significantly greater load-bearing capacity value of 326.83 kN/m² and has proclaimed around 38.97% inclination of bearing capacity compared to the normal soil. Table 4.1 illustrates the response of the plate load test on both subgrade conditions.

Table 4.1: Response of Plate Load Test

Soil Type	Settlement (mm)	Load (kN)	Bearing capacity at 40mm (kN/m ²)
Normal Soil	@ 25 mm	6.099	235.18
	@ 40 mm	7.724	
Geocell reinforced soil	@ 25 mm	8.493	326.83
	@ 40 mm	10.577	

Thus, the Geocell has enhanced the stiffness, elasticity, loading capacity, and bearing capacity and developed a uniform stress distribution pattern in the soil stratum. The soil crack pattern and soil surface heaving have been shown in Figure 4.2 for both soil conditions.



(a)



(b)

Figure 4.2: Plate Load Test Response of (a) Normal soil (b) Geocell-Reinforced soil

4.3 Monotonic Load Test of Slab-On-Grade Specimens on Normal Soil

This experimental study was conducted on a large metal soil tank in the heavy structure lab at Dalhousie University. Once the soil was leveled and compacted to the required relative density of 50% the slab specimens were positioned exactly in the middle of the soil surface and tested under monotonic load according to ASTM D1196 standard. GFRP-1, 10%-TDA-GFRP-2, and 20%-TDA-GFRP-1 slabs were examined by position on top of normal sandy soil subgrade. A data acquisition software called “Strain Smart 8000” was utilized to gather electronically transmitted test data. Once each slab is tested, the slab specimen is removed and the top three layers (500 mm to 600 mm) of soil subgrade are excavated to diminish the stress induced in the soil due to the previous slab testing. The top three layers of the soil were then reinstated following the same compaction mechanism. This procedure would be executed before every other slab specimen is tested.

4.3.1 Subgrade Response of GFRP-1 Slab

The load and settlement data acquired through the data acquisition system was used to determine the average settlement value of all the six LVDTs placed on top of the slab specimen and plotted against the load applied on the specimen. The relative density of the normal soil was 48.69 %. Figure 4.3 represents the load vs settlement curve test results for the GFRP-1 slab specimen. Initially, as the load was imposed on the slab the soil exposed a stiff and elastic behavior until the 20 kN standby load. From Figure 4.3 it was evident that the slab had sunk up to a depth of 3.23 mm. While inspecting the soil and slab at the 20 kN load interval, the concrete did not generate any flexural or tensile cracks and the soil did not develop any surface cracks surrounding the specimen. The hydraulic actuator was maintained at the 20 kN mark until there was a minimum deflection of 0.03 mm/min in the settlement value of each LVDT for 3 consecutive minutes. It took 5 cycles of 3-minute settlement inspections to attain the required minimum settlement difference. In the first cycle, the slab had an average settlement of 3.0061 mm and at the 5th cycle of 0.03mm/min inspection, it ended with a settlement of 3.2316 mm. The concrete slab had a compressive strain of -10.143@ SG1 and -12.201@ SG2. The strain on the tension side was 12.172@ SG3 and 10.674@ SG4 almost the same as compressive strain values.

The load inclination method was maintained similarly for every 20 kN incrementation to attain a similar trendline for every loading session. The load was increased to 40 KN manually using a portable hydraulic oil pump. During the loading phase, the slab and soil surface were inspected visually to identify the cracking point. The soil developed cracks elongating outwards from the four corners of the slab around 36 kN of load. At the 40 kN load interval the soil was subjected to settle under the same load for 7 consecutive 3 min

settlement inspection cycles. During these inspection cycles, the slab settled to 12.618 mm during the first and 13.17 mm in the last inspection, the shear crack on the soil surface was measured to be around 12.3 and 12.4 mm long on both corners of the A-A' section. In section B-B' the corner crack was around 13.6 to 13.7 mm. The concrete slab had no flexural or tensile cracks on the 40 kN interval. The Maximum strain on the compression side of the slab was -18.764@ SG 1 and -22.368@ SG 2, and the maximum strain on the tension side was determined to be 24.852@ SG 3 and 24.397@ SG 4.

Eventually, the load was increased manually to 60 kN using the load control value. The concrete did not develop cracks during the loading and load withholding phase. During the loading phase slab attained an average settlement of 25 mm at a load of 59.524 kN. The soil surface developed several lateral cracks running parallel to the length of the slab, engaging the soil to converge inwards. It took 8 repetitive inspections on all the LVDT values to attain 0.03mm/min variable deflection. The average settlement was 27.557 mm during the first inspection, and it ended up at 28.133 mm for the last inspection. The soil had developed several elongated cracks both at the corners and on all of its four sides, the corner crack widened propagating several other cracks as the slab settled down. The Maximum strain on the compression side of the slab was at -25.357@ SG 1 and -31.009@ SG 2, and the maximum strain on the tension side was determined to be 36.01@ SG 3 and 37.613@ SG 4.

Since the strain was high on the tension side, the slab was pushed to 80 kN load even after attaining a settlement of 25 mm. In this load increment phase, the slab attained its peak capacity and developed a tensile crack on the tension zone, which then prolonged the slab's length side. The GFRP-1 specimen developed flexural cracks at a peak cracking load of

69.141 kN. From Figure 4.4 it can be observed that the stress-induced strain had a linear relationship, exhibiting the elastic behavior of the slab specimen until the crack happened, beyond cracking the slab transitioned into a plastic behavior.

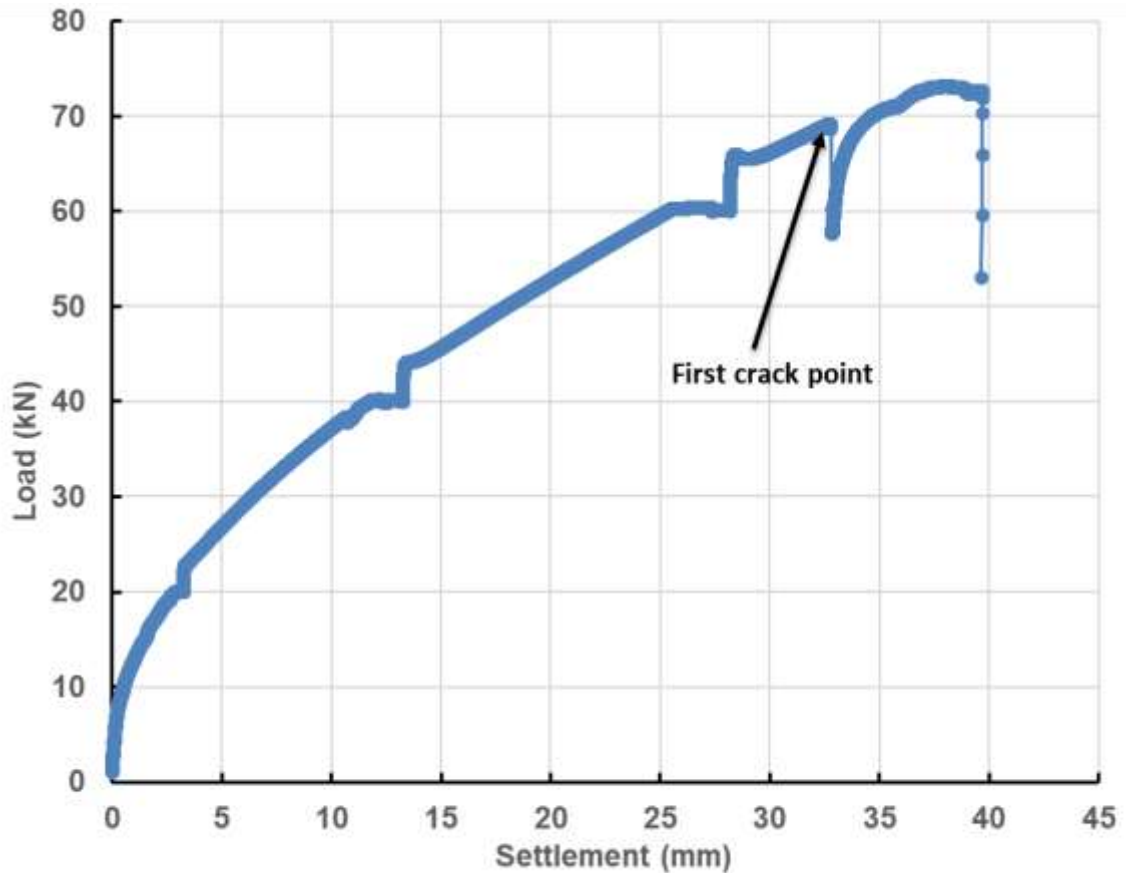


Figure 4.3: Load Vs Settlement Curve Results for GFRP - 1 Slab Specimen

There was a reduction in the stress imposed on the slab, upon cracking the load dipped from 69.141 kN to 57.593 kN and the Strain values experienced a steep downfall as the concrete swapped to its plastic state. The compression section of the slab had a strain of -26.37 (SG1), and -33.04 (SG2), and the tension slab section had a strain of 41.58 (SG3), and 45.74 (SG4) at cracking load. The loading valve was left undisturbed until the hydraulic actuator regained the load sequentially after the crack with the help of existing oil pressure. The load value ended up oscillating between 72.60 to 73.10 kN.

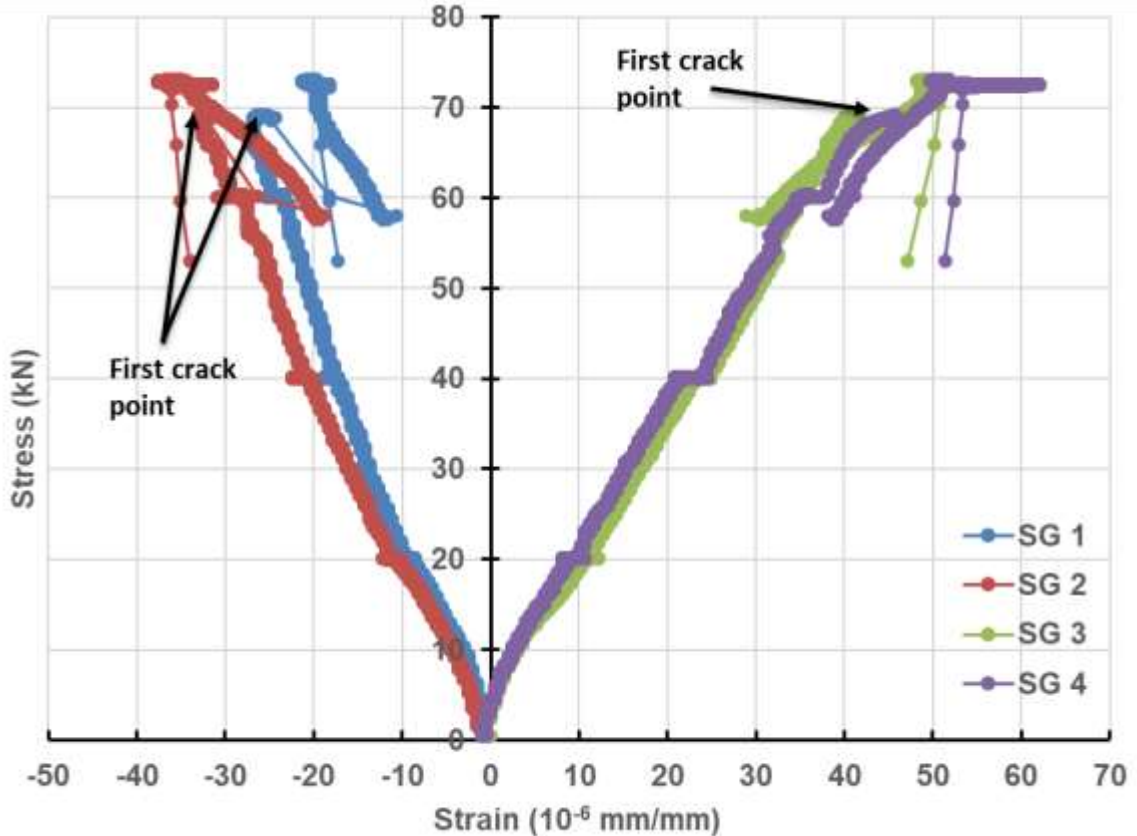
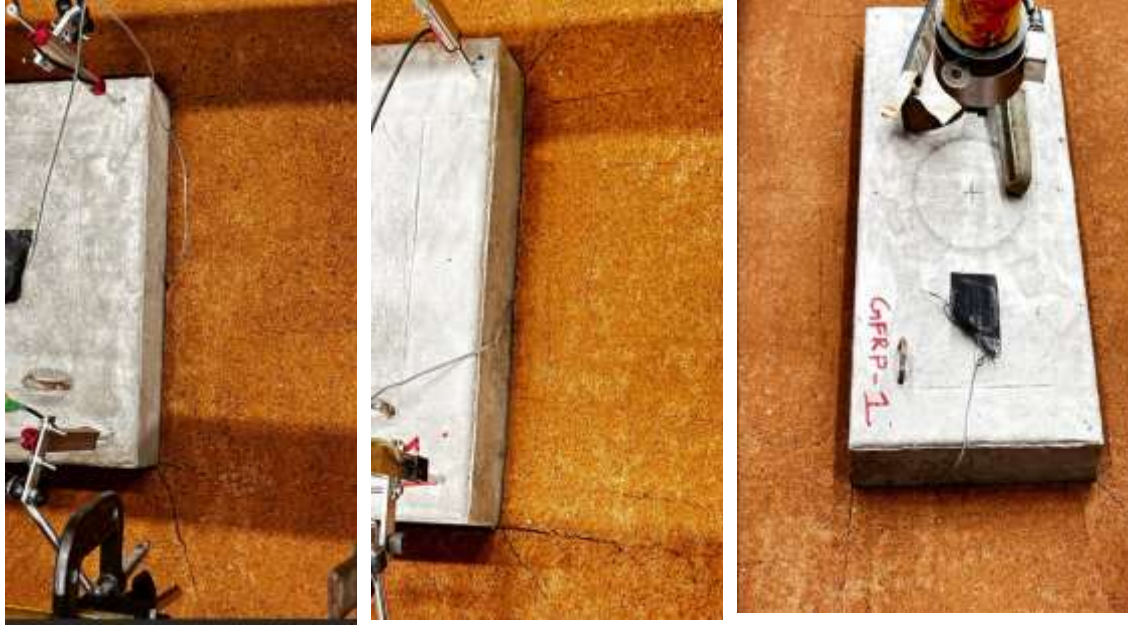


Figure 4.4: Stress-Strain Curve of GFRP-1 Slab

The flexural crack width was 1.25 mm on both sides of the slab. As the crack prolonged to the compressive part of the slab the crack width dropped to 0.4 to 0.5 mm. It took 11 settlement inspection cycles to obtain the 0.03mm/min criteria. The soil settled at 37.688 mm during the initial inspection and dipped to 38.936 mm for the last inspection. By the end of the settlement inspection analysis, the slab had a maximum strain value of 52.241(SG 3) and 62.012(SG4) on the Tension side, while the compression side experienced lesser strain values after the crack (-26.371 and -37.618). Since the slab attained both cracking loads and settled around 40 mm, the test was terminated by releasing the stress imposed on the slab utilizing the load control valve.



(A)



(B)

Figure 4.5: (A) Soil Crack at Sections A-A1, B-B1, and Lateral Cracks

(B) Flexural and Tension Cracks Of GFRP-1 Slab

4.3.2 Subgrade Response of 10%-TDA-GFRP-2 Slab

Before imposing the slab on top of the soil, the top three layers of the soil subgrade were disturbed and compacted again based on the same compaction method. The soil subgrade had an overall relative density of 49.82%. The 10%-TDA-GFRP-2 slab specimen was positioned in the middle of the soil tank and all 6 LVDTs were placed in position, the strain gauge and the LVDTs were connected to the data acquisition system. The Load was incremented from 0 kN to 20 kN manually using the load control valve, once the 20 kN load interval was attained, the loading rate was actuated to maintain the load oscillating around 20 kN to 20.2 kN. It can be observed from Figure 4.6 that the soil body exhibited a very stiff behavior and the slab had only settled to about 1.9 to 2.1 mm. The in-situ soil settlement analysis was done and the required settlement difference of 0.03mm/min was attained at the 5th inspection cycle. There was no crack in the concrete and the soil did not generate any fractures on the soil surface at this load interval. The average soil settlement was 1.94 mm in the initial evaluation and the soil body embedded down to 2.09 mm. The concrete slab had a strain value of -18.238 (SG1), -13.232 (SG2) on the compression side, 16.224 (SG3), and 14.731 (SG4) on the tension side.

The load control valve was then rotated clockwise to infuse oil into the hydraulic actuator to increase the load from 20 kN to 40 kN. The slab and the soil surface were investigated during the load incrementation process. The slab had uniform settlement as the load crept up to 40 kN, and the strain experienced by the concrete slab escalated double the times of 20 kN respectively. At 38 kN, the soil stress distribution pattern started to overlap each other causing the soil to expose the stress by developing a surface fissure at all four corners. The corner split crack at section A-A' was measured to be 11.2 mm and 10.6 mm long.

Section B-B' had a two-way split crack at B each measuring (12.1mm and 11.7 mm) and at B' it was 12.4 mm. As the actuator reached 40 kN, the slab had an average settlement of 9.116 mm. The actuator was set to oscillate at a load of 40 kN and the settlement of the slab was recorded manually for all the LVDTs at every 3-minute interval, this analysis was continued for 10 repetitive cycles to attain the desired 0.03 mm/min settlement. In the initial cycle, the slab had driven through the soil to a depth of 9.22 mm from the top surface. By the 10th cycle, the slab settled to 9.84 mm. The strain obtained on the compressive side of the slab was at -40.021 (SG1) and -28.499 (SG2), while the tension side of the slab generated strain values of 35.491 (SG3) and 33.527 (SG4).

The load was then increased gradually with the load control value to 60 kN, the slab was constantly viewed and recorded visually to determine the concrete yielding point. The 10%-TDA-GFRP-2 slab peaked to its maximum strain at a load of 51.0922 kN and the slab developed flexural cracks on the tension side of the slab, which eventually prolonged to the longer side of the slab surpassed the neutral axis of the slab. This flexural crack made the slab tilt concave towards the central point load, which depreciated the load to 43.29 kN and diminished the strain exerted on the slab. The hydraulic pump was left to catch up to the load imposed before the crack, and the actuator oscillated around 57.7 to 57.8 kN. Beyond that load control value was utilized to manure the load to 60 kN point. The concrete slab had a strain value of -44.58 (SG1), and -32.061(SG2) from the section above the rebars, and the tension concrete section had a value of 41.06 (SG3) and 41.655 (SG4) while the concrete slab yielded its plastic state. The flexural crack had a width of 0.75 mm below the neutral axis (Tension section) as it went above the neutral axis the crack contracted to a width of 0.5 mm on both sides of the slab.

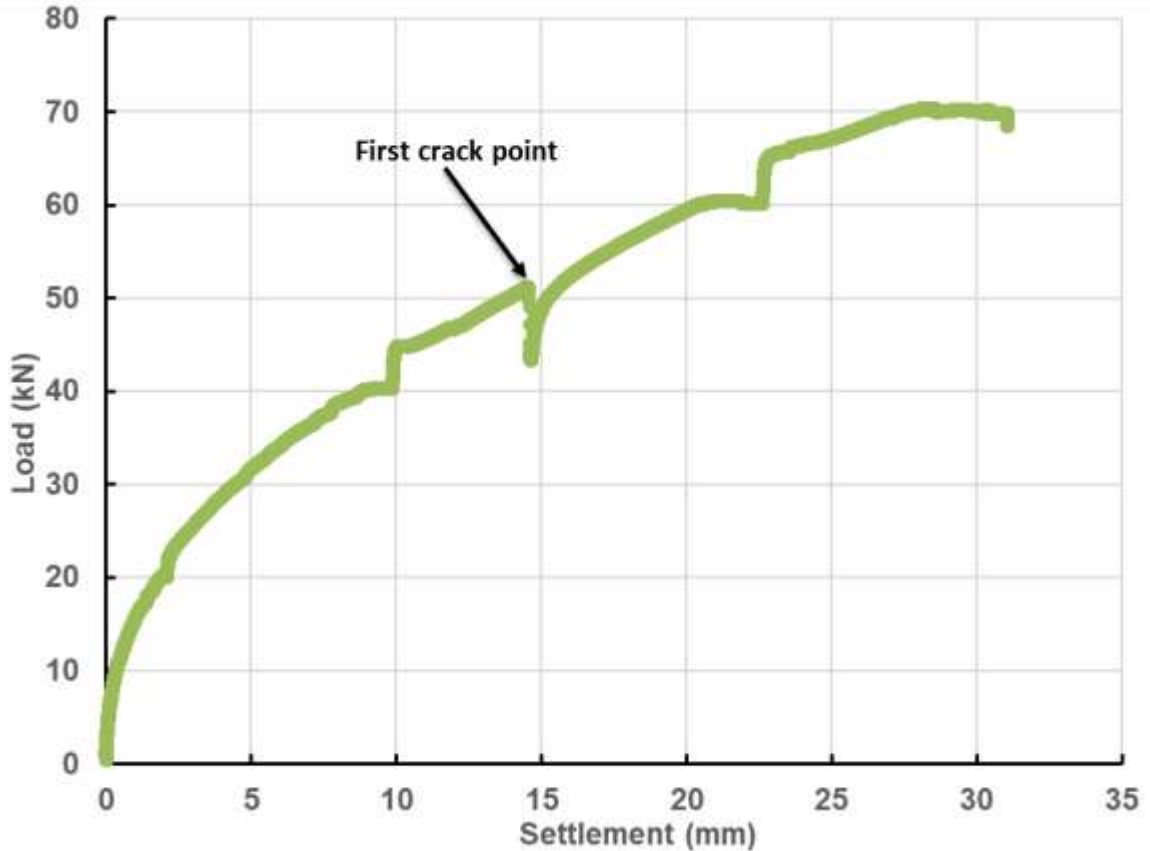


Figure 4.6: Load Vs Settlement Curve of 10%-TDA-GFRP-2 Slab Specimen

At 60 kN the slab had dilated the soil subgrade to a depth of 20.557 mm. It took 11 cycles of cross-verifications to attain the desired difference of 0.03 mm/min at 3-minute intervals for each LVDT. In the First cycle, the slab had displaced 22.079 mm of soil and in the last cycle, the slab had sunk to a depth of 22.567 mm. At 60 kN analysis, the strain value changed drastically. From the strain data, it can be analyzed that the strain on the compressive part dropped down to -29.383(SG1), and -23.919 (SG2), while in the tension part of the slab, it drastically aggravated to 57.294 (SG3) and 60.959 (SG4). This exposes the behavior of 10%-TDA reinforced concrete.

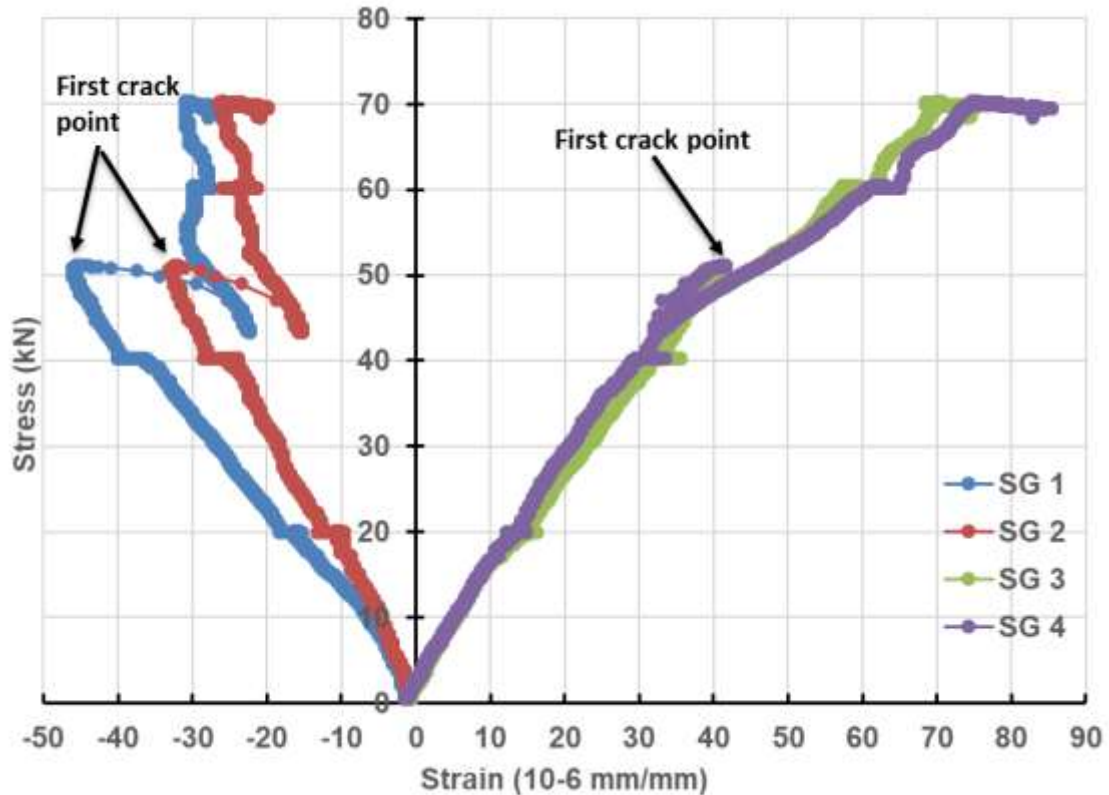


Figure 4.7: Stress-Strain Curve of 10%-TDA-GFRP-2 Slab

Since the slab had already settled to 22 mm of depth, the desired settlement required for the slab was 25 to 30 mm. Hence, the load incrementation was shifted to 70 kN instead of 80 kN. As the load was incremented the slab attained 25 mm of settlement at 67.1338 kN and as the load inclined to 70 kN the soil was exposed to its passive state making the soil deform 29.692 mm. It took 15 iterations to attain the 0.03 mm/min of settlement. The soil had submerged down to 30.510 mm by the last iterative analysis. The concrete slab did not develop any further crack, the present flexural crack had elongated wider and was at 1 mm width at the tensile zone. The crack width reduced above the neutral axis, it curtailed to 0.75 mm on both sides of the slab. The strain value augmented on the tension side due to the flexural crack, the strain on both sides of the crack on the tension side were 69.971 (SG3) and 74.676 (SG4). Concrete above the neutral axis had a strain value oscillating at -

30.902 (SG1) and -25.954 (SG2). The Strain values were escalating vigorously on the tension side during the load interval, hence by the end of the settlement analysis the slab had a strain value of 74.534 (SG3) and 82.805 (SG4) on the tension zone. Figure 4.6 exemplifies the soil stiffness regains at each settlement inspection phase, as the load is held at a certain value for a long period. Eventually, this process enhances the soil stiffness and makes the soil effective to withstand 4 to 5 more kN of load at the same settlement value for each load incrementation process. The soil surface cracks at the corner of the slab developed further and diverged into several cracks, The initial soil crack width increased to 4 mm, and it developed three cracks vertically to the short span of the slab on both sides. The slab had more surface area in the longer span, causing it to exert more pressure. Hence the soil had longitudinal cracks running parallel to the longer span of the slab, disturbing the soil body, and causing it to heave towards the slab. The test was terminated as all the required outcomes were attained.





(A)



(B)

Figure 4.8: (A) Soil Crack at Sections A-A1, B-B1, and Lateral Cracks

(B) Flexural Cracks Of 10%-TDA-GFRP-2 Slab

4.3.3 Subgrade Response of 20%-TDA-GFRP-1 Slab

Once all the top 1/3 depth of soil is disturbed and reinstated into the soil tank. Each layers were subjected to an in-situ soil test to evaluate the RD value. The soil subgrade had an average relative density of 50.28%. The 20%-TDA-GFRP-1 slab specimen was prepared for testing. The slab was then imposed on top of the prepared soil. All the LVDTs and strain gauges were mounted and connected to the data acquisition system. The Load was imposed and inclined to 20 kN with the help of the load control valve. At 20 kN load interval, the

soil was inspected for the optimum settlement of 0.03mm/min for every 3 min interval. The soil exhibited an extremely stiff behavior during the 20 kN investigation period. The elasticity of the soil withheld the slab efficiently exerting very little settlement of 0.872 mm to 0.971 mm throughout the load investigation period. As the soil displayed stiffer characteristics, it took just 4 iterations to obtain 0.03mm/min of settlement. The soil did not generate any surface fractures at this load concerning the slab's surface area. The 20%-TDA-GFRP-1 slab did not generate any flexural or shear cracks which exemplifies the shear behavior of this slab. The imposed load had provoked the strain value to -19.279 (SG1) and -11.694 (SG2) on the compression zone, the tension zone experienced a strain value of 17.778 (SG3) and 15.742 (SG4).

The load was manually escalated to 40 kN by increasing the oil pressure exerted by the pump. From Figure 4.9 it can be viewed that the load inclination to the soil settlement pattern has shifted to a steep pattern which emphasizes that the soil subgrade had transmitted from an elastic to a plastic state. The soil lost its stiffness and yielded at a load of 36 to 37 kN instigating shear cracks on the soil surface at all four corners of the slab. As the soil shifted to its plastic state it experienced a sudden settlement of 8.407 mm over the previous settlement of 0.97 mm. The cracks were 9.3 mm and 8.8 mm long at corners A and A', while the shear crack at corner B had a split crack of 11.7 mm and 6.8 mm and a slim crack at B' of 7.4 mm. The concrete slab exhibited prominent flexural behavior and maintained its state as elastic. Concrete slab under the influence of 40 kN load effectuated a significantly higher strain value of -42.109 (SG1) and -24.913 (SG2) on the compression zone, the concrete in the tension zone displayed a strain value of 37.588 (SG3) and 31.992 (SG4). It took 10 settlement inspection iterations for the soil to attain the 0.03mm/min

settlement rate per 3 mins. In the first iteration, the slab had sunk 9.382 mm into the subgrade, at the last analysis it ended up at 9.964 mm beneath the top surface.

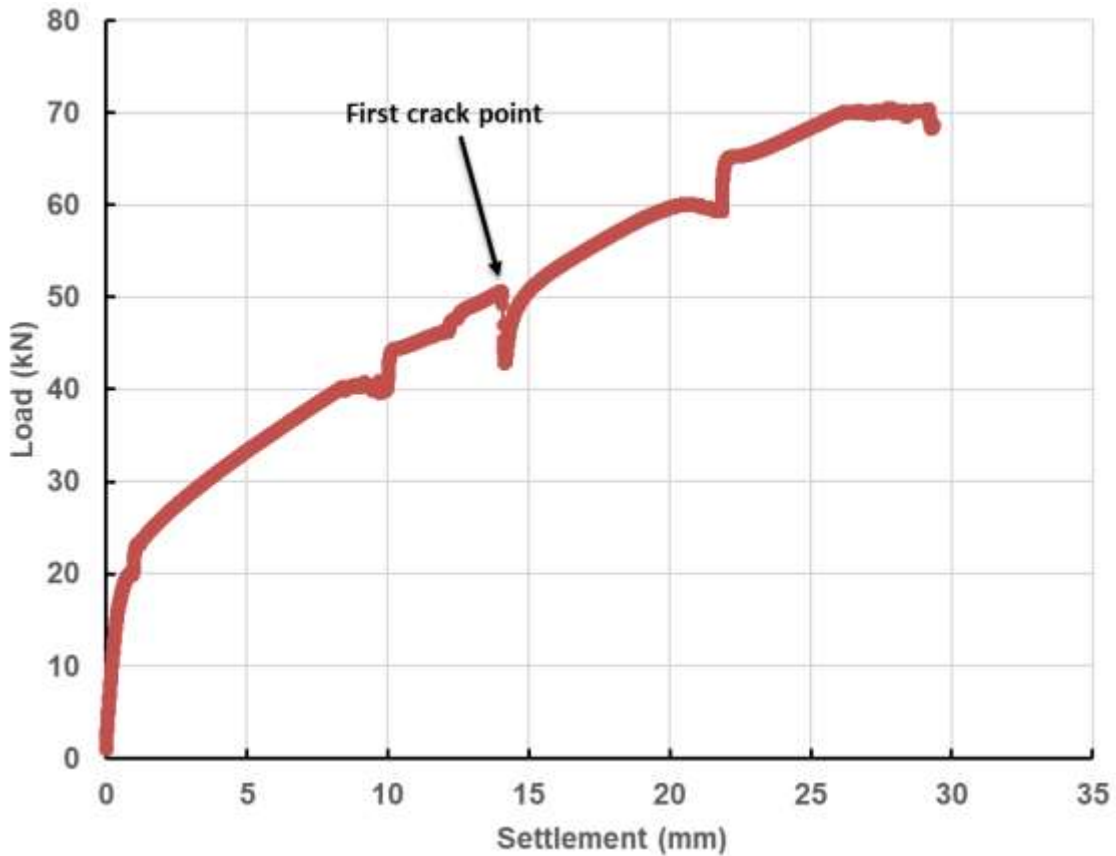


Figure4.9: Load Vs Settlement Curve of 20%-TDA-GFRP-1 Slab Specimen

The load was proliferated to 60 kN manually utilizing the load control valve. The Slab and the soil surface were visually monitored during the load inclination process. There was a steep inclination of load from 40 to 44 kN as the soil gained considerable stiffness during the previous load inspection cycle, thus sustaining the slab around 10 to 10.2 mm of settlement till 44 kN. Beyond 44 kN the soil exhibited a plastic-bearing effect. In Figure 4.9 it can be seen that there is a sudden heap of load in the middle of the load incrementation around 46 to 48 kN caused due to the change in oil pressure imposed by the pump. During

this loading process, the 20%-TDA concrete exerted a notable increase in its strain value as the stress inflates up.

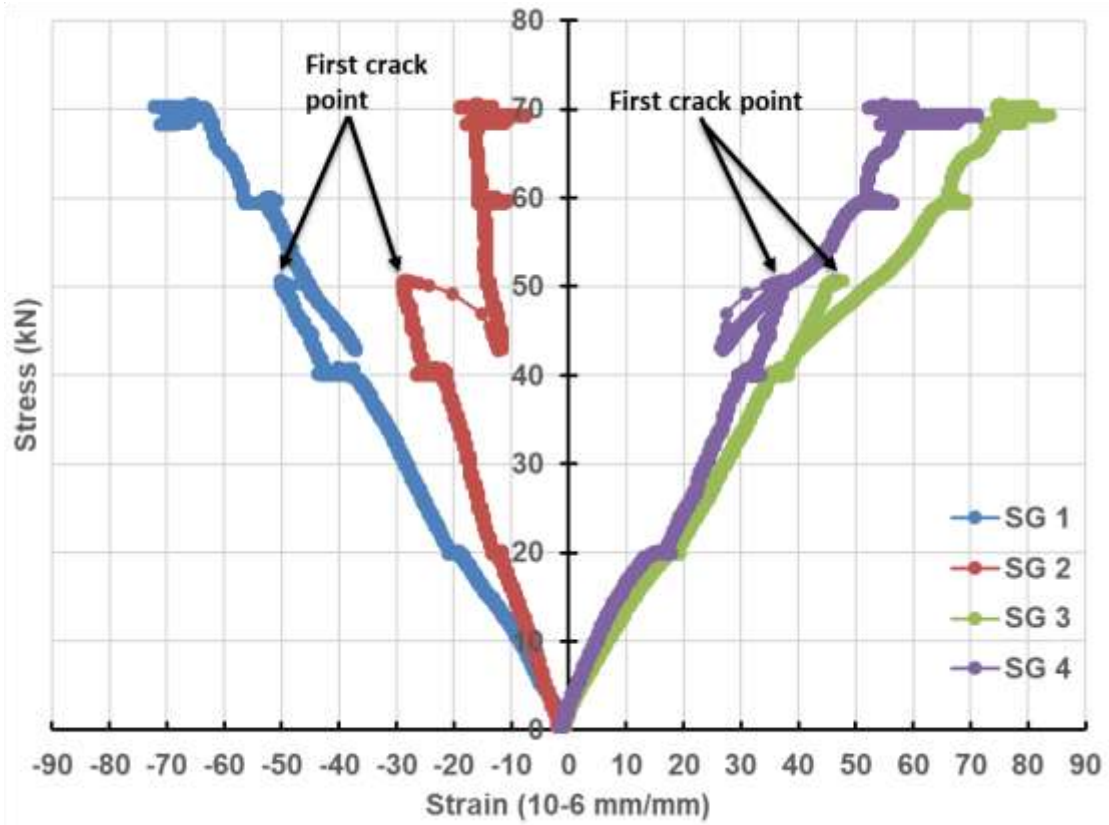


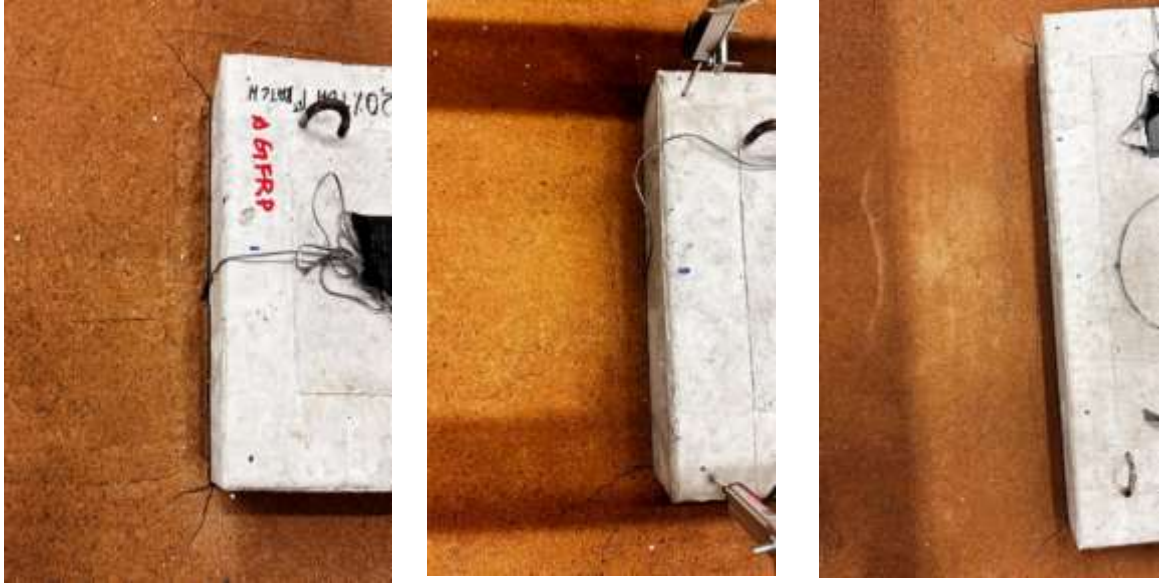
Figure 4.10: Stress-Strain Curve of 20%-TDA-GFRP-1 Slab

At 50.591 kN load, the strain in the slab attained its threshold value causing the concrete to deform and induce flexural cracks in the tension zone which elongated on both long-span sides. The 20%-TDA concrete deformed at a peak strain value of -50.226 (SG1) and -28.472 (SG2) in the compressive zone, and the tension zone produced a strain of 47.748 (SG3) and 37.071 (SG4). The load acting on the concrete dropped off to 42.908 kN due to its deformation and gradually the oil pressure in the actuator increased the load to 52.335 kN, beyond which the load control valve was used to augment the load to the 60 kN mark. The cracks were 0.75 mm wide in the tension zone and the crack width declined to 0.4 mm as it went above the neutral axis on both longer spans of the slab. The Slab had settled to a

depth of 20.8 mm once the stress value reached 60 kN. Under the influence of flexural crack and soil subgrade settlement, the slab has settled an additional 11.007 mm during the 60 kN incrementation phase. At the first iteration for 0.03mm/min per 3-minute interval, the slab was 20.972 mm below the surface level. 10 iterations were required to obtain the essential settlement rate. By the last iteration, the slab went down to 21.839 mm average settlement. The stress-induced flexural crack made the slab tilt inward enabling the middle LVDTs to undergo more settlement than the corner ones. The Middle LVDTs was at 23.5 mm and the corner ones varied between 20.5 to 21.2 mm. The soil matured further by developing parallel cracks beside all four sides of the slab. These cracks indicate that the soil body has begun to fail and is converging toward the point load on top of the slab. In Figure 4.9 at a 60 kN load interval, there was a drop in the load from 60.097 kN to 59.352 kN caused due to soil failure. The soil exposed a plastic behavior and had less heaving of the topsoil surface. The strain experienced by the concrete during the settlement inspection phase was -51.748 (SG1) and -13.219 (SG2) in the compression zone and 66.543 (SG3) and 52.306 (SG4) at the tension zone during the first settlement inspection cycle. Concerning the load drop, the strain value reduced on the tension side to 66.035 (SG3) and 51.798 (SG4), while the compression zone gained more strain at -56.314 (SG1) and -15.761 (SG2). The soil corner crack width has widened to 2 mm and the lengths vary around 93 to 97 mm on both sections. Several fissure soil cracks were formed perpendicular to the short and long span of the slab specimen.

Since the slab had already settled to 21.8 mm approximately, the load was incremented to 70 kN to attain 25 mm of settlement. In Figure 4.9 it can be observed that the initial 60 to 65 kN load increment went vertical with a very minimal amount of settlement. This exposes

that the soil had gained a substantial amount of stiffness to hold the slab around 23.1 mm. Surpassing the 65 kN the slab started to push through the soil stiffness transferring the soil to its plastic state. The Slab hit 25 mm of settlement at a load of 68.37 kN. At 70.193 kN both the middle LVDTs attained 30 mm of settlement. The concrete experienced a maximum strain value of -72.04 (SG1) and -18.812 (SG2) on the compressive side, while the tension side had 80.768 (SG3) and 59.924 (SG4) post-cracking. The Strain evolving around the crack enhanced its width at the tension zone to 1.25 mm, at the middle (neutral axis) it was 1 mm and as it went above it came down to 0.75 to 0.5 mm wide on both sides of the slab. As the subgrade manifested failure on the previous load interval, the failure pattern developed further by stimulating the soil pressure into the passive zone. As the load distribution pressure was greater than the surface surcharge pressure the soil began to bulge and pile up in an elliptical shape surrounding the slab specimen. The soil surface heaved out in a wavy manner. The soil had several thin cracks running perpendicular to the slab's long and short spans. The overall soil settlement was at 28.122 mm for the first iteration, Throughout the inspection phase the soil settled, by the last iteration the soil yielded a settlement of 29.179 mm. It took 15 iterations to procure 0.03 mm/min settlement for 3 consecutive intervals. The test was terminated by releasing the load imposed with the help of the load control valve.



(A)



(B)

**Figure 4.11: (A) Soil Crack At Sections A-A1, B-B1, and Lateral Cracks
(B) Flexural Cracks Of 20%-TDA-GFRP-1 Slab**

4.3.4 Non-geocell Subgrade Response Comparison between Slab Specimens

Figure 4.12 brings forth the comparison between GFRP-1, 10%-TDA-GFRP-2, and 20%-TDA-GFRP-1 slab specimens tested on top of an unreinforced sandy soil subgrade. The relative density of the soil body utilized for the three slab tests varied between 48.6% to 50.3%. The subgrade utilized for the 20%-TDA-GFRP-1 slab exhibited a comparatively stiffer soil surface behavior at the initial phase of the testing, at 20 kN load the slab had settled to 0.97 mm, whereas the 10%-TDA-GFRP-2 and GFRP-1 slab settled to a depth of 2.1 mm and 3.23 mm corresponding to the specimens. The cause of such settlement could be due to higher friction between soil particles, and the reduction of slab weight for 10% and 20% TDA-reinforced concrete slab. The 20%-TDA-GFRP-1 Slab had a significantly higher amount of strain acting in the concrete. The 10%-TDA-GFRP-2 slab had a strain value greater than the GFRP-1 slab, and lower than the 20%-TDA slab. The strain values are mentioned in Table 4.2.

The settlement of all three slabs increased drastically during the 40 kN loading phase, and the soil was exposed to a plastic state. The soil with RD 50.28% was greater in stiffness till 36 kN, beyond which the soil yielded to its plastic state generating cracks at the corner. Resembling that soil performance the other two subgrades as well yielded around 35 to 38 kN boundary. Thus, all three subgrades were exposing plastic response. At 40 kN load-interval, both 10%-TDA-GFRP-2 and 20%-TDA-GFRP-1 slab have penetrated the soil to a depth of 9.84 mm and 9.96 mm. Whereas the GFRP-1 slab has submerged 13.17 mm deep into the subgrade.

As all three soil bodies had almost similar RD values, excessive settlement of the GFRP-1 slab happened due to its excessive weight, uniform deformation into the soil body, and less

bending movement as it has lesser strain acting in the concrete. While the 10%-TDA-GFRP-2 and 20%-TDA-GFRP-1 slab had a higher strain value at 40 kN load exemplifying that these slabs had experienced significantly higher bending movement than the GFRP-1 slab. This is caused due to the addition of TDA in the concrete slab, which enforces these slabs to have a flexible settlement. The GFRP-1 slab has 66.585% and 62.943% less strain value on the compressive zone than the 10%-TDA-GFRP and 20%-TDA-GFRP-1 slab specimens. On the tension zone, the GFRP -1 slab has 40.14% and 41.14% lesser strain value than the 10% and 20% TDA slab specimens. All three soils demonstrated an extensively stiffer behavior at the initial loading phase, and all three slabs were sustained at the same settled value with a negligible advancement of 0.1 to 0.2 mm. This was experienced as the subgrade was left to deform under the same load for more than 30 minutes which enhanced the stiffness of the soil, eventually allowing the soil to endure up to 44 to 45 kN. Certainly above 45 kN, the soil reverts to its plastic state enhancing further soil deformation as the pressure increases. The GFRP-1 slab exhibited an elastic response throughout the loading phase, and the concrete had a strain value of 28.228 in the compressive zone and 36.8115 in the tension zone. The slab had attained the 25 mm deformation at a load of 59.524 kN and by the end of the settlement inspection phase, the slab had sunk 28.133 mm at 60 kN.

In contrast, the 10%-TDA-GFRP-2 and 20%-TDA-GFRP-1 slab response varied in terms of the slab and deformation of the soil. Both slab specimens manifested akin results in terms of the load-settlement curve. Both concrete slabs had higher bending movement and flexibility, and both slabs yielded during the 60 kN loading phase. The 10%-TDA-GFRP-2 slab yielded to its plastic state by generating flexural cracks at a load of 51.092 kN. This

slab encountered a substantial strain value of 41.457@ tension zone and 38.32@ compressive zone. While the 20%-TDA-GFRP-1 slab exerted a homogeneous result with a marginally comparable value in terms of cracking load, strain value, and soil deformation.

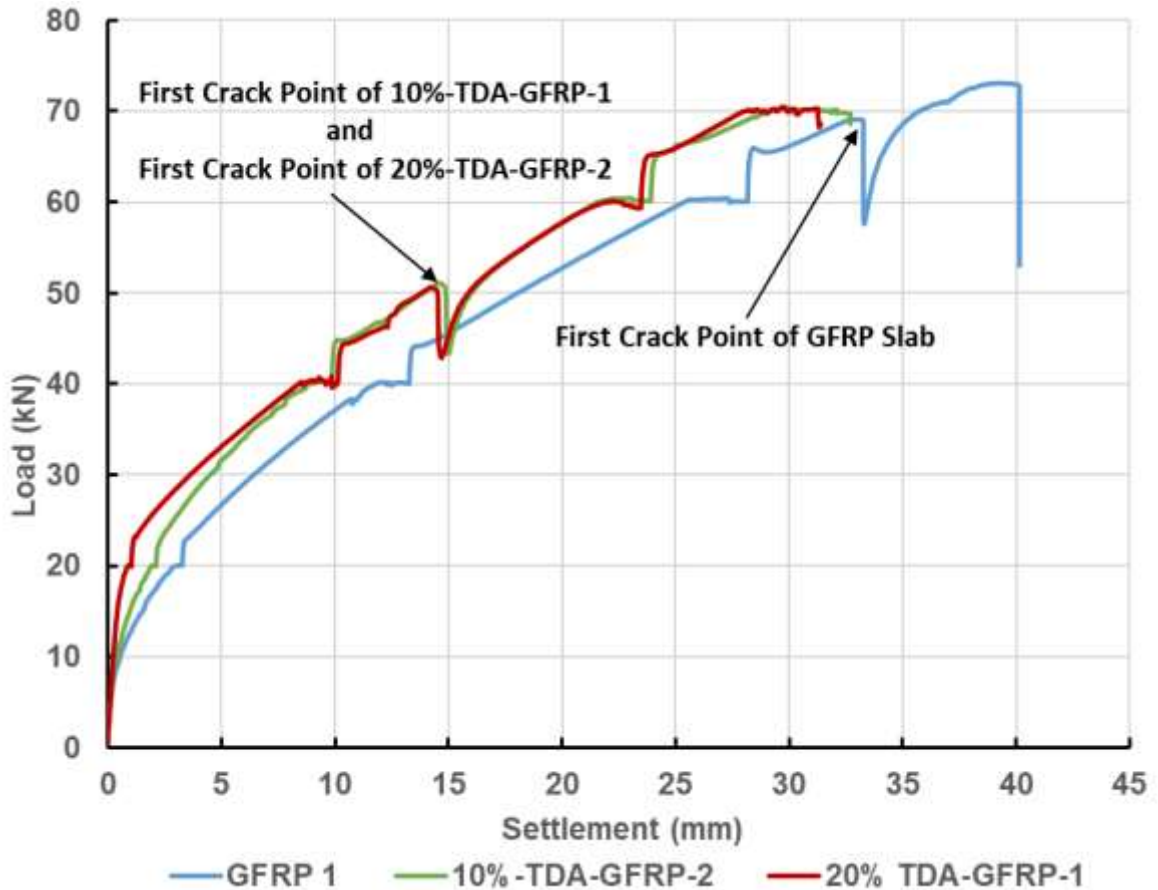


Figure 4.12: Monotonic Load Test Comparison on Non-Geocell Sandy Soil

The 20%-TDA-GFRP-1 slab transmitted to its plastic state yielding a flexural crack at 50.591 kN slightly lower than the 10% TDA slab. The concrete detriment at a peak strain value of 42.4095@ tension zone and 39.349@ compressive zone. Both slabs exposed elongated flexural cracks on the longer span, it was measured to be 0.75 mm on the tension zone, and as it elongated above the neutral axis the crack width reduced to 0.4 mm. In contrast to the GFRP-1 specimen, the soil deformed to 22.567 mm for the 10% TDA specimen and 21.839 mm for the 20% TDA specimen. The GFRP-1 specimen had settled

24.66% and 28.82% respectively more than the 10% and 20% TDA-GFRP slab specimens at the 60 kN load interval.

Similar to all other loading phases, the initial stiff soil behavior was observed in all three soil conditions. GFRP-1 slab was pushed further beyond 28 mm of settlement to determine the ideal cracking point of the normal concrete GFRP reinforced specimen. As the GFRP-1 specimen was experiencing a higher strain value at the 60 kN interval, the concrete slab developed a flexural crack with a loud cracking sound exemplifying the brittle behavior of normal concrete. Certainly, the TDA reinforced slab yielded a crack without any cracking sound proclaiming the ductility of these slabs. Thus, the GFRP-1 slab yielded to its plastic state at 69.141 kN, and a huge drop in load was experienced due to the deflection of the slab. The load went down to 57.593 kN and the actuator eventually caught up to 72.6 kN. It is evident through Figure 4.12 that the slabs with 10% TDA and 20% TDA yielded at their certain loads, which were 26.104% and 26.829% drastically lower than the GFRP-1 slab. GFRP-1 slab had a strain value of 43.645@ tension zone and 29.705@ compressive zone while the crack developed. The GFRP-1 slab sunk into the soil to a depth of 40.152 mm by the end of the settlement inspection phase.

From Table 4.2 it is evident that the strain values on the tension side were comparatively similar with both TDA-reinforced GFRP slab specimens. 10% and 20% TDA-reinforced slabs were both subjected to 70 kN load incrementation to attain the 30 mm settlement. From Figure 4.12 it is evident that the 10%-TDA-GFRP-2 slab attained 25 mm of settlement at 67.1338 kN and the soil experienced a sudden deformation to 29.692 mm at 70 kN forcing the soil to develop passive zones surrounding the specimens. Likewise, the 20%-TDA-GFRP-1 specimen procured an average of 25 mm of settlement at 68.37 kN,

and at 70 kN the slab submerged to 26.341 mm. Post-cracking, the 20%-TDA-GFRP-1 concrete slab on the tension zone had 80.768 (SG3) and 59.924 (SG4) strain values. By the end of the settlement inspection phase, the middle LVDTs had settled 32.681 mm beneath the ground level. The 10%-TDA-GFRP-2 slab ended up at 31.269 m sunk into the soil surface. At the same time, strain readings on the tension zone intensified significantly over the load interval, resulting in a value of 74.534 (SG3) and 82.805 (SG4) at the end of the settlement inspection. All three tests depicted the same soil failure pattern by the end of the test. The soil top surface was converging in a concave pattern towards the slab, the soil surface had several shear cracks at the corner of the slab, heaving of the top surface of the soil due to the passive behavior, soil cracks running perpendicular to both shorter and longer spans for all the three slabs, and longitudinal cracks running parallel to the longer span of the slab. Irrespective of the slab type and type of settlement exerted on the soil by the slab, the non-geocell sandy soil subgrade exposed corresponding crack patterns.

Table 4.2: Non-Geocell Sandy Soil Result Comparison

TEST RESULTS		Slab Type		
		GFRP-1	10%-TDA- GFRP-2	20%-TDA- GFRP-1
R.D of Soil		48.69%	49.82%	50.28%
Bearing Capacity (kN/m ²)		228.37	219.83	220.30
Soil Crack Type		Passive crack	Passive crack	Passive crack
F'c (kN/m ²)		42.63	27.32	21.95
P _{cr1} (kN)		69.14	51.09	50.59
Δ _{cr1} (mm)		1.25	1	1.25
Strain @20 kN	Compression Zone	-11.172	-15.735	-17.01
	Tension Zone	11.423	15.477	18.537
Strain @40 kN	Compression Zone	-20.566	-34.26	-35.034
	Tension Zone	24.624	34.509	35.806
Strain @60 kN	Compression Zone	-28.183	-27.921	-36.037
	Tension Zone	36.811	63.441	62.726
Strain @70 kN	Compression Zone	-31.994	-28.428	-45.426
	Tension Zone	57.126	80.193	70.346

4.4 Conclusion

This chapter deliberately presents the results of several laboratory tests conducted in the soil tank. It comprises different test results such as a comparison of plate load tests on normal and geocell-reinforced soil, monotonic load tests on GFRP-1, 10%-TDA-GFRP-2,

and 20%-TDA-GFRP-1 slab specimens on normal soil with 50% RD, Comparison between the soil response due to the monotonic load test done on these three slab specimens.

1. The geocell reinforced showed prominent improvements in the load vs settlement rate, the load vs settlement curve of geocell reinforced soil was predominantly linear as the soil was sustained in its elastic state, compared to the normal soil (NS) which transitioned to its plastic state at a load of 2.50 kN @ 3mm settlement. The geocell-reinforced soil did not have any passive effect in it and the cracks were reduced by 95%. Whereas the NS produced several shear cracks bifurcating the subgrade's top surface diverging away all around the circumference of the bearing plate. The geocell-reinforcement enhanced the load-bearing capacity of the soil by 38.97% more than the normal soil. Therefore, the Geocell has enhanced the stiffness, elasticity, loading capacity, bearing capacity of soil and augment the uniform stress distribution pattern in the soil stratum.
2. Irrespective of the slab type and type of settlement exerted on the soil by the slab, the non-geocell sandy soil subgrade exposed corresponding crack patterns. The subgrade top surface was converging in a concave pattern towards the slab, the soil surface had several cracks such as shear cracks at the corner of the slab, heaving of the top surface soil due to the passive behavior, soil cracks running perpendicular to the shorter span and longer span for all the three slab specimens, and longitudinal cracks running parallel to the longer span of the slab. The 10% and 20%-TDA-GFRP slabs cracked around 50 to 51 kN load, the 10%-TDA-GFRP-2 slab experienced a flexural crack at 26.10% lesser load and 20%-TDA-GFRP-1 slab cracked at load which is 26.82% lesser than GFRP-1 Slab which had a cracking

load of 69.141 kN. The strain on the tension zone of the 10%-TDA-GFRP-2 and 20%-TDA-GFPR-1 slab was 28.764 % and 18.792% greater than the GFRP-1 slab at 70 kN.

CHAPTER-5 FIELD DATA VALIDATION USING PLAXIS 3D FEA SOFTWARE

5.1 Introduction

In this research, the experimental monotonic load test on a slab-on-grade arrangement was rigorously modeled using Finite Element (FE) analysis Plaxis 3D software. Six different soil subgrade properties were generated based on different relative densities of the soil using the empirical formula to correlate the hardening soil small strain (HS small) model parameter. The designed models were thoroughly evaluated to generate significant FE analysis results for different soil parameters derived from varied relative density values. The model results obtained utilizing Plaxis 3D FEA software were used to compare and numerically validate the Load vs Settlement curve results, and evaluate the behavior of sandy soil under different relative density values, which were obtained through experimental analysis in the laboratory.

5.1.1 Finite Element Soil Model Development

Soils and rocks can be modeled with different levels of precision to study their mechanical behavior. The linear elastic perfectly plastic model, known as the Mohr-Coulomb model, operates as an initial approximation for soil or rock behavior, encapsulating fundamental characteristics. However, PLAXIS offers a broader spectrum of advanced material models that encompass various intricate features. These models go beyond the simplistic linear elastic perfectly plastic approach, incorporating distinct aspects such as stress-dependent stiffness, strain hardening or softening, a memory of pre-consolidation, critical state behavior, anisotropic properties, creep phenomenon, swelling, and shrinkage behaviors. By incorporating these advanced models, PLAXIS provides a more comprehensive

understanding of the complex mechanical responses exhibited by soils and rocks under different loading conditions.

In this study, the soil subgrade has been defined as a hardening soil small strain model. The hardening soil model is an advanced soil model utilized to simulate the behavior of soil. Analogous to the Mohr-Coulomb model, this model also employs strength parameters such as the dilatancy angle (ψ), friction angle (ϕ), and cohesion (c) to define the stress limits. Yet, when it comes to specifying soil stiffness more precisely, it comprises four distinct stiffness measures: Secant stiffness in standard drained triaxial test (E_{50}^{ref}), Tangent stiffness for primary oedometer loading (E_{oed}^{ref}), Unloading/reloading stiffness from the drained triaxial test (E_{ur}^{ref}), and Power for a stress-level dependency of stiffness (m). The Hardening Soil model differs from the Mohr-Coulomb model as it incorporates stress-dependent stiffness moduli. This means that the value of stiffness increases in proportion to the pressure. The original hardening soil model was modified and improved to create a new hardening soil with a small strain (HSs) version to account for the increased stiffness of soils at low strain levels. Soil frequently exhibits non-linear variations in stiffness with strain, and they are stiffer at lower strain levels relative to engineering circumstances. To accurately capture the behavior, the HSs model incorporates an extra strain-history property, which allows it to handle this problem. Two additional material small strain parameters were incorporated: G_0^{ref} and $\gamma_{0.7}$. G_0^{ref} signifies the shear modulus at low levels of strain, $\gamma_{0.7}$ indicates the strain level at which the secant shear modulus (G_s) declines to approximately 70% of the shear modulus (G_0) at small strains. Specifically, the model outperforms the HS model in terms of its accuracy of displacement predictions.

Additionally, the hardening soil model incorporates material damping with hysteresis when used in dynamic conditions, together with the small-strain stiffness.

It was originally assumed in the hardening soil model that soil acts elastically when imposed to loading and unloading of stress. However, in reality, soils only show truly elastic behavior within a very narrow range of strain. As the strain increases, the stiffness of the soil decreases nonlinearly. Hence, soil stiffness decreases subtly over time, as illustrated by characteristic curves plotted against the logarithm of strain. Figure 5.1 depicts the characteristic stiffness-strain behavior of soil with typical strain ranges for laboratory tests and structures.

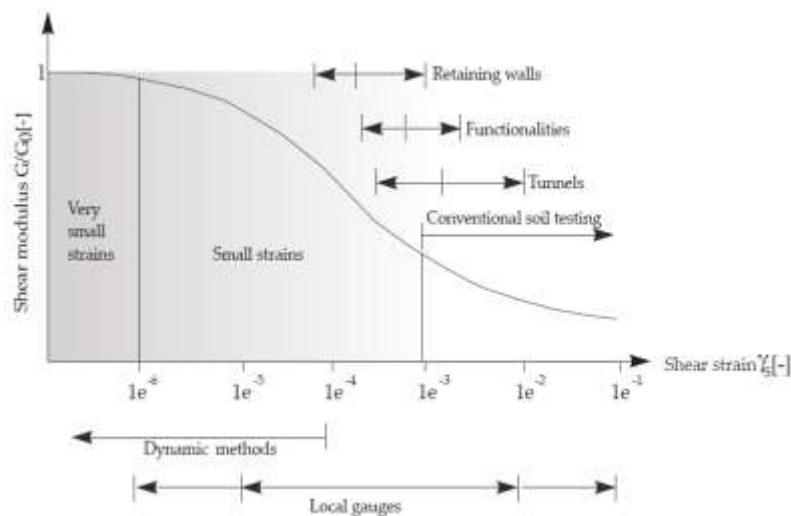


Figure 5.1: Characteristic Stiffness-Strain Behavior of Soil with Typical Strain Ranges

Both the conventional hardening soil model and the model that incorporates small-strain stiffness simulate the decrease in stiffness caused by plastic straining through a process called strain hardening. In the model with small-strain stiffness, there is a specific lower limit that constrains the reduction curve of stiffness at minimal levels of strain. In the

hardening soil model with small-strain stiffness, the quasi-elastic tangent shear modulus is computed by integrating the reduction curve of the secant stiffness modulus over the actual increment in shear strain. Figure 5.2 exposes the stiffness reduction curve in the hardening soil small-strain model.

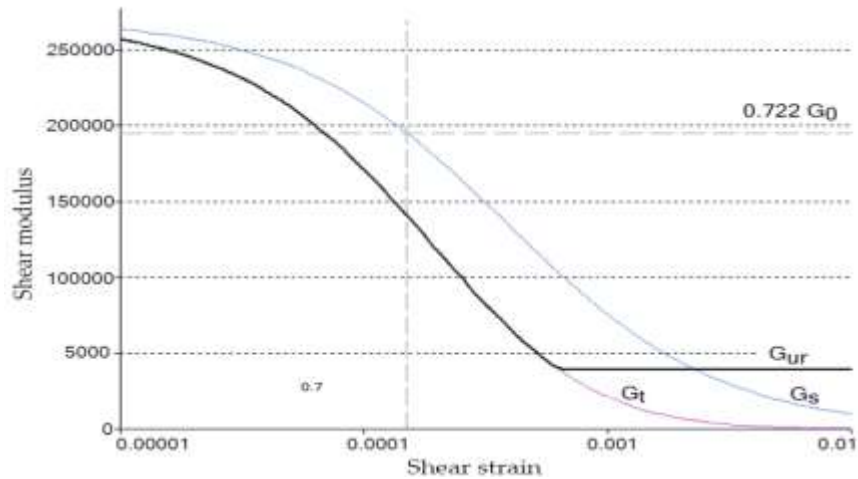


Figure 5.2: Secant and Tangent Shear Modulus Reduction Curve

5.1.2 Soil and Slab Parameters

A series of six Plaxis 3D models were developed and analyzed to determine the results of slab settlement when superimposed on top of six different soil subgrades with varying relative density values (RD-40, RD-45, RD-50, RD-65, RD-70, and RD-75). In every model, the soil type was defined as the HSs model. The soil parameters were calculated based on the RD percentage of the sandy soil utilizing the empirical equation proposed by (Brinkgreve et al., 2010). The soil parameters between RD-40% to RD-75% were varied by amending the basic properties such as saturated and unsaturated unit weight, four stiffness parameters such as Secant stiffness in standard drained triaxial test (E_{50}^{ref}), Tangent stiffness for primary oedometer loading (E_{oed}^{ref}), Unloading/reloading stiffness from the drained triaxial test (E_{ur}^{ref}), and power for a stress-level dependency of stiffness (m), the

strength, and small strain parameters as mentioned above in section 5.1.1. Irrespective of the sandy soil type based on RD percentage the Poisson's ratio ν'_{ur} for unloading and reloading was specified as 0.2, and the reference stress level P^{ref} is fixed at 100 kN/m².

Table 5.1 denotes the material properties of all the soil.

Table 5.1: Plaxis-3D Soil Material Properties

Properties	RD40%	RD45%	RD50%	RD65%	RD70%	RD75%	units
Material	HSs	HSs	HSs	HSs	HSs	HSs	-
Model							
Drainage	Drained	Drained	Drained	Drained	Drained	Drained	-
Type							
γ_{unsat}	16.60	16.80	17.0	17.6	17.8	18	kN/m ³
γ_{sat}	19.64	19.72	19.8	20.04	20.12	20.2	kN/m ³
E_{50}^{ref}	24.0e3	27.0e3	30.0e3	39.0e3	42.0e3	45.0e3	kN/m ²
E_{oed}^{ref}	24.0e3	27.0e3	30.0e3	39.0e3	42.0e3	45.0e3	kN/m ²
E_{ur}^{ref}	72.0e3	81.0e3	90.0e3	117.0e3	126.0e3	135.0e30	kN/m ²
m	0.575	0.5594	0.5437	0.4968	0.4813	0.4656	-
G_0^{ref}	87.2e3	90.6e3	94.0e3	104.2e3	107.6e3	111.0e3	kN/m ²
$\gamma_{0.7}$	0.16e-3	0.155e-3	0.15e-3	0.135e-3	0.13e-3	0.125e-3	-
C	1.0	1.0	1.0	1.0	1.0	1.0	kN/m ²
φ (ϕ)	33	33.63	34.25	36.13	36.75	37.38	°
Ψ (ψ)	3	3.625	4.25	6.125	6.75	7.375	°
R_f	0.95	0.9438	0.9375	0.9188	0.9125	0.9063	-
K_0^{nc}	0.4554	0.4462	0.4372	0.4105	0.4017	0.3930	-
R_{inter}	0.7	0.7	0.7	0.7	0.7	0.7	-

The concrete slab was defined under the set type - soil and interfaces as a linear elastic material model and the drainage type was assigned as non-porous. The concrete slab properties were the same for all six models used to validate the experimental results. A steel bearing plate was modeled under set-type plates and specified as an elastic material. Table 5.2 shows the material properties of concrete slab and steel bearing plate.

Table 5.2: Material Properties of Concrete Slab And Steel Plate

Properties	M30 Concrete Slab	Steel Bearing Plate	Units
Material Type	Linear Elastic	Elastic	-
Drainage Type	Non-Porous	-	-
d (diameter)	-	0.03	m
γ	24.0	78	kN/m ³
E	31.53e6	200e6	kN/m ²
ν	0.15	0.35	-
G	13.7e6	74.07e6	kN/m ²
E_{oed}	33.26e6	-	kN/m ²

The soil parameters for each soil type falling under different relative densities were calculated based on the fundamental empirical equation which was derived and validated for different soil data with varying relative density values and soil pressure. (Brinkgreve et al., 2010). However, these formulations function highly beneficial during the initial stages of the project, especially in situations where soil data is inadequate. The empirical formulas used to derive the HSs model parameters corresponding to the relative density (RD in %) for different soil subgrades have been presented in section 2.6.

5.1.3 Borehole and Subgrade Modeling

A Plaxis 3D model with 10-noded elements was selected for all the FEA models. The units were mentioned as meters (length), kN (force), and day (time). The contour dimensions of the soil body were assigned under the following dimensions: $X_{Max} - 2.75$ meters, $X_{Min} - 0$, $Y_{Max} - 2.25$ meters, and $Y_{Min} - 0$. The borehole was assigned exactly at (0, 0, 0) coordinates in the Soil stage. Similar to the dimensions of the soil tank of 2.75 m X 2.25 m X 1.85 m the contour was assigned with the maximum boundary limit using this dimension, the soil was filled up to a depth of 1.5m inside the soil tank. Hence, the borehole was assigned with top value (0 meters) and a depth/bottom value of -1.5m. The groundwater head level was set at -1.6 m in all the FEA models as the soil did not have any groundwater flow in the laboratory tests. According to the model requirements, the soil material was defined as either of the following ones (RD40%, RD45%, RD50%, RD65%, RD70%, and RD75%) and was assigned to the soil body. Figure 5.3 displays the constructed soil subgrade in Plaxis 3D.

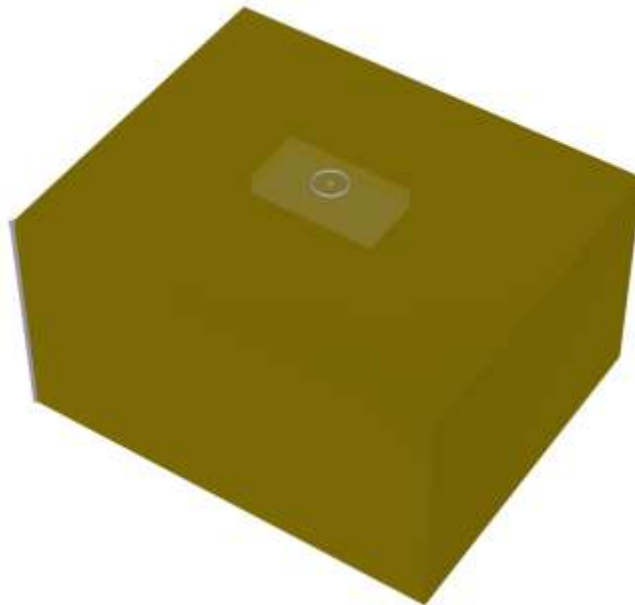


Figure 5.3: Soil Subgrade Model in Plaxis 3D

5.1.4 Modeling of Concrete Slab

Once the soil subgrade was modeled according to the soil tank dimensions, the slab would be oriented exactly in the middle of the soil body, by imposing the centroid of the slab above the middle of the soil top surface. The slab surface was generated and positioned on top of the soil with the surface coordinates of (A - (0.975,0.925,0), B - (1.775, 0.925,0), B' - (1.775, 1.325,0), A' - (0.975, 1.325,0)). The slab surface was extruded in the positive z-coordinates to attain the required thickness of 0.127 m. The concrete volume was generated, and the concrete material properties were assigned to it. A negative interface was created for the concrete slab-on-grade structure to simulate the interaction between structure and soil. Node pairs were generated at the interface between the structure and the soil by the use of an interface. In a pair of nodes, one is associated with the concrete slab, and the other is associated with the soil beneath it. Two elastic-perfectly plastic springs connect these two nodes in contact. Two elastic-perfectly-plastic springs: one to represent the displacement in the separation and another to represent the displacement in the slip. A steel-bearing plate with a diameter of 0.205 mm was superimposed in the middle on top of the slab by aligning the radial point of the plate to the central midpoint (1.375, 1.125, 0.127) of the slab. The steel-bearing plate material properties were assigned to the plate. A point load was allocated exactly at the centroid of the steel plate. A secondary sub-soil structure was modeled inside the existing soil body beneath the slab with the coordinates of (D - (0.375,0.250, 0), E - (2.375, 0.250, 0), F - (2.375, 2.000, 0), G - (0.375, 2.000, 0)). The subsoil structure was then extruded to a depth of -1.2 m in the negative Z-axis. The structure was left unassigned as a volume. This additional sub-soil structure will be used to generate

a denser mesh pattern beneath the slab. Figure 5.4 exposes a visual view of the structural stage in Plaxis-3D.

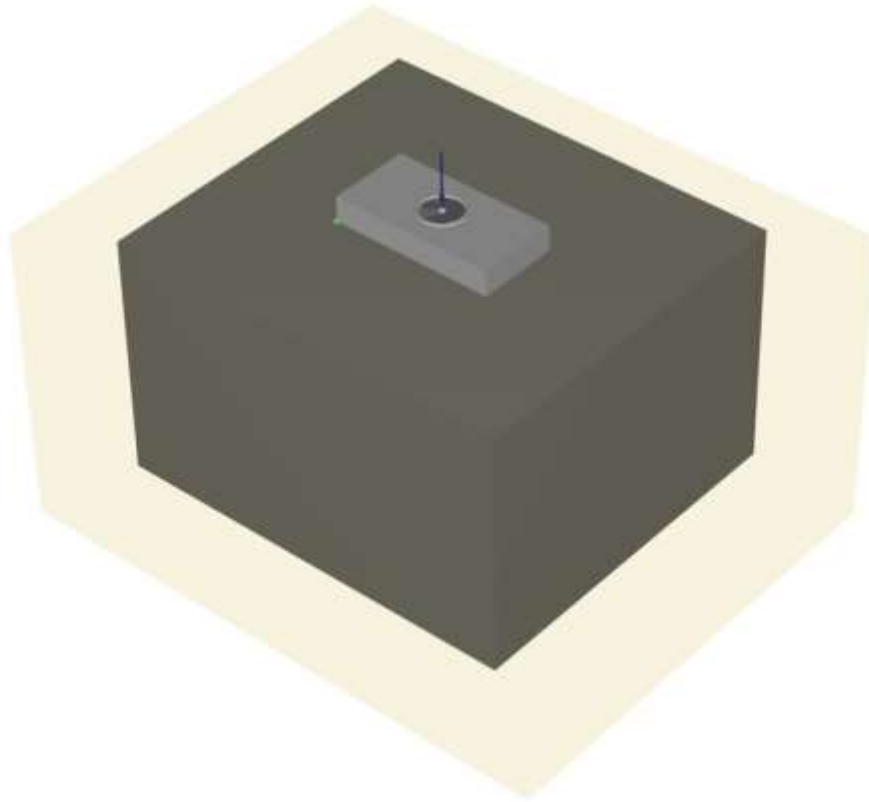


Figure 5.4: Structure Stage in Plaxis 3D

5.1.5 Generating Geometric Mesh

Every Plaxis 3D model used to validate the laboratory testing data had been modeled under the same meshing and boundary conditions. There were two contour soil structures developed in all the Plaxis models. The mesh element distribution pattern was assigned as medium distribution for all models. The exterior contour soil volume was meshed with a coarseness factor of 1.0. The inner contour soil volume which is confined tightly by the exterior contour would be meshed with a coarseness factor of 0.3536, which indicates that the meshing conditions were refined three times more than the exterior soil volume. The negative interface of the concrete volume will be assigned a coarseness factor of 0.3536

similar to the inner contour soil volume as the interfaces adhere to the adjacent soil material mode. The concrete volume, steel bearing plate, and point load were refined twice as much as the preexisting coarseness factor to attain a value of 0.5. Once, all the coarseness factors are assigned, the mesh element distribution pattern is mentioned as a medium and the mesh is generated. Under the specified meshing conditions, the generated mesh comprised 79872 elements and 111100 nodes throughout the structure. In all Plaxis 3D models, the horizontal boundary conditions were set as normally fixed in both positive and negative coordinates of the X and Y axes. The vertical boundaries were prefixed in two different patterns, the positive Z coordinates were assigned as free, while the negative Z direction was set under fully fixed conditions. The Dynamic boundary conditions were assigned as viscous in both the X and Y axis horizontally, whereas it was set as non in the vertical axis. The global water level was fixed at the borehole water level to depict the soil condition that was attained in the laboratory soil tank.

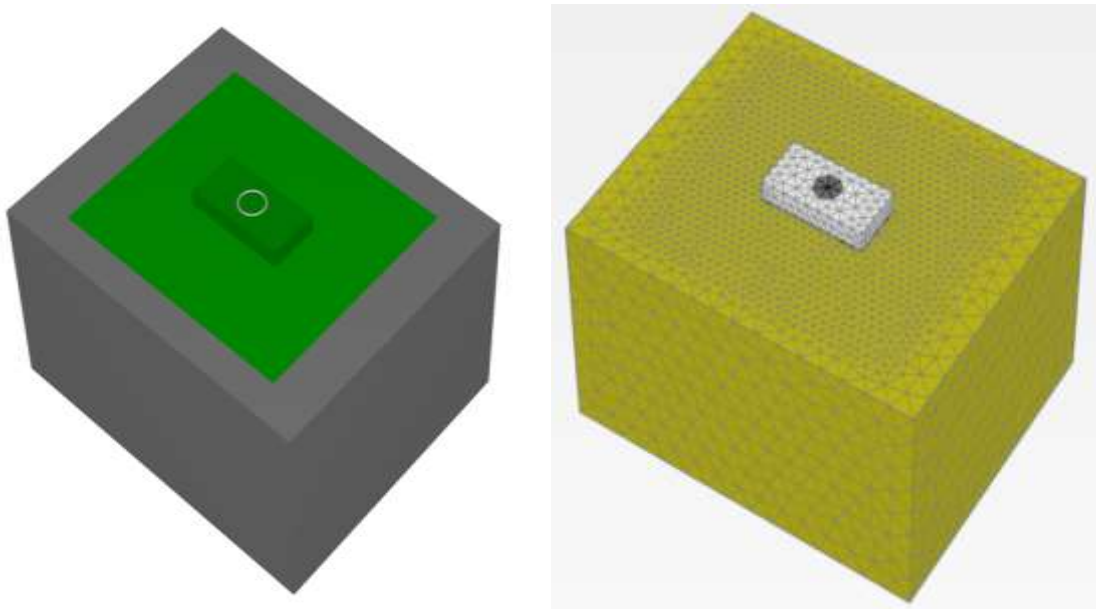


Figure 5.5: Meshing Stage

5.1.6 Stage Construction

In the developed Plaxis 3d models every defined element was activated sequentially as per the construction process under different phases. Each structural element was activated in separate individual phases to determine the progressive stress, strains, and initial deformation values that were generated due to its activation. In the initial phase, the whole soil volume was activated, and it was analyzed following the K0 procedure, to establish the immediate generation of initial effective geostatic in-situ stresses in the soil, the pore pressure was not brought into effect as the water head level was set beneath 1.5 depth of soil. As the initial soil conditions were analyzed and calibrated, the first phase of construction simulated the activation of the concrete slab and the negative interface of the concrete slab. Phase 1 was set to simulate the soil structure under a plastic state to stimulate the elastoplastic drained analysis to evaluate the stress, strain, and elastic deformation of the soil. All the upcoming phases were set to formulate analysis under the elastoplastic drained analysis. In phase 2 the steel bearing plate positioned in the middle of the concrete slab was activated and set to analyze the change in soil structure due to its stress.

In the third phase, the point load positioned preciously in the middle of the steel bearing plate was activated. The point load was calibrated to exert a certain amount of load set to stimulate the stress through the bearing plate onto the slab on grade, the load was regulated varying between 70 to 120 kN depending on the soil parameters with concern to the relative density of soil. Apart from these, the soil would have experienced a certain amount of stress due to the activation of concrete slab-on-grade and the steel bearing plate, which eventually simulated the soil to attain a minimal amount of settlement and small strain. In the experimental laboratory analysis, the soil was compacted and produced according to the

required relative density value. The concrete slab was then positioned in the middle of the soil's top surface. All the LVDTs and the strain gauges were wired to the connection deck which transfers the obtained strain values to the data acquisition system. The value of all LVDTs and strain gauges were calibrated to zero after which the test would commence. Similarly, to attain a precisely comparable stage before the load initialization, in the third phase, the attained displacement and small strain effect of the soil were reverted to zero. The utilization of default iteration parameters was disabled, and the arc length control type was turned off to improve the convergence of the load-displacement curve by regulating the load incrementation. The maximum step for this stage was increased to 3000 to prevent the analysis from terminating the simulation due to maximum step failure. Six different nodes were assigned on the concrete slab, four nodes were assigned at the corner of the slab and two nodes were assigned in the middle of the longer span of the slab. All six nodes were positioned approximately at the same position where the 6 LVDTs were positioned on top of the slab during the experimental analysis. Figure 5.6 depicts the stage construction of a Plaxis 3D model.

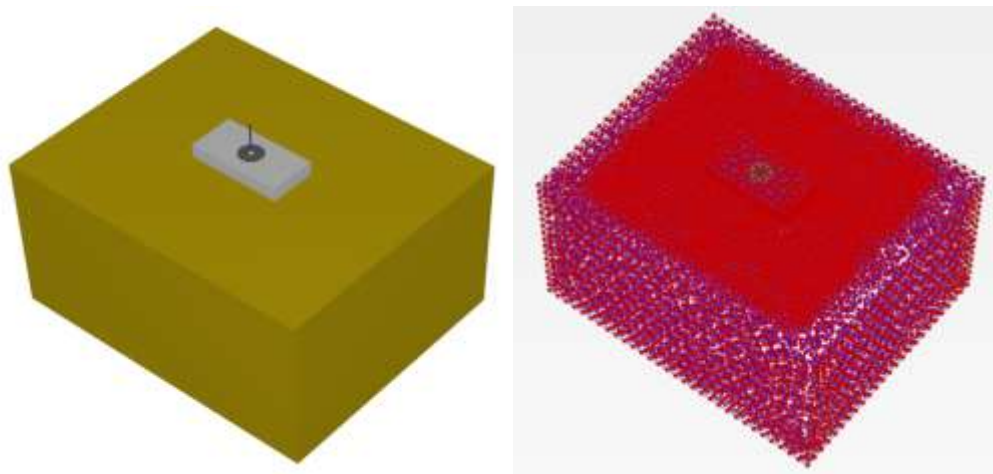


Figure 5.6: Stage Construction and Node Points

5.2 Validation of Field Data with Plaxis 3D Results

Figure 5.7 exhibits the result comparison for the soil displacement caused by the monotonic load test of slab-on-grade specimens examined in the soil tank at the Heavy Structures lab against the displacement (U_z) of slab-on-grade obtained from various Plaxis 3D models with different soil properties concerning the varying relative density of soil. This comparison is done to validate the relative density of non-geocell soil, which was calculated for each slab testing through the sand cone and compaction tests. It substantiates the lab soil test results by comparing them with Plaxis 3D model results. A series of six Plaxis 3D models were developed and analyzed to determine the results of slab settlement when superimposed on top of six different soil subgrades with varying relative density values (RD-40, RD-45, RD-50, RD-65, RD-70, and RD-75).

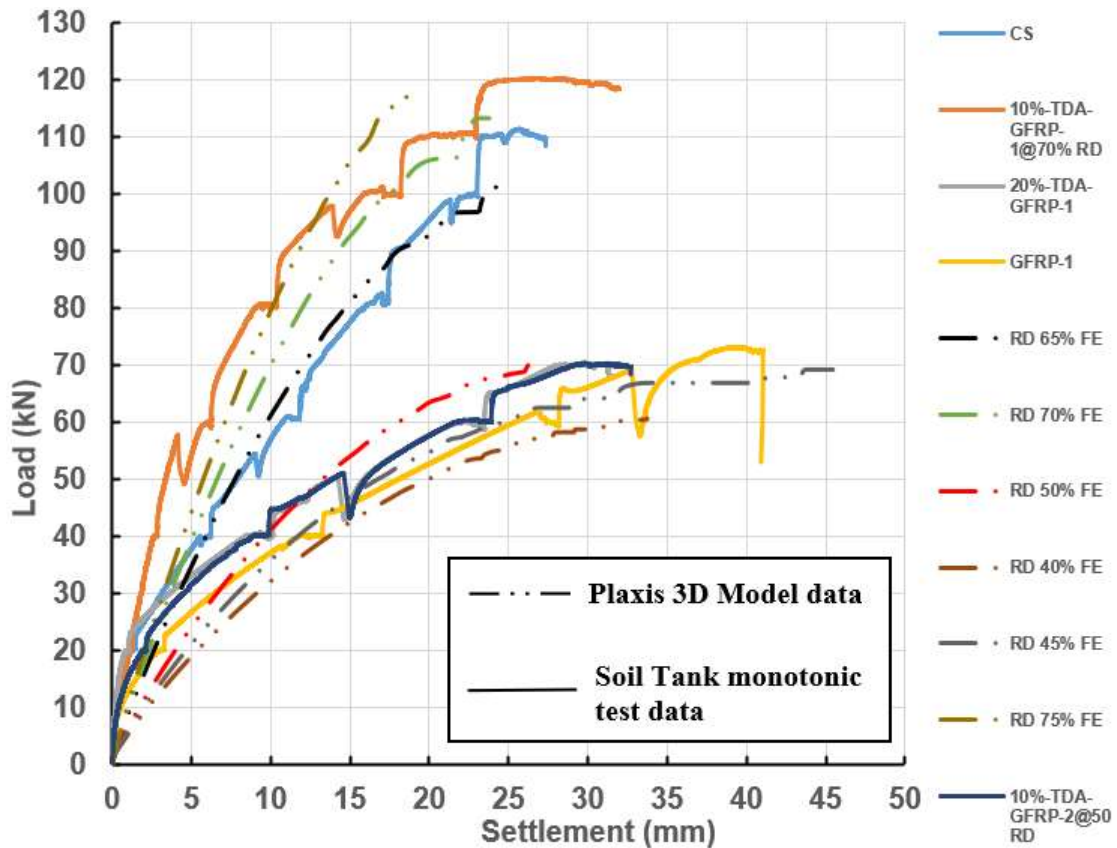


Figure 5.7: Validation of Lab Testing Data

From Figure 5.7, it is visible that there were two sets of load vs settlement curves, the lower set of curves fell under 40% to 50% of RD and the second set fell under 65% to 75% of RD. GFRP-1, 10%-TDA-GFRP-2@50% RD, and 20%-TDA-GFRP-1 Specimens were tested on top of the soil which had a Relative density of 48.69%, 49.82%, and 50.28% respectively. Plaxis 3D FEA, performed under 40%, 45%, and 50% RD soil parameters yielded a comparable result with these three slab specimen results. In Figure 4.19, it is evident that all three lab test results had a comparatively very stiffer soil condition during the initial stage of the test, but above 40 kN load, the lab test results began to align in between the Plaxis 3D results. Around 60 kN to 70 kN load all three laboratory test results were varying between the 45% to 50% RD Plaxis 3D results.

In the second set of curves, the Control specimen (CS) and 10%-TDA-GFRP-1 slab specimens were tested on top of the soil which had RD of 68.03% and 70.59% respectively. In lab testing circumstances the soil showed immense stiffness up to 40 kN. Above 40 kN load the CS began to align exactly with the 65% RD Curve attained from Plaxis 3D. At the point of reaching 90 kN, the CS curve was wavering between RD 65% FE and RD 70% FE curves. While the 10%-TDA-GFRP-1 slab specimen shows a comparatively stiffer settlement pattern, it sustained above the RD 75% FE curve till 80 kN, beyond which the soil exhibited a plastic behavior and the curve deviated towards the RD 70% FE curve. Thus, based on this validation done against the Harding small strain (HSs) soil model in the Plaxis 3D FEA software, it is evident that the relative density values calculated for each slab test results were precise and accurate. The same field test procedures can be followed for the geocell-reinforced soil subgrade to derive its relative density.

5.3 Conclusion

This Chapter summarizes the materialistic properties used in the Plaxis 3D model for sandy soil subgrade, concrete slab, and steel bearing plate. It also emphasizes model development methodology and discusses the model validation of laboratory testing against the Plaxis 3D FEA model results.

The HSs soil model showed appropriate results. The Plaxis 3D model results exhibited prominent alignment for the load VS settlement curve with the experimental lab monotonic load test results. Hence, the Plaxis 3D models displayed rational and comparable results, to validate the experimentally calculated soil parameters and their relative density. Based on Plaxis 3D validation, the soil parameters, and relative density values attained through in-situ soil testing are significant. It is recommended to compact the geocell-reinforced soil accordingly to attain the same 50% RD to evaluate the influence of geocell in terms of settlement rate, soil crack pattern, soil cracking load, and concrete cracking load.

CHAPTER-6 GEOCELL REINFORCED SOIL RESULTS

DISCUSSION

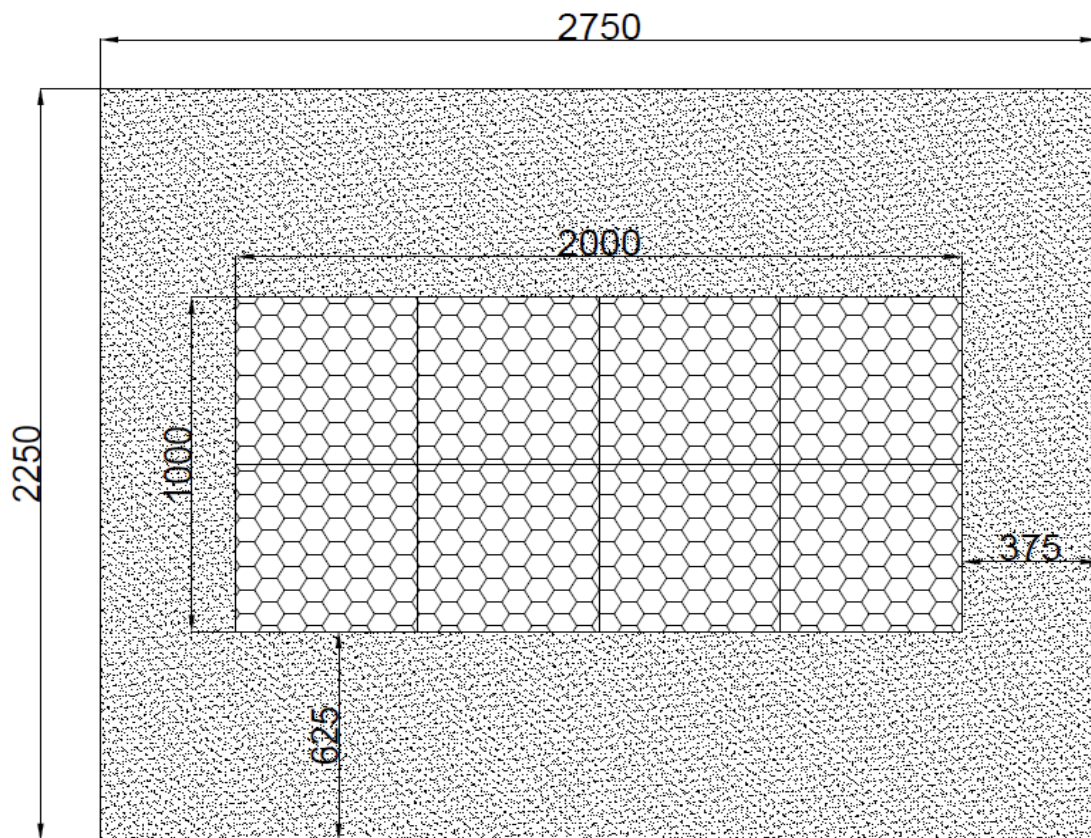
6.1 Introduction

This chapter comprises the results and explanation of the experimental monotonic load test executed on the GFRP-2 and 20%-TDA-GFRP-2 slab specimens on top of geocell-reinforced soil. The sandy soil was reinforced with geocell at a depth of 150 mm beneath the top surface of the soil before slab testing. This test was conducted to identify soil structure behavior and the effectiveness of geocell reinforcement. Specifically, the variation that occurs in the bearing capacity of the soil, types of soil cracking pattern, surface heaving, and the load vs settlement rate with geocell-reinforced soil were compared with the slab results attained on top of normal soil subgrade conditions. The change in concrete cracking load and strain during the cracking load and the strain development rate for each slab specimen will be discussed and compared with the slabs tested on normal soil conditions.

6.2 Geocell Soil Preparation Method

Initially, the top two layers of the soil were shoveled out into the industrial nylon bag and the third layer of the soil was disturbed inside the soil tank by inverting the whole layer with the shovel. The soil was distributed throughout the soil tank using the shovel and the soil layer was spread evenly using a 4-foot-long wooden plank and the soil layer was uniformly leveled. Three bottles of water were sprinkled on top of the soil layer. Once, the soil was moist, the third layer was compacted using the same compaction mechanism. As the soil layer was compacted the soil parameters were examined and the relative density of the soil layer was checked if it lies between 45 to 50%. On top of that compacted layer, an additional bag of soil was released with the assistance of the industrial crane. The layer

was moist with the same quantity of water and compacted using the same compaction mechanism. The soil parameters were attained through two sand cone tests at different spots and the relative density of the soil was acquired. The soil was initially removed according to a calculation, which yielded 150 to 155 mm of subgrade space above the second layer. This was done intentionally to place the geocell precisely at 150 mm below the top surface level. Sequentially, the geocell layer was installed on top of the prepared top-1 soil layer. The geocell layer was designed to be installed with a scale of 2.5 times the slab dimensions. The length of the geocell layer was designed to be 2 meters and the width was determined to be 1 meter. Figure 6.1 depicts the layout of geocell layer alignment on top of the top-1 soil layer and the installation of geocell in the soil tank.



ALL DIMENSIONS ARE IN MM

(A)



(B)

Figure 6.1: (A) Geocell Alignment on Top of The Second Soil Layer (B) Geocell Installation

Each geocell panels were placed in its position precisely based on the calculated spacings between the geocell's longer and shorter spans against the soil tank side walls. Once all eight geocell panels were interlocked and connected in position to form a geocell layer, the spacing between the geocell layer's perimeter and the soil tank walls was verified. The topsoil layer was discharged into the soil tank on top of the geocell layer as shown in Figure 6.1 (b) utilizing an industrial crane. The Soil layer was uniformly spread across the tank surface using the spreading tools. As the soil was spread on top of the geocell layer, it eventually got compacted while leveling out the soil layer. Thus, the compaction rate must be reduced for the top layer of soil. Subsequently, as the soil was leveled out, the same amount of water was sprinkled proportionately across the soil surface area. A small 500 mm X 500 mm wooden plank was imposed on top of the soil surface and the compacting tool was superimposed on top of the wooden plank. The compaction hammer was dropped once in a single spot. This compaction rate would be followed for each compaction spot throughout the soil surface area. The relative density of the soil was assessed based on the soil parameters obtained through the sand cone test. If the RD was less than 45 % the soil was compacted again utilizing the same compaction method, consequently the top surface attained an RD value between 45% - 50%. Subsequently, the slab-on-grade specimens were positioned in the middle of the soil surface and tested. This method was repeated to reproduce the whole soil subgrade appropriately for every slab-on-grade specimen testing.

6.3 Monotonic Load test of Slab-on-grade on Geocell-Reinforced Subgrade

6.3.1 Geocell-Reinforced Subgrade Response With GFRP-2 Slab

Prior to placing the slab on top of the geocell-reinforced soil, two 120-ohm strain gauges were installed on the compression side and two strain gauges were positioned exactly

beneath the top two strain gauges, on the tension zone. The slab was placed precisely in the middle, beneath the hydraulic actuator. All six LVDTs were positioned appropriately at the same spot similar to the previous test setup. All the strain gauges, six LVDTs, and load cells were connected to the data acquisition system. Once all the LVDTs, load cell, and strain gauge readings were zeroed out, the system was armed for testing. The geocell-reinforced soil subgrade had an average relative density of 50.36%.

Initially, the portable oil pump was turned on and left undisturbed until the oil drove through the hose and pressured the hydraulic actuator piston. Once the load cell showed significant pressure, the loading gauge was manually rotated clockwise to boost piston oil pressure. This was done slowly till the 20 kN load interval to get the best linear result. At the 20 kN load interval, the pump oscillated between 20 to 20.25 kN, and the soil settlement rate was inspected for all the LVDTs to attain a minimum settlement rate of 0.03 mm/min deformation for a couple of consecutive 3-minute intervals. The soil had settled to 2.475 mm at the initial stage of inspection. As the soil was reinforced with a geocell panel, the load exerted by the slab onto the soil surface was distributed evenly throughout the soil volume. Thus, it took only 4 cycles to attain the required settlement rate. In the last inspection, the slab had sunk 2.577 mm into the soil's top surface. The soil had no cracks throughout the 20 kN load interval and the concrete did not yield. The maximum strain developed in the concrete slab at the 20 kN load interval was -3.041 (SG1) and -5.588 (SG2) on the compression side, and on the tension side, it was 3.554 (SG3) and 4.062 (SG4). Figure 6.2 shows the load vs settlement curve of the GFRP-2 slab tested on geocell-reinforced soil.

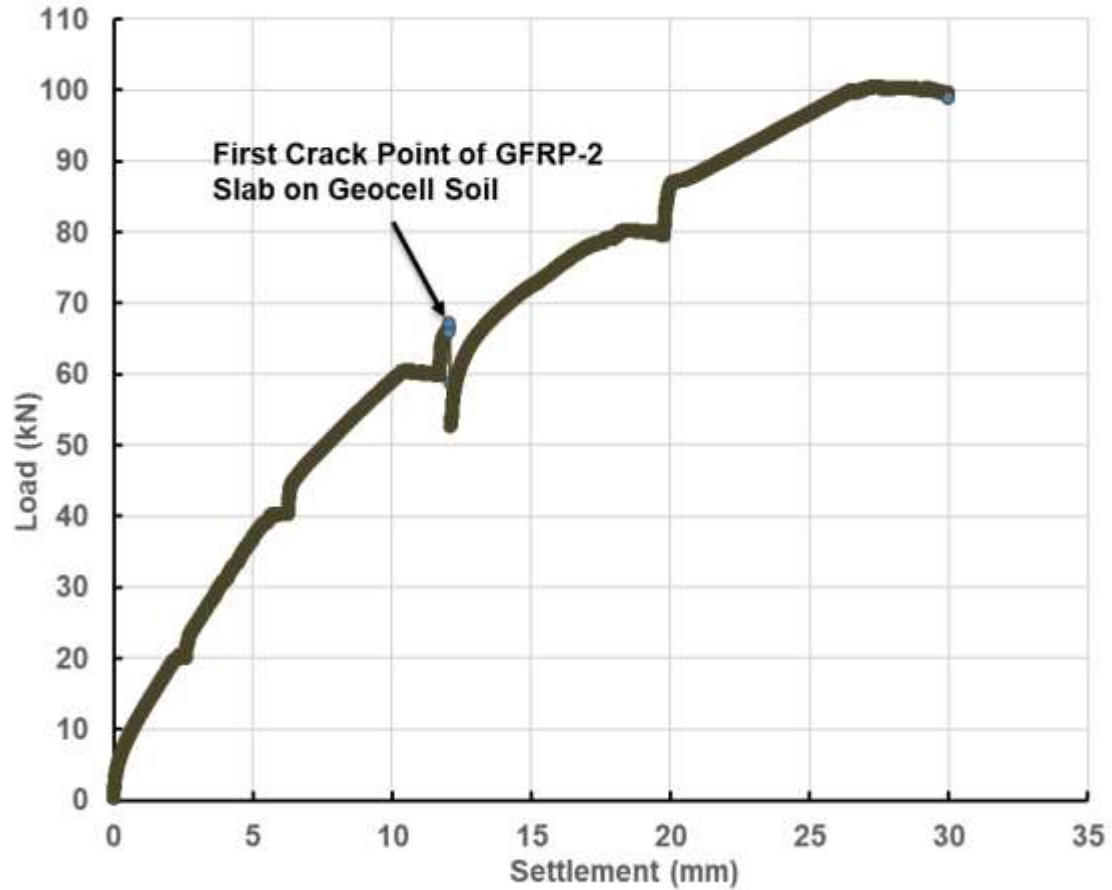


Figure 6.2: Load VS Settlement Curve Of GFRP-2 Slab on Geocell-Reinforced Soil

As the desired results were derived the loading gauge was rotated clockwise manually to impose more oil pressure on the piston. The load was incremented to 40 kN at a uniform pace to get a linear inclination of load. During the load incrementation process, the slab and the soil reaction were monitored visually to identify if cracks were imposed on the soil and concrete slab. No cracks were generated on both the soil and the concrete slab till the load reached 40 kN. As the actuator imposed a 40 kN load on the slab, the soil had deformed to 5.961 mm. Since the geocell was inserted as a soil reinforcement, the stress exerted on the soil got spread evenly and forced the soil particles to deform slowly causing the slab to settle uniformly. Due to this, the soil subgrade manifests stiffer behavior, causing it to achieve 0.03mm/min settlement over six cycles of inspections. At the last iteration,

the slab had immersed down to 6.225 mm. Due to the geocell reinforcement, the soil particles were tightly confined and maintained their elastic state throughout the settlement inspection. The concrete slab produced marginally higher strain on the tension zone (16.753 – SG3 and 18.28 – SG4), while the compression zone had strain values of -14.7 (SG1) and -15.748 (SG2).

The loading gauge was revolved clockwise to surpass more oil through the hose, thus inflicting more oil pressure against the piston to escalate the load to 60 kN. From Figure 5.2 it is evident that the soil evinces a dominant stiffer reaction till the pressure rises to 45 kN, beyond which the slab begins to sink further into the soil structure. During the load incrementation phase, the soil was visually observed, and the slab's reaction was video recorded to ascertain the soil and slab cracking point. The monitoring of the loading phase has indisputably displayed that the soil reinforced with the geocell has delivered predominantly stiffer soil under the RD of 50%. Eventually increasing the load-carrying capacity and elastic limit of the soil without yielding any shear cracks or small fractures due to the transmitted pressure. The soil particles had deviated to a certain extent which made the slab submerge to a depth of 11.152 mm at 60 kN. The geocell drastically reduced the soil particle dispersion rate during the load inspection cycles. Thus, the slab had only settled 0.52 mm throughout the inspection period. It took ten iterations for the geocell-reinforced soil subgrade to proclaim the required settlement rate. By the last iteration, the soil had sustained transmitted pressure and secured the slab at 11.673 mm depth. The concrete slab showed exceptional elastic mechanism as it did not procure any flexural and shear cracks. The soil showed prominent elastic properties during the settlement inspection cycle and did not acquire any cracks. The maximum strain the concrete experienced at 60

kN load was -26.86 (SG1) and -26.416 (SG2) in the compressive zone, in the tension zone the strain oscillated at 27.414 (SG3) and 31.99 (SG4) on both halves of the slab. Figure 6.3 displays the stress-strain curve of the GFRP-2 slab.

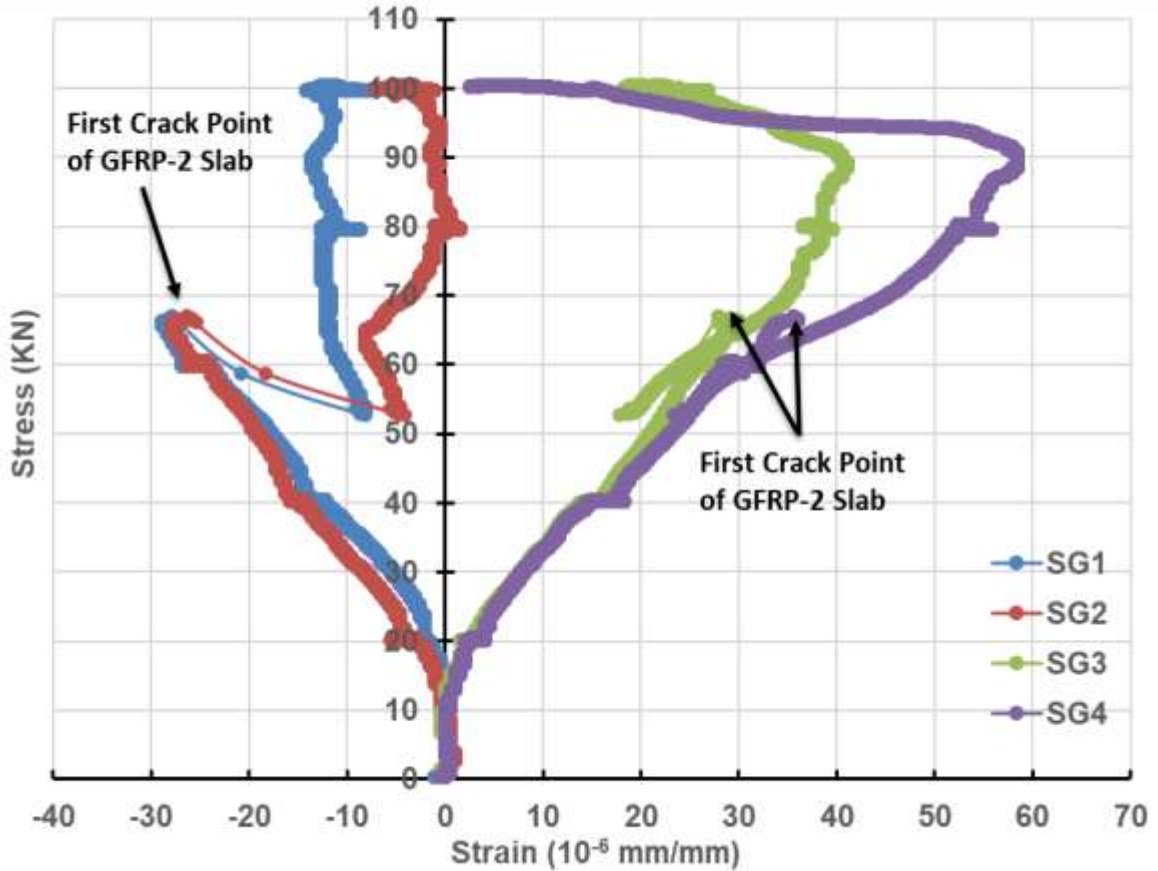


Figure 6. 3: Stress-Strain Curve Of GFRP-2 Slab on Geocell Reinforced Soil

The actuator was infused with more oil pressure by twisting the loading gauge, to increment the imposed load to 80 kN. Since the soil was left to isolate for more than 30 minutes under a 60 kN load, it instigates the stiffness level of the soil to a certain extent. Thus, the soil exhibited a stiffer mechanism until the load reached 65 kN, resisting the slab to settle just 0.14 mm (11.82mm) more than its previous 60 kN settlement value. Once the actuator pushed the load beyond 65 kN the soil particles began to deviate outwards due to excessive pressure distribution in the soil. The concrete slab exceeded its elastic limit by yielding at

67.133 kN, producing two flexural cracks in the middle of the slab indulging into the compressive zone. Circumstantially, due to the flexural crack, the slab bent allowing the load to fluctuate down to 52.64 kN. Once, the slab generated a flexural crack the loading gauge was left ideal, as the existing oil pressure will push the piston to retrieve the load to its desired level. The soil was performing exceptionally well as it did not generate any cracks. Eventually, as the load crept up to 60.67 kN the loading gauge was again tightened clockwise to pervade further oil into the hydraulic actuator to escalate the load to 80 kN. Between 78 to 79 kN, the transmitted load surpassed the load-bearing limit inducing the soil to develop surface cracks at all four corners of the slab. During the 80 kN load interval, the width of the flexural cracks on the concrete was 1 mm wide on the LVDT2 side and 0.75 mm wide on the LVDT5 side. At the 10 min evaluation, the soil surface cracks were measured to be 10.2 mm @ A, and a split crack was generated at A' each one was found to be 12.3 mm and 10.6 mm long. Whilst on the other end at Section B-B', at B the soil exposed a single crack of 10.8 mm long, and B' had developed a split crack with lengths of 14.1 mm and 9.4 mm respectively. The soil had no passive effects or lateral cracks during this stage. The desired 0.03mm/min settlement rate for the slab was acquired after fourteen three-minute intervals. During the first iteration, the slab had descended 18.667 mm on average for all LVDTs, by the end of the settlement analysis the slab went down to 19.661 mm as the soil deviated around 1 mm under the same load. As soon as the concrete slab cracked, strain gauge 2 transmitted a reasonable value until the load crept up to 60 kN, beyond which it failed, as it transmitted false values. The Maximum strain value experienced by the concrete at 80 kN on the compression side was -12.673(SG1) and -1.016 (SG2), whilst the tension zone was experiencing a higher strain value of 39.599 (SG3)

and 55.857 (SG4). This drop in strain at compressive and sudden inflation on the tension zone happened due to the flexural crack.

The test proceeds further by proliferating the load to 100 kN using the loading gauge in the portable oil pump. The soil particles showed exceptional stiff behavior as the load climbed up to 86.65 kN, and the soil was able to sustain the slab within 20 mm of settlement. As the actuator toggled gaining more oil pressure, pushed the load further, causing a predominant amount of soil particles to lose their friction which enabled the slab to push through the soil surface. Approximately at 92.6 kN the mid-section of the slab had reached 25 mm of settlement. At 100 kN the slab has submerged 27.65 mm down into the soil surface. During the 100 kN loading phase, the concrete slab experienced a sudden dip in the strain values. In the compression zone, the maximum strain value was -14.193 (SG1) and -7.112 (SG2), similarly the strain values dropped majorly in the tension zone to 26.907 (SG3) and 2.539 (SG4). As the soil performed exceptionally under an RD of 50% due to the influence of geocell, the crack in the slab grew deeper and wider. Alongside, due to a higher strain value, the concrete has yielded a lateral crack above the neutral axis diverging away from the existing flexural crack on the LVDT 5 side at a load of 90 kN. The crack on the LVDT2 side had grown to 2 mm at the bottom and 1.5 mm at the neutral zone, converging to 1–0.75 mm above the neutral axis. LVDT 5 side crack width widened to 1.75 mm at the tension zone, reduced to 1.25 mm at the center, and then dropped to 0.75 – 0.5 mm above the neutral axis. The lateral crack was measured to have a width of 0.5 mm. Based on the behavior of the stress-strain curve in Figure 6.3, it is observed that the SG4 is transmitting readings that were deducing down to 0 as the load increases to 100 kN. This emphasizes that the lateral crack has reduced strain in the tension zone. Even though the

soil had geocell reinforcement as the load was very huge for soil with RD 50%, it exposed plastic behavior. The soil did not exhibit heaving of the top surface on either side, but it has generated several lateral cracks running parallel and perpendicular to both longer spans of the slab roughly at a load varying between 97 to 98 kN. The longest crack on the longer span side was measured to be 43 mm on the LVDT 2 side and 41 mm on the LVDT 5 side. The pressure was delivered to a large region by geocell, causing steady settlement during loading. The allotted settlement rate of 0.03mm/min for 3-minute gaps was proclaimed after sixteen settlement inspection cycles. In the first cycle, the slab dispersed soil particles and sunk 28.37 mm. Geocell-influenced soil sustained settlement rate and slab settlement at 29.499 mm. Since all expected findings were obtained, the load was gently deduced by spinning the loading gauge anti-clockwise and the test was concluded.



(A)



(B)

Figure 6.4: (A) Soil Crack at Sections A-A1, B-B1, and Lateral Cracks (B) Flexural Cracks of GFRP-2 Slab

6.3.2 Geocell-Reinforced Subgrade Response With 20%-TDA-GFRP-2 Slab

The soil subgrade was disturbed up to the top three levels after the previously tested. Each soil layer will be compacted using the above approach. The soil geocell will be removed and reinstalled at 0.15 meters below the surface. The topsoil subgrade layers had 50.11% relative density. The 20%-TDA-GFRP-2 specimen was placed precisely in the center of the top surface underneath the hydraulic actuator. The test would be initiated once the slab test setup was completed. The load was tweaked up to 20 kN gradually by releasing oil into the actuator by twisting the loading gauge. As the load hits the 20 kN mark the actuator

was set to operate at this load till the desired settlement rate is attained. Both soil and concrete were in their elastic state as they did not experience any cracks. It just took four cycles to obtain 0.03 mm/min for two consecutive 3-minute intervals. The slab had a liberal settlement of around 1.763 mm in the initial first settlement analysis. The geocell-reinforced soil stiffness deemed the settlement down to 1.820 mm in the last cycle of inspection. The strain experienced by the concrete at the 20 kN checkpoint was: -9.122 (SG1) and -7.634 (SG2) on the compression zone, while the tension zone flaunted higher strain values of 14.742 (SG3) and 12.662 on (SG4). The load oscillated between 20 to 20.24 kN due to varied oil pressure and the slab settlement.

At 40 kN load, both the slab and subgrade top surface were visually spectated to identify any crack formation. Based on visual observation and a linear load inclination curve till 40 kN load prove that both soil and concrete did not exert any cracks and withheld their elastic behavior throughout the load settlement analysis phase. The subgrade exhibited predominantly stiffer features similar to the prewise load cycle. The slab sank 4.872 mm at 40 kN. The soil deformed 5.084 mm in the first settlement analysis cycle. Geocell helped the subgrade sustain pressure and reach the required settlement rate in 7 iterations. Eventually, in the last iteration, the slab had pushed through to a depth of 5.347 mm. During the initial stage of testing the soil exhibited immense stiffness under the same RD value. Although the 20%-TDA-GFRP-2 specimen responded exceptionally by sustaining in the elastic limit, the concrete experienced an instantaneous uplift of strain on both the compression and tension zones. On the compressive side, it had adhered to -20.271 (SG1) and -18.829 (SG2) of strain, similarly, the strain value has intensified on the tension zone: 37.617 (SG3) and 27.35 (SG4).

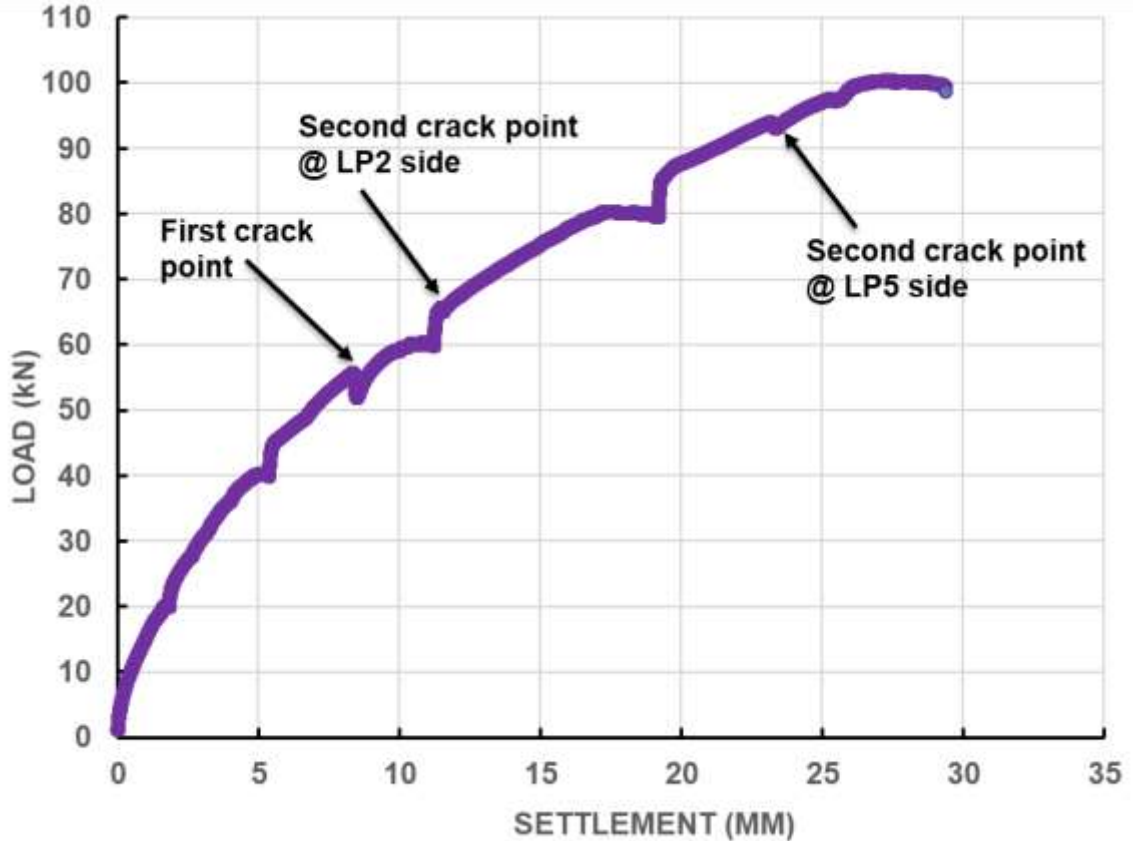


Figure 6.5: Load Vs Settlement Curve of 20%-TDA-GFRP-2 slab on Geocell-Reinforced Soil

The load was incremented to 60 kN by infusing more oil into the hydraulic actuator. Similar to the previous test, initially the soil stiffness exerted shear domination over the load up to 45 kN. Beyond 45 kN the soil particles started to evade due to the pressure distributed by the slab specimen. The slab was recorded visually, and the subgrade top surface was monitored during the load incrementation phase. Figure 6.5 shows that the loading curve has inclined linearly till 55 kN and precisely at 55.62 kN, the graph had a dip in the curve. This reaction transpires the first cracking point of the 20%-TDA-GFRP-1 specimen. As the slab transmitted from its elastic to a plastic state, it exerted a very minimal bend causing load depreciation. The flexural crack on the LVDT 2 side has developed 97.4 mm away

from the LVDT 2 position, whilst on the opposite side the crack evolved approximately beneath the LVDT 5 position. The strain encountered by the specimen during cracking was: (-23.869 @SG1 and -23.918 @SG2) on the compression side, whereas the tension zone had varying strain values of (51.851 @SG3 and 31.908 @SG4). SG 4 quantified 1.625 times greater value than SG3, caused by misalignment of the crack. The loading gauge was left undisturbed till the lost load was regained and then it was operated to push the slab to 60 kN interval. The 20%-TDA-GFRP-2 specimen crack width was measured to be 0.5 mm for both cracks. The geocell-reinforced subgrade took 11 analysis cycles to proclaim the required settlement rate. During the first cycle, the slab had dropped to a depth of 10.69 mm on average, and the soil surface had deformed 11.193 mm below the top surface at the last inspection cycle. The geocell reinforcement worked phenomenally as it did not acquire any cracks and fractures on the top surface till 60 kN. The specimen encountered a reduction in strain value to -19.258 (SG1) and -22.391 (SG2) on the compression side, whereas, on the tension side, it produced an aggravated strain value of 61.002 (SG3) and 31.908 (SG4).

The oil was further inflated gradually into the actuator to push the load to 80 kN. The soil exerted a stiffer reaction against the slab surface area. This made the soil oppose the settlement by absorbing the pressure exerted till 65 kN, which restricted the slab to settle to just 11.37 mm. Apart from this, the subgrade reaction constrained the slab to absorb the additional force imposed on it, which eventually pressurized the slab to produce a second crack on the LVDT 2 side. The second crack happened at 65.604 kN. Due to this, there was a minor deviation in the load and gradually the load escalated to 80 kN. From figure

6.5 it can be observed that the soil particles decompressed and began to evade further as the load increased.

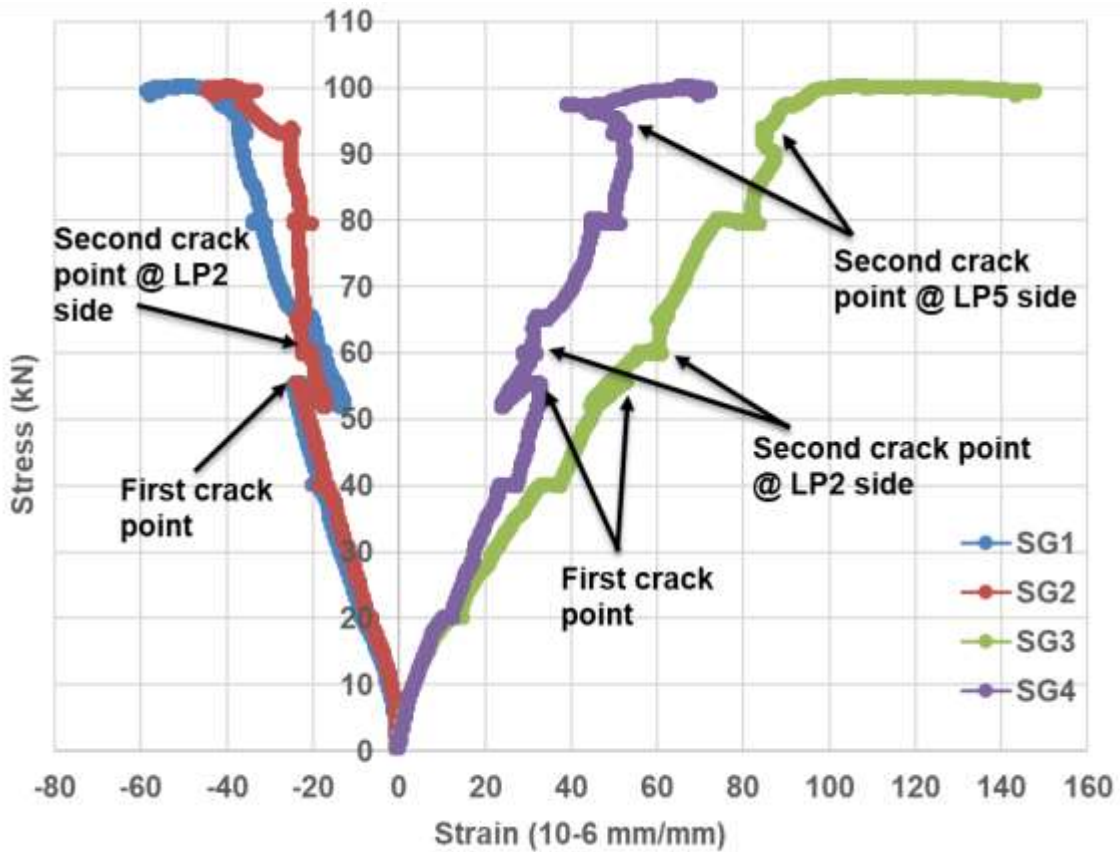


Figure 6.6: Stress-Strain curve of 20%-TDA-GFRP-2 Slab on Geocell-Reinforced Soil

The top surface of the soil developed shear cracks at all four corners of the slab at a load varying between 75 to 76 kN. On the LVDT 2 side, the first crack had widened to a width of 0.75 mm at the tension zone, and the width depreciated to 0.5 mm as it went past the neutral axis. The width of the second flexural crack was scaled to be 0.4 to 0.5 mm thick. Whereas on the other longer span the crack has expanded to a width of 1 mm at the bottom and gradually reduced to 0.5 mm as it goes into compressive zone. Due to the high intensity of strain, the concrete has yielded a lateral crack emerging from the pre-existing crack on

the LVDT 5 side. This crack was located above the neutral axis and was measured to be 0.4 mm wide. As the soil transitioned from a linear elastic to a plastic state, the stiffness index and the friction between the soil particles reduced drastically. At 80 kN the soil top surface had declined to a depth of 17.115, hence this shows that the soil particles were decompressing at a fast pace. Due to this, the soil took 18 analysis cycles to procure the required settlement rate. At the beginning of the analysis, the slab was evaluated to be at a depth of 17.87 mm. By the last cycle, the slab had sunk into the soil to a depth of 19.054 mm. The maximum strain the concrete endured during the 80 kN load inspection phase was: -33.954 (SG1) and -24.427 (SG2) above the neutral axis, whereas below the neutral axis, the strain values were recorded as 83.88 (SG3) and 51.662 (SG4). Due to the lateral crack, the compressive concrete dealt with lesser strain. Figure 6.6 exposes the stress-strain curve of 20%-TDA-GFRP-2 specimens along with the exact concrete cracking points.

To push the limits further, the test progressed by inducing more pressure on the slab and soil subgrade by proliferating the load to 100 kN. During the loading phase, the slab and soil reactions were monitored. This load incrementation effectuated the subgrade to generate passive cracks surrounding the slab. The pressure exerted on the soil proposed cracks running parallel to the longer span and a lateral crack running perpendicular to both the shorter and longer span was exposed on the top surface of the subgrade. Apart from this the soil surface was flat and did not converge towards the slab. Finally, the slab settled to 25 mm precisely at a load of 97.09 kN. While the load imposed on the slab reached 100 kN, it had pushed through the geocell-reinforced soil to a depth of 26.645 mm on average. Since the soil had shown a significant surface failure pattern, it took 23 repetitive settlement analysis cycles to ascertain the ASTM standards specified settlement rate. At the first cycle,

the slab was evaluated to have sunk 27.342 mm deep into the top surface. Eventually, by the end of the settlement analysis, the slab had consolidated the soil volume beneath it to an average depth of 29.256 mm. During the analysis, the soil crack's width was measured using a scaling device. The shear cracks on the soil at the corner of the slab were scaled to be 2 mm wide, while the other soil cracks were 0.5 mm wide. From figures 6.5 and 6.6, it is apparent that the second crack was pertained by the slab at a load of 93.93 kN. While observing with naked eyes, it was determined that a second crack was induced on the LVDT 5 side. The width of concrete cracks was evaluated using a concrete crack scale sheet. The cracks on the LVDT-2 side were quantified as follows – 1. The first crack was 1.25 mm wide at the lower half of slab depth, whilst it plummeted down to 0.5 mm as the crack elongated above the neutral axis. The first crack had yielded a lateral crack emerging out of the existing crack. The lateral crack was scaled to be 0.5 mm wide and 72 mm long. 2. The second crack width had magnified to 0.75 mm, gradually descending to 0.5 mm as it went into the tension zone. The cracks on the LVDT-5 side were quantified as follows – 1. The first crack ended up with a width of 1.25 mm below the neutral axis and went down to 0.75 mm as it went up. The lateral crack was under the same width of 0.5 mm. 2. The second flexural crack was scaled to be 0.75 mm wide. The 20%-TDA-GFPR-2 concrete slab has exhibited both flexural and lateral failure. Hence, the strain procured by the concrete specimen has grown enormously. The strain on the tension side has magnified almost double the times as the previous load interval, transmitting a value of 147.943 (SG3) and 72.429 (SG4). The average strain on the tension zone was evaluated as 110.186. Similarly, concrete on the compression zone expressed a notable growth in the strain value as shown: -58.785 (SG1) and -44.782 (SG2). The average strain value on the compression

side was evaluated to be 51.783. Finally, the test was terminated as all the required objectives were obtained.



(A)



(B)

Figure 6.7: (A) Soil Crack At Sections A-A1, B-B1, And Lateral Cracks (B) Flexural Cracks of 20%- GFRP-2 Slab on Geocell-Reinforced Soil

6.3.3 Comparison Between Normal Soil and Geocell-Reinforced Subgrade

Response

Figure 6.8 compares the load vs settlement curve of the slab specimens tested at normal soil (NS) and geocell-reinforced soil (GRS) conditions. Although the compaction method was the same and consistent, the relative density of the subgrade has deliberately varied between 48 to 50.5 %, for all five subgrades. Figure 6.8 can be scrutinized in terms of settlement at a particular load interval, cracking load of each slab, and percentage of improvement for both settlement and cracking load. At 20 kN load-interval, all three normal soil and two geocell-reinforced soil subgrades exhibited a stiff soil reaction against the load imposed on them. The normal subgrade utilized to test 20%-TDA-GFRP-1 delivered the stiffest soil response at 20 kN load with a least settlement of 0.9753 mm. Whereas, the other two normal subgrades ended up settling at 3.2316 mm (GFRP-1) and 2.09 mm (10%-TDA-GFRP-1). Geocell-reinforced subgrade was pushed to a settlement of 2.577 (GFRP-2 GRS) and 1.8206 mm (20%-TDA-GFRP-2 GRS). The pressure transferred to the subgrade was negligible, as the slab has a large flat contact surface on the subgrade. Hence, the pressure gets distributed uniformly and absorbed by the soil particles at the top surface. There were no cracks in the soil and concrete at this stage. The GFRP-2 specimens under 20 kN delivered 61.385% and 66.663% lesser strain values than the GFRP-1 specimen on compression and tension zones. Similarly, the 20%-TDA-GFRP-2 specimen produced 50.746% and 26.083% lower strain on compression and tension zones than the one tested on the NS subgrade.

As the load was escalated to 40 kN, all three normal subgrades showed a steep inclination toward the settlement axis. Whilst, both GRS subgrades dominated the pressure transferred

to it and withheld its elastic state, as the geocell had enhanced the stiffness, friction, and bonding between the soil particles to their highest potential under 50% RD. All three NS subgrades transferred to plastic state, as they had generated shear cracks on the soil top surface at all four corners of the slab. The NS subgrades yielded to its plastic state at a load varying between 35 to 40 kN. The NS subgrade utilized for the GFRP-1 Slab produced the steepest settlement curve out of all others. It has settled down to a depth of 13.17 mm. While the remaining two NS subgrade was forced to settle to a depth of 9.8403 mm and 9.9645 mm. The GRS subgrade exposed exceptional load distribution efficiency; hence it derived a linear curve inclination as the load increased. The soil did not lapse any cracks at this load. The geocell soils had consolidated to a settlement of 6.225 mm (GFRP-2) and 5.3475 mm (20%-TDA-GFRP-2). On average, the GRS subgrade governed and restrained the settlement rate by 47.359% less than the NS subgrade. None of the slabs yielded at this load. At 40 kN, the GFRP-2 specimens sustained a strain value of 25.974% and 28.865 % less than the GFRP-1 specimen on compression and tension zones. Similarly, the 20%-TDA-GFRP-2 specimen generated 44.197% and 9.28% lower strain on compression and tension zones than the 20%-TDA-GFRP-1.

From Figure 6.8, It is significant that all subgrades used in this research increased in stiffness following each settlement inspection analysis phase. At every cycle of load incrementation (40, 60, 80, and 100 kN), the soil showed ultimate resistance against a majority of settlement in the initial 5 kN uplift. But further, as the loading proceeds into the remaining 15 kN, each subgrade substantially starts to settle quicker following the same steeper trendline as the previous loading cycle.

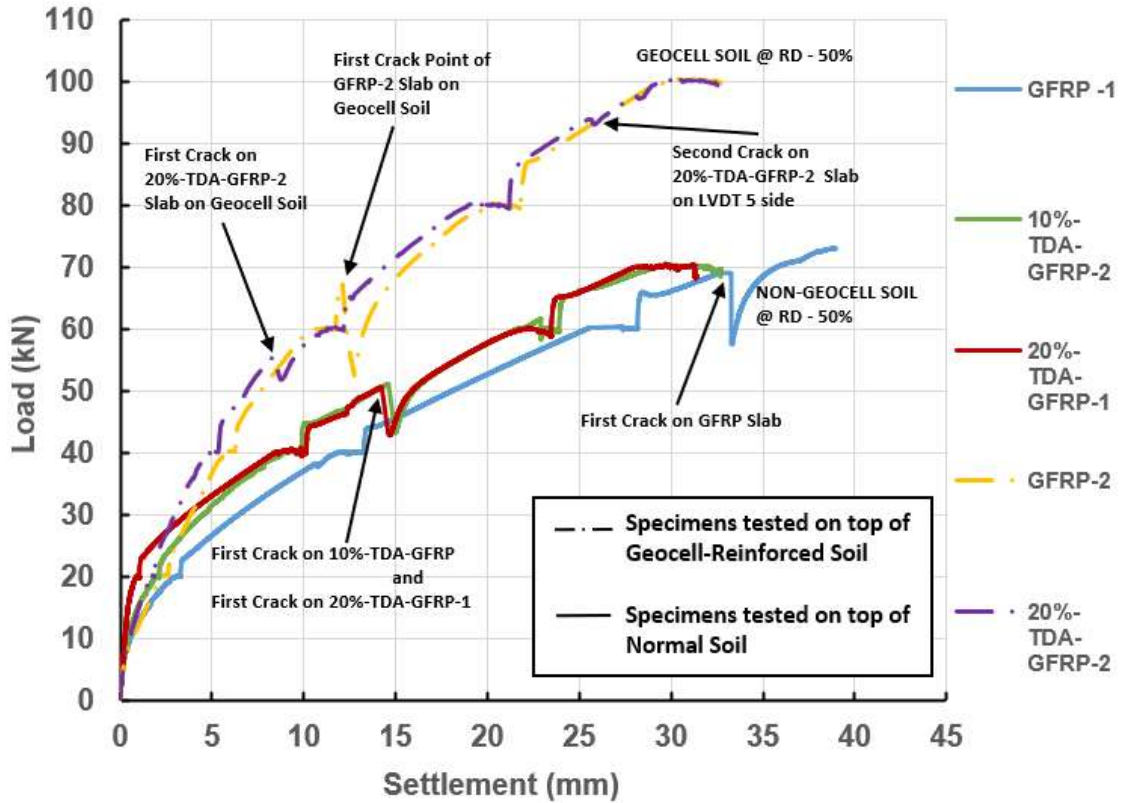


Figure 6.8: Comparison Between Normal and Geocell-Reinforced Soil Monotonic Load Test

The 60 kN load incrementation phase revealed physical and characteristic changes in TDA-reinforced concrete slab specimens. The GFRP-1 specimen had a similar settlement curve to its last loading cycle, as the slab remained elastic. Both 10%-TDA-GFRP-2 and 20%-TDA-GFRP-1 specimens became plastic due to high imposing strain and pressure which yielded a flexural crack at 51.092 and 50.591 kN/m². Thus, the settlement curve drops drastically due to the flexural crack. The GRS subgrades had prodigiously held up its linear elastic stiffness and tight bond between the soil particles, as the predominant amount of pressure was distributed uniformly and absorbed by the geocell present in the soil. Hence the soil top surface GRS subgrades did not yield any cracks throughout the loading phase of 60 kN. The GFRP-2 specimen was intact without yielding any flexural cracks. The 20%-

TDA-GFRP-2 specimen went past its elastic limit by yielding a flexural crack exactly at 55.62 kN. The geocell has moderately influenced the slab's performance as it exposed a 9.04% increase in the yielding point of this specimen. The GFRP-1 specimen had consolidated the soil to 28.133 mm at 60 kN, surpassing the 25 mm threshold. While 10%-TDA-GFRP-2 and 20%-TDA-GFRP-1 specimens on the NS subgrade settled at 22.567 and 21.8398 mm, respectively. The geocell reinforcement improved soil performance under 50% RD by sustaining settlement to 11.673 mm and 11.193 mm for both specimens. Thus, the GRS subgrade gained 52.716% less settlement than NS at 60 kN. During the 60 kN interval, the GFRP-2 specimen had a negligible rate of difference at 5.482% in its strain value on the compressive side, but the tension zone differed by 19.313% from the GFRP-1 specimen. Likewise, the 20%-TDA-GFRP-2 specimen expressed a better strain value on the compressive side which is 42.215% and 25.939% lesser strain was experienced on the tension side.

In the case of NS subgrade condition, the load was further induced to 70 kN load as all three slabs were close to 25 mm depth. During the load incrementation phase, the GFRP-1 slab yielded a flexural crack at 69.141 kN. Finally, after the loading phase, the GFRP-1 specimen ended up settling to a depth of 38.936 mm. The specimens 10%-TDA-GFRP-2 and 20%-TDA-GFRP-1 have pushed the subgrade beyond its passive failure zone to a depth of 32.698 mm and 31.40 mm. All three subgrades exerted several soil cracks such as shear cracks at the slab corner and sides, lateral cracks, passive cracks, and top surface heaving. In the GRS subgrade condition, the GFRP-2 yielded transferring to its plastic state at 67.133 kN. The settlement curve for both slabs was still linear and predominantly elastic till the end of the 80 kN loading phase. For both slab specimens, around 75 to 79 kN soil

particles at the corner of the slab yielded by developing shear cracks. The geocell has reinforced the soil particles, increased the bonding strength, and magnified elastic load-bearing capacity (soil cracking point) by 53.846% more than the NS subgrade. At 80 kN both the slabs tested on GRS subgrade have deviated the soil particles and consolidated the soil to a depth of 19.661 mm and 19.054 mm. Thus, the subgrade had shifted from an elastic deformation to plastic deformation by causing the pressure imposed on the soil to exceed the precompression stress leading to soil degradation, which is instigated by aggregate failure and irreversible loss of pore air volume. The test proceeds further by increasing the load to 100 kN for the GRS subgrade. Figure 6.8, highlights that the GFRP slab sustained the loading condition without any additional cracks, whilst it can be depicted that the 20%-TDA-GFPR-2 slab yielded a second flexural crack at 93.939 kN. The geocell in the subgrade had effectively sustained both GFRP-2 and 20%-TDA-GFPR-2 specimens to 92.6 and 97.09 kN from consolidating to a depth of 25 mm. At 100 kN the top surface of the GRS subgrade has additionally yielded one lateral crack running perpendicular to the longer span on both sides of the slab. Even though the subgrade was reinforced with geocell, it is significant that the subgrade has generated passive failure as high pressure was imposed on it. However, the geocell has predominantly distributed the pressure evenly throughout the subgrade which has technically negated the soil from converging towards the slab. Eventually, the Geocell produced comprehensive results by significantly enhancing the soil bearing capacity by 40.776%(313.787 kN/m²), whilst the NS subgrade had projected a bearing capacity of 222.898 kN/m². Hence, the geocell widened the pressure distribution web, unified the soil particles together, augmented the uniform pressure distribution pattern, integrated soil particles together, and improvised the soil

particles bonding strength to aggrandize the bearing capacity of the subgrade under the same 50% relative density.

6.4 Conclusion

This chapter extensively scrutinizes the experimental investigation on the influence of geocell reinforcement in the sandy soil subgrade toward the load vs settlement rate, soil settlement and cracking load, top surface cracking pattern, and subgrade bearing capacity. Alongside it also analyzes the characteristic changes in the concrete slab specimens such as variation in concrete cracking load, and difference in strain value attained by the specimen.

The geocell has infused its positive impact on the subgrade while testing by prodigiously aggrandizing the bearing capacity of the 50% RD subgrade about 40.776% excessive than the NS subgrade. Evidently, the subgrade responded by expressing an impressive reduction in the load vs settlement rate as follows: 47.3599% @ 40kN, 52.716% @ 60 kN, and at 80 kN it sustained the slabs 41.117% lesser settlement than NS. Subsequently, it took 92.6 and 97.02 kN load for the subgrade to deform to a depth of 25mm and it took 100 kN for it to attain 29.377 mm of average settlement.

The subgrade top surface instigated only shear cracks elongating away from the slab corners at load ranging between 78 to 80 kN. Thus, the geocell has proliferated the switch between Linear elastic deformation to plastic deformation of the subgrade by 53.846% greater than the soil cracking point of the NS subgrade. The GRS subgrade had exerted shear cracks and several perpendicular and lateral cracks on all sides of the slab. One of the prominent phenomena analyzed experimentally was that the geocell prohibited the soil mass from bulking up and heaving of top surface towards the slab due to passive zone soil

pressure. The geocell significantly Magnifies the soil performance, whilst it shows negligible influence at the slab cracking load. The 20%-TDA-GFRP-2 specimen exerted a flexural crack at 55.6236 kN load which is 9.04% more than the same specimen tested on NS. The GFRP-2 specimen had a cracking load of 67.133 kN which is negligibly lesser than that of the GFRP-1 Specimen. As the soil stiffness intensified, eventually the pressure transferred by the specimens augmented significantly causing the specimens to experience lesser strain while tested on top of the GRS subgrade. Thus, geocell ameliorates soil performance by aggrandizing soil particle bonding, stiffness, elastic loading limit, and bearing capacity by expanding the pressure distribution pattern and uniformly distributing the pressure induced on the subgrade.

CHAPTER-7 CONCLUSION

This research work has been primarily focused on the intricate interaction between the slab-on-grade specimens reinforced with GFRP rebars with a partial amount of tire derivative aggregates, the settlement rate at normal sandy subgrade, and low-density polyethylene (LDPE) GF30 geocell reinforced subgrade, considering the parametric changes that were emphasized by the soil structure with concern to the subgrade type. It was important to analyze and understand the effect of the irregular shape and non-linear distribution of TDA particles and the parametric changes that evolved in the concrete slab. Two different volumes (10% and 20%) were used to replace the coarse aggregate in the mix design. Seven concrete slabs were designed and constructed in the lab. To achieve the required motive of this study, each specimen was examined under a monotonic load on top of two different subgrade conditions to analyze the impact of TDA, GFRP rebars, and geocell reinforcement. A custom-made soil tank of 2.75m X 2.25m X 1.85 M was used to formulate the soil subgrade which will be the base of our test apparatus. Similarly, a custom-made hydraulic actuator was suspended vertically to impose the load on the slab. A fixed test procedure was followed with iterative load incrementation to examine the response of concrete slab specimens and soil subgrade reaction. Plaxis 3D FEM analysis software was utilized to validate the soil subgrade data obtained through lab testing. Six different Plaxis 3D models were developed, each one having different soil parameters based on the six differing relative densities of the soil subgrade.

The plate load test outcomes indicate the significant benefits of employing geocell reinforcement in soil. Compared to normal soil, the geocell-reinforced soil evinces a notable improvement in load vs settlement behavior, maintaining a linear elastic state under

imposed load. This reinforcement technique notably enhanced the soil's load-bearing capacity by 38.97% and minimized cracks by 95%, illustrating its effectiveness by stiffening the soil subgrade, bonding the soil particles tightly, enhancing the elastic limit, enlarging the pressure distribution pattern, and distributing pressure uniformly.

Additionally, observations on different slab types revealed passive crack patterns in the non-geocell sandy soil subgrade, emphasizing the importance of soil structure reinforcement in preventing subgrade failures like Passive soil expansion and top surface heaving surrounding the slab, and development of shear, lateral, and perpendicular cracks. Incorporating TDA at different percentages in the slabs manifested variations in concrete cracking loads and escalation of strain values compared to GFRP slabs. In contrast to the GFRP-1 slab, which generated a flexural crevice at a load of 69.141 kN, the 10%-TDA-GFRP-2 slab fissured at a load that was 26.10% lower, and the 20%-TDA-GFRP-1 slab snapped at 26.82% lesser load than GFRP-1. At 70 kN, the strain on the tension region of the 10%-TDA-GFRP-2 and 20%-TDA-GFPR-1 slabs increased by 28.764% and 18.792%, respectively, in comparison to the GFRP-1 slab. Thus, TDA emphasizes the potential to induce flexural cracks a bit earlier than the conventional concrete slab, whilst TDA enhances the structural integrity, ductility, flexibility, and diminishes the emergence of shrinkage cracks. Furthermore, the validation of Plaxis 3D models against experimental field-tested subgrade results highlights their reliability in evaluating the soil parameters and settlement rates, emphasizing their use for assessing geocell-reinforced soil parameters.

When investigated with slab specimens, geocell soil structure has demonstrated significant improvements in the subgrade's performance, specifically enhancing the bearing capacity

of the subgrade with 50% relative density by approximately 40.776 % over the normal subgrade. This improvement was accompanied by a substantial reduction in settlement rates under several load increments. Furthermore, the subgrade reinforced with geocells demonstrated uniform pressure distribution capacities prior to approaching deformation limits. Shear cracks were predominantly perceived on the surface of the subgrade, originating from the corners of the slab, within a load range of 78 to 80 kN. This observation suggests that the geocell effectively postpones the shift from linear elastic to plastic deformation by 53.846% greater than the soil cracking point of the NS subgrade. Furthermore, the geocell mitigated soil mass bulking and convergence towards the slab, by reducing passive zone soil pressure. However, the influence of the geocell on the slab cracking load was found to be minimal. When it comes to slab performance, the 20%-TDA-GFRP-2 specimen exerted a flexural crack at a load which was 9.04% higher than the same specimen tested on conventional soil. However, the GFRP-2 specimen displayed a slightly lower cracking load (67.133 kN) compared to the GFRP-1 specimen. As a result, there was a significant increase in the pressure transferred by the specimens. Which in turn, leads to a reduction in the strain experienced by the specimens when subjected to heavy loading conditions. To summarize, it is evident that although the 20%-TDA-GFRP slab specimen had a 48.49 % drop in compressive strength to normal concrete mix and 19.63 % lesser strength than 10%-TDA concrete mix, it exhibited exceptional results outperforming the 10%-TDA-GFRP specimen behavior. Hence the 20%-TDA concrete mix is an efficient concrete mix that can be utilized for small warehouses, workshops, parking lots, garages, footpaths, pavements, driveways, and other non-structural elements.

7.1 Future Research Works

1. Conduct further experimental analysis by subjecting these 10% and 20 %-TDA-GFRP specimens to cyclic load test analysis under both normal soil and geocell-reinforced subgrade conditions.
2. Changing the TDA composition with the coarse aggregate to (30% and 40%) and examining the Specimens with static and cyclic load tests on both subgrade conditions
3. Developing a 3D FEA simulation using Plaxis 3D to further investigate and validate the static and cyclic load analysis on both subgrade conditions.

APPENDIX A SOIL SUBGRADE IN-SITU FIELD TEST

A.1 Introduction

The soil subgrade was examined using three different testing methods based on the ASTM standards. Initially, each soil surface in the soil tank will undergo an in-situ sand cone test at least in two spots following ASTM D1556/D1556M standard. A huge soil sample was collected from the soil tank and was investigated using the laboratory compaction testing method based on ASTM D698 standards to determine its maximum dry density, minimum dry density, and optimum water content. Based on the soil parameters obtained from these testing methods the relative density of each soil layer was calculated. The testing methodology has been briefly explained in section 3.7 (Subgrade test methodology) in this report.

A.2 Soil Parameter Calculation Methodology

Every soil layer in the soil tank has gone through a series of iterations of sand cone test, moisture content test, and relative density calculations to determine the RD value of the soil layer. The calculation has been done utilizing the formulas mentioned below.

Ith Iteration – (Sand Cone Test and Moisture Content Test)

Sand Cone Test – Step-wise Calculation

Weight of Container and silica sand in it = 7200 gm / 7.2 Kg

Weight of container alone = 720 gm

To acquire optimum values for each soil layer through the in-situ sand cone test, the container was weighed separately and filled up completely. It weighs 7200 gm with silica sand in it. This weight was kept constant for all the iterations. The sand cone was inverted on a flat surface with a plastic sheet underneath it, the nozzle was opened to evaluate the

weight of silica sand filling the cone alone. It was repeated three times, and an average weight was considered as the weight of silica sand filling the cone alone.

$$\text{Weight of silica sand in the cone alone AVG } W_C = 1684 \text{ gm}$$

As per the ASTM standard, a spot was chosen on the soil layer, and the circular plastic base plate was placed on top of that spot. The soil within the inner circle was removed spherically up to a depth of 10 to 12 cm and collected in a zip-lock bag. The sand cone was placed on the circumferential edge of the inner circle and the test was performed. The silica sand container weight and the weight of the wet soil obtained were recorded.

$$\text{Weight of wet soil obtained from the soil tank } W_s = 2760 \text{ gm}$$

Weight of silica sand left in the container after

$$\text{Filling the hole and cone } W_{\text{CONT}} = 3130 \text{ gm}$$

$$\text{Weight of silica sand in the hole and cone} = 7200 - W_{\text{CON}} = 7200 - 3130$$

$$W_{(H+C)} = 4070 \text{ gm}$$

$$\text{Weight of silica sand in the hole alone } W_H = W_{(H+C)} - W_C$$

$$W_H = 4070 - 1684 = 2386 \text{ gm}$$

$$\text{unit weight of silica } \gamma_{\text{SILICA}} = 1.44 \text{ gm/cm}^3$$

$$\text{Volume of hole in the soil tank } V_{\text{hole}} = \frac{W_H}{\gamma_{\text{SILICA}}}$$

$$V_{\text{hole}} = 2386/1.44 = 1656.944 \text{ cm}^3$$

$$\text{Wet unit weight of soil in the soil tank} = \frac{W_s}{V_{\text{hole}}} = 2760/1656.944$$

$$= 1.665717 \text{ gm/cm}^3$$

$$= 16.340 \text{ kN/m}^3$$

$$\text{Dry unit weight of soil} = \frac{\gamma_{\text{wet}}}{1 + \frac{w}{100}} = \frac{1.665717}{1 + \frac{4.6817}{100}} = 1.59122$$

gm/ cm³

$$= 15.609 \text{ kN/m}^3$$

To calculate the moisture content of the soil layer, a small sample of sand particles is measured in two small steel containers which were used to place the sample inside the

oven. The moisture content test is implemented following ASTM D2216. The table A.1 Comprises the moisture content ω calculation method.

Table A.1: Moisture Content Calculation Method

Container no	3	2
Container self-weight W_{SW}	45.2	45.7
Container + wet soil weight $W_{WS+CONT}$	262.2	255.7
Container + dry soil weight $W_{DS+CONT}$	252.4	246.4
Mass of water W_{Water}	$= W_{WS+CONT} - W_{DS+CONT}$ $= 262.2 - 252.4 = 9.8 \text{ gm}$	$= W_{WS+CONT} - W_{DS+CONT}$ $= 255.7 - 246.4 = 9.3 \text{ gm}$
Mass of dry soil W_{DS}	$= W_{DS+CONT} - W_{SW}$ $= 252.4 - 45.2 = 207.2 \text{ gm}$	$= W_{DS+CONT} - W_{SW}$ $= 246.4 - 45.7 = 200.7 \text{ gm}$
Moisture content ω	$= \frac{W_{water}}{W_{ds}} \times 100$ $= (9.8/207.2) \times 100$ $= 4.72 \%$	$= \frac{W_{water}}{W_{ds}} \times 100$ $= (9.3/200.7) \times 100$ $= 4.63\%$
Avg Moisture content ω_{AVG}	4.68 %	

Laboratory Compaction Test of Sandy Soil

A substantial amount of soil is collected from the total mass of soil present in the tank. The laboratory compaction test was conducted according to ASTM D698. The testing methodology has been briefly explained in section 3.7.2. According to this methodology, the derived soil mass was oven-dried for 48 hours at 105°C. The soil is tested under different moisture contents (5%, 7%, 11%, 13%, 15%, and 19%) to attain the corresponding Maximum dry unit weight for those particular moisture content to establish a relationship

between the dry unit weight and the molding water content for the soil. Do not reuse the same soil sample for other moisture contents (ω).

The formulas used to determine the dry unit weight and moisture content were as follows:

Determine the dry mass of test fraction $M_{\text{DRY}} = \frac{M_m}{1 + \frac{\omega}{100}}$

Moist density of soil sample $\gamma_m = K \times \frac{(M_T - M_{CM})}{V_{CM}}$

Dry density of the soil sample tested $\gamma_D = \frac{\gamma_m}{1 + \frac{\omega}{100}}$

From the data attained with the help of these formulas through a series of compaction tests under different moisture content, a graph can be plotted to represent a curvilinear relationship known as the compaction curve. From the graph shown in Figure A.1, the maximum dry unit weight and the optimum moisture (ω_{Optimum}) content can be proclaimed.

The Maximum dry unit weight of soil $\gamma_{D\text{Max}} = 1.77 \text{ gm/cm}^3$

The Optimum Moisture Content $\omega_{\text{Optimum}} = 15.2$

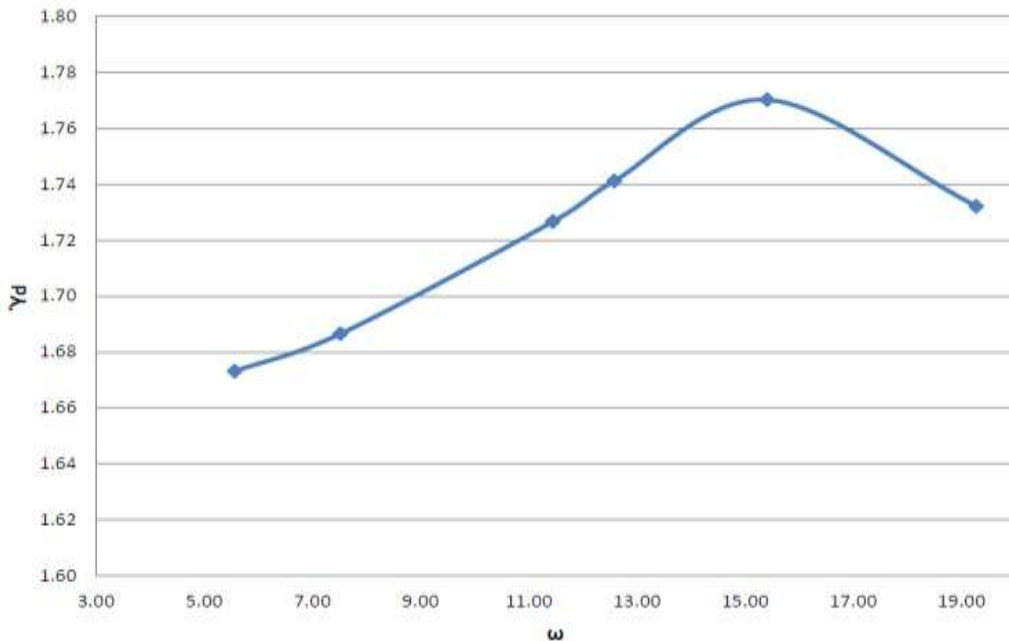


Figure A.1: Compaction Test Result Curve

The soil subgrade was oven-dried at 105°C for 48 hours before testing it. The minimum dry unit weight is evaluated using the mold, water, and oven-dry soil sample. Initially, the weight of the empty mold is measured, again the mold is entirely filled with sand and weighed without any compaction. The volume of the mold is calculated. Depending on these terms the minimum dry unit weight is measured.

$$\text{Weight of container} = W_{\text{CONT}} = 2042.8 \text{ gm}$$

$$\text{Weight of container and dry soil} = W_{\text{CONT} + \text{D}} = 9097 \text{ gm}$$

$$\text{Diameter of the container} = d = 19.6 \text{ cm}$$

$$\text{Height of the container} = h = 16.1 \text{ cm}$$

$$\text{Volume of container} = V_{\text{CONT}} = \frac{\pi}{4} d^2 h = \frac{\pi}{4} 19.6^2 \times 16.1 = 4857.66 \text{ cm}^3$$

$$\text{Weight of dry soil} = W_{\text{CONT} + \text{D}} - W_{\text{CONT}} = 9097 - 2042.8$$

$$W_{\text{D}} = 7054.2 \text{ gm}$$

The minimum dry unit weight can be calculated using these data.

$$\text{Minimum dry unit weight} \quad \gamma_{\text{DMIN}} = \frac{W_{\text{D}}}{V_{\text{CONT}}} = \frac{7054.2}{4857.66}$$

$$\gamma_{\text{DMIN}} = 1.452 \text{ gm/cm}^3$$

These parameters were determined to derive the relative density of the soil layer. The relative density is evaluated for each layer to maintain the compaction of the soil layer between 45 to 50% to replicate a medium soil subgrade. The relative density (Rd) is ascertained based on this formula.

$$\text{Rd} = \frac{\gamma_{\text{dmax}} (\gamma_{\text{d}} - \gamma_{\text{dmin}})}{\gamma_{\text{d}} (\gamma_{\text{dmax}} - \gamma_{\text{dmin}})}$$

Table A.2: Sand Cone Test and RD Results of Soil Subgrade

Slab Type	Soil Type	Layer of Soil	γ_{WET} (gm/cm³)	ω_{Avg} %	γ_{DRY} (gm/cm³)	RD %
NS	CS	3 rd Layer	1.72	3.69	1.66	69.91
		2 nd Layer	1.71	3.64	1.65	67.59
		1 st Layer	1.72	3.73	1.66	68.03
NS	10%-TDA-GFPR-1	3 rd Layer	1.72	3.91	1.66	69.74
		2 nd Layer	1.73	3.98	1.66	71.05
		1 st Layer	1.74	4.16	1.67	70.59
NS	GFPR-1	3 rd Layer	1.67	4.78	1.59	49.87
		2 nd Layer	1.67	4.71	1.60	52.65
		1 st Layer	1.66	4.68	1.59	48.69
NS	10%-TDA-GFPR-2@50	3 rd Layer	1.66	4.36	1.59	51.18
		2 nd Layer	1.67	4.70	1.60	51.57
		1 st Layer	1.66	4.22	1.59	49.82
NS	20%-TDA-GFPR-1	3 rd Layer	1.68	4.78	1.60	52.60
		2 nd Layer	1.67	4.50	1.59	51.20
		1 st Layer	1.66	4.61	1.59	50.28
GRS	GFPR-2	3 rd Layer	1.66	4.55	1.59	49.89
		2 nd Layer	1.67	4.59	1.60	52.01
		1 st Layer	1.67	5.01	1.59	50.36
GRS	20%-TDA-GFPR-2	3 rd Layer	1.69	5.52	1.60	52.67
		2 nd Layer	1.66	4.16	1.60	51.79
		1 st Layer	1.66	4.49	1.59	50.11

APPENDIX B SIEVE ANALYSIS OF TDA

B.1 Introduction

The sieve analysis for TDA size distribution was conducted according to ASTM C136 standards by Ahmad M. Abu Abdo and Hany El Naggar for their study on “Properties and Behavior of Rubberized Concrete Enhanced with PVA Fibers”. Thus, the sieve analysis for TDA was done as per the same ASTM C136 standard and test procedure. Type GU Portland cement, coarse aggregate, and fine aggregated were sourced from a construction material local dealer, whereas the tire derivative aggregate was obtained as scarp shredded particles with irregular shape and size along with rusted steel wires. Thus, the TDA was cleaned properly, all the rusted steel wires were removed, and the bigger particles were cut to scale it under $\frac{3}{4}$ of an inch. The clean TDA particles were then collectively examined through sieve analysis to segregate the particles that fall under $\frac{3}{4}$ inch size for concrete mix.

B.2 TDA Particle Size Distribution

Initially, the TDA particles were cleaned by removing the dirt and rust wires from all the particles that were segregated for sieve analysis. Once a sufficient quantity of TDA particles was collected, which were cut under the size of $\frac{3}{4}$ th of an inch, a few sets of TDA samples weighing around 5 kg from the segregated TDA particles were examined according to ASTM C136 standard. The required sieve of sizes (3/4-inch, 3/8-inch, No.4, and pan) was selected to examine the TDA particles to attain the required particle size distribution data. The sieves were arranged in the size descending order starting from $\frac{3}{4}$ inch to pan. The TDA samples were weighed and placed on the top sieve. The whole rack of sieves was placed in the mechanical vibrating apparatus for seven minutes. The particles retained in the corresponding sieve sizes were weighed and recorded. The same procedure

was followed for all sets of TDA samples, and the test data was recorded. All the test data proclaimed at each iteration were added together concerning the retained sieve size to combine into a whole single test data. Figure B.1 shows the sieve analysis testing method.



Figure B.1: TDA Sieve Analysis

The combined test data were then used to generate a logarithmic particle size distribution sieve analysis graph. Figure B.2 depicts the particle size distribution graph.

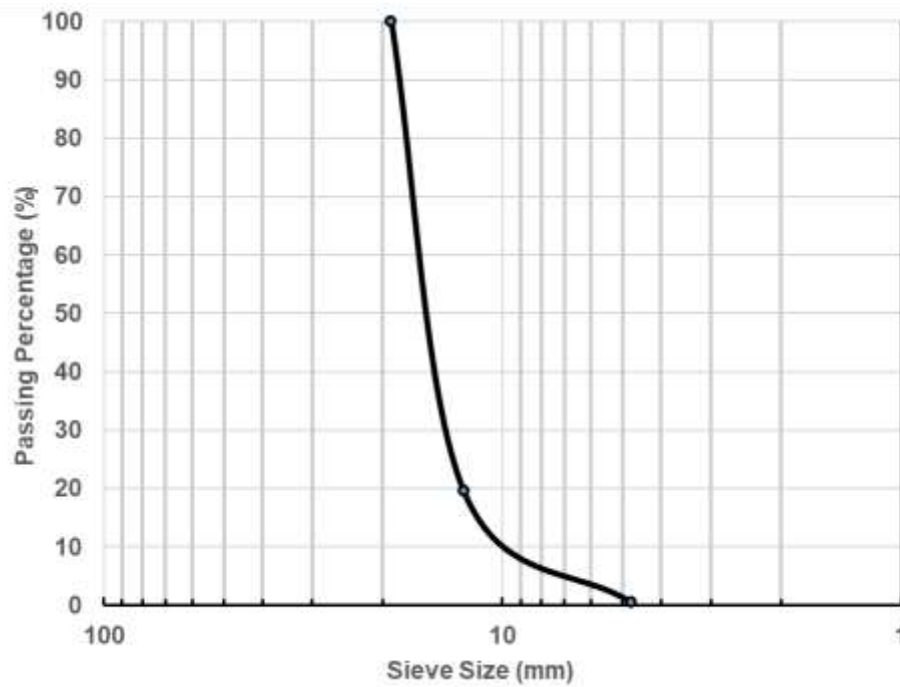


Figure B.2: Particle Size Distribution of TDA

APPENDIX C COMPRESSIVE STRENGTH OF CONCRETE CYLINDER

C.1 Introduction

Initially, three cylinders were cast for each mix design, to validate if the control specimen mix design yielded the required strength of 30 Mpa, and check the strength generated by 10%-TDA and 20%-TDA mix. Furthermore, three to four cylinders of size (100mm X 200mm) were cast along with each slab mix. Those cylinders were moist cured for the first seven days, and then for the rest of the days, they were left to air cure along with the corresponding slab specimens. As the slab specimens were tested, the cylinders of the respective slabs were tested for compression test on the same day.

C.2 Concrete Cylinder Compressive Test Results

Figure C.1 and Table C.1 depict the compressive strength results of concrete cylinders of different mix designs tested on an ultimate testing machine (UTM). The Compression test was executed according to ASTM C39/C39M standards.

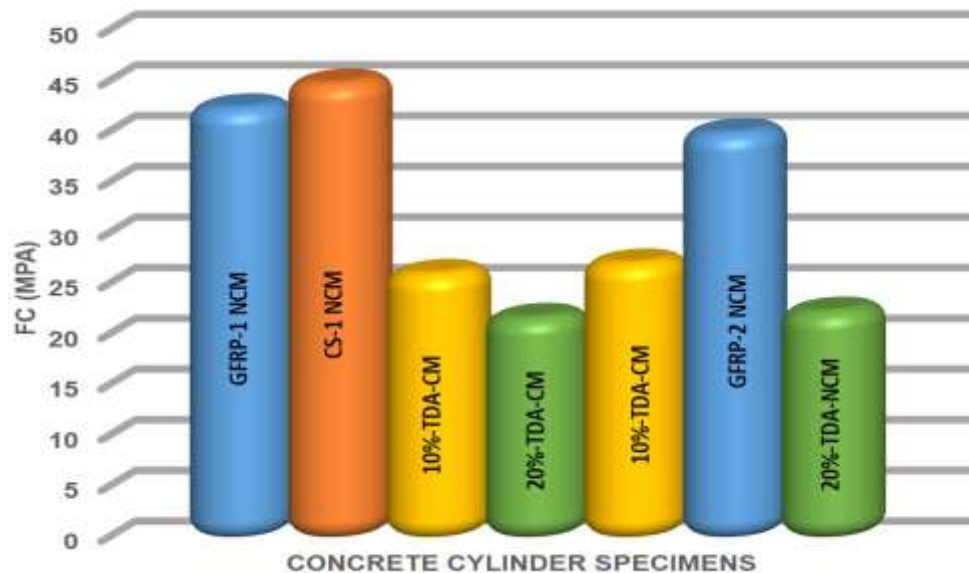


Figure C.1: Compression Test Results

Table C.1: Compression Strength of Concrete Cylinders with Different Mix Designs

Concrete Mix Type	Number of Cylinders	Cylinder size (mm)		Compressive strength F_{ck} (Mpa)	Average Compressive Strength F_{ck}	Cracking Type	
		ϕ	Height				
GFRP-1 NCM	3	1 st Cyl	101.2	201.5	40.33	42.63	Shear crack (Brittle Failure)
		2 nd Cyl	101.7	202	44.27		
		3 rd Cyl	103	202.5	43.29		
CS-1 NCM	3	1 st Cyl	102.5	201	45.37	45.19	Shear crack (Brittle Failure)
		2 nd Cyl	102	202	44.60		
		3 rd Cyl	101.7	203.2	45.62		
10%-TDA-CM	3	1 st Cyl	101.5	201.7	29.40	26.29	Columnar vertical and hairline crack (ductile failure)
		2 nd Cyl	102.3	202.5	27.04		
		3 rd Cyl	102.5	203	22.44		
20%-TDA-CM	4	1 st Cyl	101.8	202.4	21.12	21.95	Columnar vertical and hairline crack (ductile failure)
		2 nd Cyl	102	203.1	20.79		
		3 rd Cyl	103	201.8	22.44		
		4 th Cyl	102.5	203.6	23.48		
10%-TDA-CM	3	1 st Cyl	102.7	201.8	28.36	27.32	Columnar vertical and hairline crack (ductile failure)
		2 nd Cyl	103.4	203.8	24.47		
		3 rd Cyl	101.6	202.6	29.13		
GFRP-2 NCM	3	1 st Cyl	101.7	204.2	39.06	40.17	Shear crack (Brittle Failure)
		2 nd Cyl	102.2	203.3	40.49		
		3 rd Cyl	102.6	205.8	40.98		
20%-TDA-CM	4	1 st Cyl	101.7	203.1	23.53	22.57	Columnar vertical and hairline crack (ductile failure)
		2 nd Cyl	102.5	204.2	21.45		
		3 rd Cyl	102.7	203.1	23.70		
		4 th Cyl	101.6	205.3	21.61		

It is evident that the addition of TDA to the concrete mix has reduced the compressive strength of the concrete drastically. The 10%-TDA replacement had relinquished the concrete strength to plummet down 26.299 Mpa and 27.324 Mpa, which is 41.66% and

39.393% less than the Control specimen normal concrete mix (NCM). The addition of 20% TDA made the concrete more ductile and yielded a strength of 21.96 Mpa and 22.578 Mpa. 20% TDA specimens exhibited more than 50 % reduction in compressive strength. Both 10% and 20% TDA cylinder specimens exhibited ductile behavior, exposed columnar vertical cracks, and hairline cracks. All the NCM cylinders developed shear cracks at their peak load due to their brittle behavior. TDA concrete mixtures showed predominantly extraordinary performance in the slab-on-grade specimens while exposed to a monotonic load test. Figure C.2 shows the crack pattern in different cylinder specimens.



Figure C.2: Cracked Cylinder Specimens

APPENDIX D SETTLEMENT INSPECTION CURVE AT LOAD- INTERVAL

D.1 Introduction

At every load interval, the settlement rate of the slab was inspected for every slab specimen tested on both soil subgrade conditions. The load was intensified with a 20 kN increment rate until the slab settled to a depth of 25 to 30 mm. At each load interval (20, 40, 60, 80, 100) kN, the slab was left to settle under that load with leverage to oscillate up to 0.2 kN (20 ± 0.2 kN). During the load interval, the settlement rate of the slab was assessed critically for every 3-minute interval. This assessment prevailed till the rate depreciated to 0.03 mm/min at a 3-minute interval for two consecutive cycles. The settlement inspection analysis during each load interval was executed according to the ASTM-D1196 standard.

D.2 Settlement Rate Analysis

During every load interval, the settlement value transmitted by each LVDT was noted precisely along with the load for consecutive 3-minute intervals. The settlement rate was validated against the previous reading for each LVDT. This was repetitively done for several iterations until the required settlement rate of 0.03 mm/min for a couple of 3-minute intervals was attained. As the load surpasses 40 kN, the number of iterations for achieving the required rate will increase. Table D.1 shows that the normal soil subgrade had to undergo several inspection iterations to proclaim the settlement rate as per ASTM specifications. The soil particles of this NS subgrade with 50% RD were dispersing away due to the passive dispersion force exerted by the soil pressure distribution. Conversely, the geocell-reinforced subgrade with 50% RD exposed a lesser soil particle dispersion rate since the soil particles were confined tightly together with lesser air voids. Hence, the

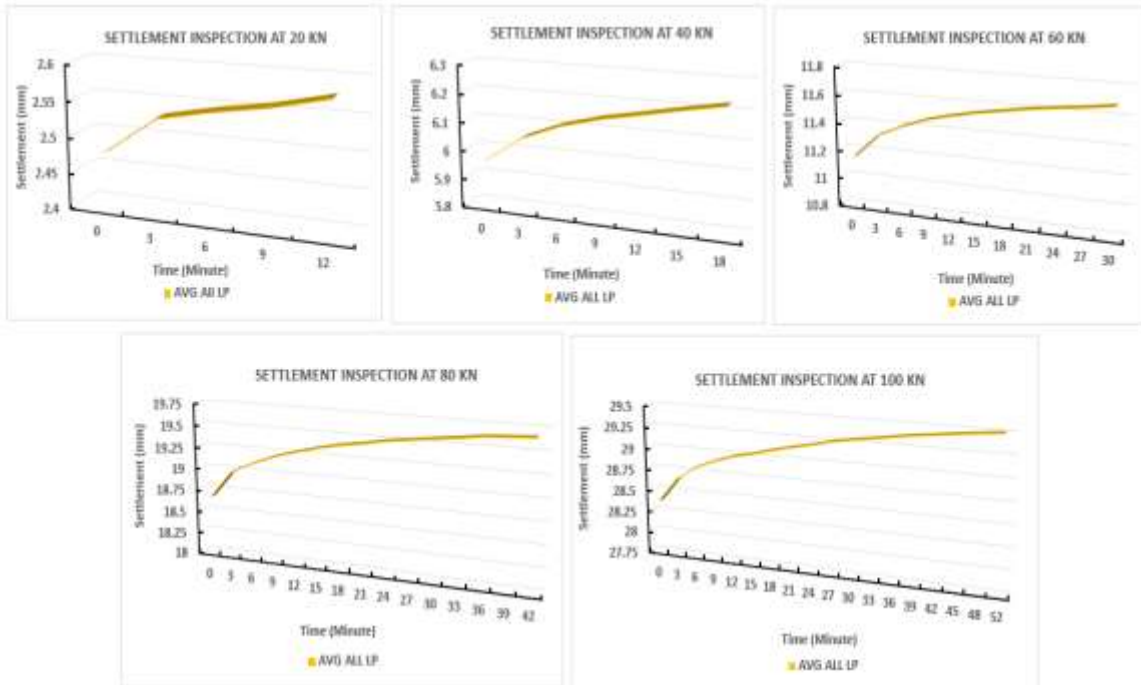
settlement rate assessment took a smaller number of iterations to procure the ASTM-specified rates.

Table D.1: Settlement Rate Analysis for Each Slab-On-Grade Specimen

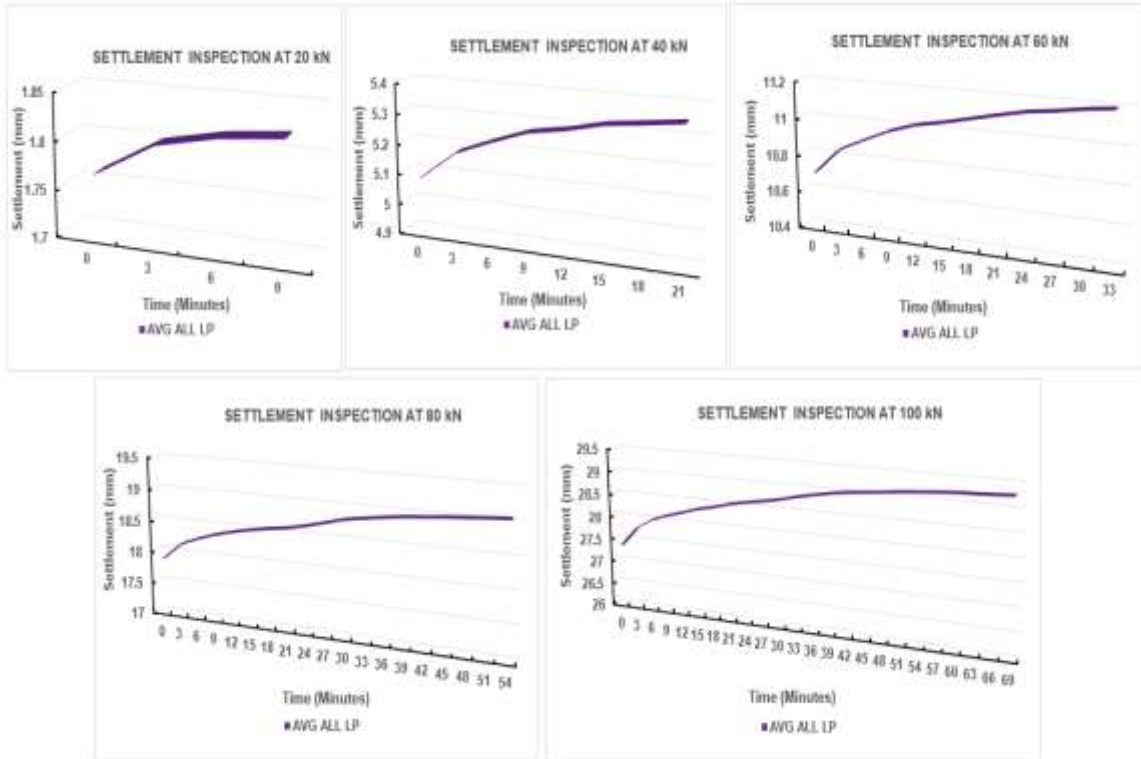
Load Interval	Settlement Analysis Iteration	Settlement of each slab-on-grade Specimen (mm)z				
		GFRP-1	10%-TDA-GFRP-2	20%-TDA-GFRP-1	GFRP-2	20%-TDA-GFRP-2
@ 20 kN	1 st Iteration	3.006	1.940	0.878	2.475	1.763
	Last Iteration	3.231	2.090	0.975	2.577	1.820
@ 40 kN	1 st Iteration	12.618	9.225	9.382	5.961	5.084
	Last Iteration	13.171	9.840	9.964	6.225	5.347
@ 60 kN	1 st Iteration	27.557	22.079	20.972	11.152	10.698
	Last Iteration	28.113	22.567	21.839	11.673	11.193
@70 kN	1 st Iteration	37.688	29.592	28.122	-	-
	Last Iteration	38.936	30.510	29.179	-	-
@ 80 kN	1 st Iteration	-	-	-	18.667	17.876
	Last Iteration	-	-	-	19.661	19.054
@ 100 kN	1 st Iteration	-	-	-	28.371	27.342
	Last Iteration	-	-	-	29.449	29.256

The GFRP-2 and 20%-TDA-GFRP-2 Specimens were examined on top of the geocell-reinforced soil subgrade. Hence the subgrade had an enhanced pressure distribution pattern and better bonding and friction between the soil particles, enabling it to withstand up to 100 kN load. At 60 kN load, the specimens tested on the NS subgrade took around 8 to 10

iterations to attain the required rate of settlement. Whereas the specimens tested on the GRS subgrade took 10 and 11 iterations to proclaim it. As the load magnified to 80 and 100 kN, the GRS subgrade exposed shear cracks on the soil top surface at all corners of the slab. Hence, the subgrade yielded to its plastic state. Therefore, it enhanced the dispersion rate of the soil particles, significantly increasing the iterations to secure the required settlement rate of 0.03 mm/min. At 80 kN it took 14 iterations for GFRP-2 and 18 cycles for 20%-TDA-GFRP-2 specimen. At 100 kN the subgrade had developed several lateral and shear cracks on the top surface, but it did not have any passive topsoil bulking and heaving around the slab. The geocell had optimized the pressure distribution pattern and made it wider causing the soil particles to evade outwards rather than bulking upwards. Hence, it took 17 iterations for the GFRP-2 specimen and 23 iterations for the 20%-TDA-GFRP-2 specimen to proclaim the settlement rate assigned by ASTM standard. Figure D.1 shows the settlement inspection curve for GFRP-2 and 20%-TDA-GFRP-2 specimens.



(A)



(B)

Figure D.1: Settlement Curve Graph (A) GFRP-2 (B) 20%-TDA-GFRP-2

REFERENCES

ACI 211.1 – Standard Practice for Mix Design of Concrete.

ACI 360R – Design of Slab on Grade

ACI 440.1R-15 Guide for Design and Construction of Structural Concrete Reinforced With Fiber-Reinforced Polymer (FRP) Bars.

Adams, M.T.; Collin, J. G. 1997, Large Model Spread Footing Load Tests on Geosynthetic Reinforced Soil Foundations Journal of Geotechnical Engineering DOI: [https://doi.org/10.1061/\(ASCE\)1090-0241\(1997\)123:1\(66\)](https://doi.org/10.1061/(ASCE)1090-0241(1997)123:1(66))

Ahmad M. Abu Abdo; Hany El Naggar (2022) Evaluation of the Incorporation of Tire-Derived Aggregates (TDA) in Rigid Pavement Mix Designs DOI: <https://doi.org/10.3390/su141811775>

Ahmed Mahgoub, Innovative Applications of Tire Derived Aggregate (TDA) For Buried Pipes and Culverts. (203-206). DOI: [http://dx.doi.org/10.1061/\(ASCE\)PS.1949-1204.0000466](http://dx.doi.org/10.1061/(ASCE)PS.1949-1204.0000466)

Ahmed Mahgoub; El Naggar, H.; Coupled TDA–Geocell Stress-Bridging System for Buried Corrugated Metal Pipes. DOI: [https://doi.org/10.1061/\(ASCE\)GT.1943-5606.0002279](https://doi.org/10.1061/(ASCE)GT.1943-5606.0002279)

Al-Qadi IL, Hughes JJ (2000) Field Evaluation of Geocell Use in Flexible Pavements. DOI: <https://doi.org/10.3141/1709-04>

Al-Zahrani M. M.; Rahman M. K.; Fasil M.; Al-Abduljabbar S.; Nanni A.; Al-Osta M. A. Al-Gahtani H. J. (2023). Punching shear capacity of GFRP bar-reinforced concrete slabs-on-ground. Engineering Structures, 289. DOI: <https://doi.org/10.1016/j.engstruct.2023.116285>

ASTM C29/C 29M - Standard Test Method for Bulk Density “Unit Weight” and Void in Aggregate

ASTM C136 – Standard Test Method for Sieve Analysis of Fine and Coarse Aggregates

ASTM C39/C39M – Standard Test Method for Compressive Strength of Cylindrical Concrete Specimen

ASTM D698 – Standard test methods for Laboratory Compaction Characteristics of Soil Using Standard Effort (12400ft-lbf/ft³ (600 kN-m/m³))

ASTM D854-23 Standard Test Method for Specific Gravity of Soil Solids by the Water Displacement Method

ASTM-D1194 Standard Test Method for Bearing Capacity of Soil for Static Load and Spread Footings

ASTM-D1196 Standard Test Method for Nonrepetitive Static Plate Load Tests of Soil and Flexible Pavement Components, for Use in Evaluation and Design of Airport and Highway Pavements

ASTM D1556/D1556M – Standard Test Method For Density and Unit Weight of Soil in Place by Sand-Cone Method.

ASTM D1566 Standard Terminology Relating to Rubber.

ASTM D2216 -19 Standard Test Methods for Laboratory Determination of Water (Moisture) Content of Soil and Rock by Mass.

ASTM D6270 – Standard Practice for Use of Scrap Tires in Civil Engineering Applications

ASTM D6913/D6913M – Standard Test Method for Particle Size Distribution (Gradation) of Soil Using Sieve Analysis

ASTM D7205/D7205M – 21 Standard Test Method for Tension Properties of Fiber Reinforced Polymer Matrix Composite Bars

ASTM D7617/D7617M Standard Test Method for Transverse Shear Strength of Fiber-Reinforced Polymer Matrix Composite Bars

Boyd C. Ringo and Robert B. Anderson (1996) Designing floor slabs on grade - second edition. (1-2, 26-40).

Brinkgreve. R. B. J.; Engin. E; Engin. H.K. (2010) Validation of Empirical Formulas to Derive Model Parameters for Sands.

Bryan E. Barragan; Antonio Mudadu; Giuseppe Tiberti; Giovanni A. Plizzari (2023) GFRP Reinforced Concrete Slab Under Restrained Shrinkage.

CATRA Annual Report 2022

CSA S806-12 Design and Construction of Building Structures with Fiber-Reinforced Polymers.

CSA S807-19 Specifications for Fiber-Reinforced Polymers

El Naggar, A; El Naggar, H; Sadeghian, P (2019) Using TDA to Partially Replace Coarse Aggregates in Concrete Mixtures. DOI: <http://hdl.handle.net/10222/75927>

El Naggar, H.; Ashari, M.; Mahgoub, A. Development of an empirical hyperbolic material model for TDA utilizing large-scale triaxial testing. *Int. J. Geotech. Eng.* 2022, 16, 133–142. DOI: <http://dx.doi.org/10.1080/19386362.2021.1902118>

El Naggar, H.; Zahran, K. Effect of the Particle Size on T.D.A. Shear Strength Parameters in Triaxial Tests. *Buildings* 2021, 11, 76. DOI: <http://dx.doi.org/10.3390/buildings11020076>

El Naggar, H.; Zahran, K.; Moussa, A. Effect of the Particle Size on the T.D.A. Shear Strength and Stiffness Parameters in Large-Scale Direct Shear Tests. *Geotechnics* 2021, 1, 1–17. DOI: <https://doi.org/10.3390/geotechnics1010001>

(EWA) Environmental Waste International - <https://www.ewi.ca/tires-process.html>

Gridforce GF30-Geocell panel <https://www.gridforce.co.uk/product/gf30-black/>

Hegde, A. Geocell reinforced foundation beds-past findings, present trends and future prospects: A state-of-the-art review. *Construction and Building Materials* 154 (2017) 658–674 / DOI: <https://doi.org/10.1016/j.conbuildmat.2017.07.230>

Hegde, A.; Sitharam, T.G. Performance Of Shallow Footing On Geocell Reinforced Clay Bed Using Experimental And Numerical Studies. *Proceedings of Indian Geotechnical Conference December 13-15,2012, Delhi*

Horace Moo-Young; Kassahun Sellasie; Daniel Zeroka; Gajanan Sabnis (2023). Physical and Chemical Properties of Recycled Tire Shreds for Use in Construction. DOI: [http://dx.doi.org/10.1061/\(ASCE\)0733-9372\(2003\)129:10\(921\)](http://dx.doi.org/10.1061/(ASCE)0733-9372(2003)129:10(921))

Li, H.; Xu, Y.; Chen, P.; Ge, J.;Wu, F. Impact Energy Consumption of High-Volume Rubber Concrete with Silica Fume. *Adv. Civ.Eng.* **2019**, 2019, 1728762. DOI: <http://dx.doi.org/10.1155/2019/1728762>

Ling Zhang; Qiang Qu; Minghua Zhao, Double-Beam Model to Analyze the Performance of a Pavement Structure on Geocell-Reinforced Embankment. DOI: [https://doi.org/10.1061/\(ASCE\)EM.1943-7889.0001453](https://doi.org/10.1061/(ASCE)EM.1943-7889.0001453)

Mandal, J. N.; Gupta, P. Stability of geocell reinforced soil. DOI: [https://doi.org/10.1016/0950-0618\(94\)90009-4](https://doi.org/10.1016/0950-0618(94)90009-4)

Maryam Nazari; Fariborz M. Tehrani; Mojtaba Ansari (2022) Lightweight Rubberized Concrete Slabs for Sustainable Road Pavements Serving Non-Auto Traffic DOI: <https://doi.org/10.3311/PPci.19346>

Mohamed Hassan; Ehab Ahmed; Brahim Benmokrane (2013) Punching-Shear Strength of Normal and High-Strength Concrete Flat Slabs Reinforced with GFRP Bars. DOI: [http://dx.doi.org/10.1061/\(ASCE\)CC.1943-5614.0000424](http://dx.doi.org/10.1061/(ASCE)CC.1943-5614.0000424)

Molenaar, A. Durability, A Prerequisite for Sustainable Pavements. In Proceedings of the 5th Eurasphalt and Eurobitume Congress, Istanbul, Turkey, 13–15 June 2012.

Plaxis 3D Manual

Reda Taha, M. M.; El-Dieb, A. S.; M. A. Abd El-Wahab, M. A.; M. E. Abdel-Hameed, M. E. (2008) Mechanical, Fracture, and Microstructural Investigations of Rubber Concrete. DOI: [http://dx.doi.org/10.1061/\(ASCE\)0899-1561\(2008\)20:10\(640\)](http://dx.doi.org/10.1061/(ASCE)0899-1561(2008)20:10(640))

Suijt Kumar Dash, Influence of relative density of soil on performance DOI: [http://dx.doi.org/10.1061/\(ASCE\)MT.1943-5533.0000040](http://dx.doi.org/10.1061/(ASCE)MT.1943-5533.0000040)

Suijt Kumar Dash; Sireesh, S.; Sitharam, T.G. Model studies on circular footing supported on geocell-reinforced sand underlain by soft clay. Geotextiles and Geomembranes 21 (2003) 197–219. DOI: <http://dx.doi.org/10.1139/t04-117>

Sun Li-xiang; Lin Peng-zhen; Yang Zi-jiang; Liu Ying-long; Shen Qu (2021) Experimental study on flexural behavior of GFRP reinforced concrete slabs doi:10.1088/1755-1315/676/1/012060. DOI: <http://dx.doi.org/10.1088/1755-1315/676/1/012060>